Dissertation zur Erlangung des Doktorgrades
an der Fakultät für Chemie und Pharmazie
der Ludwig-Maximilians-Universität München

# Hierarchically structured zinc imidazolate mesophases

von

**Christian Sebastian Josef Junggeburth**

**aus**

**Würzburg**

**2013**

**ERKLÄRUNG**

Diese Dissertation wurde im Sinne von § 7 der Promotionsordnung vom 28. November 2011 von Frau Prof. Dr. Bettina Lotsch von der Fakultät für Chemie und Pharmazie betreut.

**EIDESSTATTLICHE VERSICHERUNG**

Diese Dissertation wurde selbständig und ohne unerlaubte Hilfe erarbeitet.
München, den 26.02.2013

.....

(Sebastian Junggeburth)

Dissertation eingereicht am 26.02.2013
1. Gutachter: Prof. Dr. Bettina Lotsch
2. Gutachter: Prof. Dr. Christina Scheu
**Mündliche Prüfung am 25.03.2013**

*Für meine Familie*

## Copyrights

Parts of this work have been and are subject to the following copyrights. They have been reproduced with permission of the corresponding publisher and have only been adapted with respect to the format of this thesis.

**Towards Mesostructured Zinc Imidazolate Frameworks**,

S. C. Junggeburth, K. Schwinghammer, K. S. Virdi, C. Scheu, B. V. Lotsch, *Chem. Eur. J* .**2012,** *18***,** 2143-2152, DOI: 10.1002/chem.201101530.
**Copyright © 2012 WILEY-VCH Verlag GmbH & Co. KGaA, Weinheim.**

**Ultrathin 2D Coordination Polymer Nanosheets by Surfactant-Mediated Synthesis,**

S. C. Junggeburth, L. Diehl, S. Werner, V. Duppel, W. Sigle, B. V. Lotsch, *J. Am. Chem. Soc.* **2013,** *135***,** 6157–6164, DOI: 10.1021/ja312567v.
**Copyright © 2013 American Chemical Society.**

## Danksagung bei….

…Prof. Bettina Lotsch, dass sie mich als ihren ersten Mitarbeiter in Ihren Arbeitskreis aufgenommen hat. Ebenso möchte ich Ihr für alle Unterstützungen und die zahlreichen Diskussionen danken, die die Arbeit verbessert haben.

…Prof. Christina Scheu für die Übernahme des Zweitgutachtens und für die Beantwortung und Diskussion zahlreicher TEM-Fragen.

…Prof. Wolfgang Schnick, Prof. Konstantin Karaghiosoff, Prof. Oliver Oeckler und Prof. Dirk Johrendt, für den Beisitz in meiner mündlichen Prüfung.

…Christian Minke für zahlreiche EDX/Festkörper-NMR Messungen.

…Christine Neumann, Peter Meyer und Prof K. Karaghiosoff für Flüssig-NMR-Messungen.

…Viola Duppel für ihren unermüdlichen Einsatz und Abarbeitung meiner zahlreichen SEM/TEM-Proben. Ich habe dich ja manchmal ganz schön mit SEM/TEM-Proben überschüttet.

…Hartmund Hartl/Marie Luise Schreiber für ICP-Messungen.

…Dr. Sophia Makowski für DTA-TG Messungen.

…Wolfgang Wünschheim für die Beseitigung von Hardware- und Software Problemen.

…Dr. Johannes Weber und Vico Celinski für die nette Atmosphäre im Büro D2.074, insbesondere Johannes für die Beantwortung und Diskussion zahlreicher Festkörper-NMR-Fragen. Ich wünsche Euch viel Spaß und Erfolg in Siegen.

…dem gesamten AK-Johrendt und AK-Schnick für die vielen Sing-Star Abende und für die nette Atmosphäre.

…dem gesamten AK-Lotsch bestehend aus der Stuttgarter-Fraktion: Viola Duppel, Claudia Kamella, Willi Hölle, Roland Eger, Friedrich Kögel, Prof. Jürgen Köhler, Vincent Lau, Cheng Li, Alexander Kuhn, Olalla Sánches-Sobrado, Vijay Vyas und Daniel Weber.

…der Münchener Zweigstelle des AK-Lotsch bestehend aus den aktuellen Mitarbeitern: Stephan Werner, Annekathrin Ranft, Linus Stegbauer, Erik Flügel, Ida Pavlichenko, Christian Ziegler, Stephan Hug und den Alumnis (die nach Stuttgart gegangen sind):

Tanja Holzmann, Katharina Schwinghammer, Brian Tuffy und Hongji Wang. Vielen Dank für die schöne Zeit und Zusammenarbeit.

…dem halben AK-Johrendt Labor in D2.049 Erwin Wiesenmayer, Christine Hiecke und Tobias Stürzer für die nette Zusammenarbeit.

…der Kochgruppe: Florian Pucher, Cora Hecht, Stephan Werner,Alexey Marchuk, Erik Flügel, Linus Stegbauer, Eva Wirnhier, Dominik Baumann für abwechslungsreiche Küche.

….Anna, Erik, Brian, Linus, Stephan und Kadda möchte ich noch fürs Korrekturlesen meiner Arbeit danken.

…meinen Praktikanten, allen voran Leo Diehl, Chiara Donadel, Danica Radmanovac, Katharina Schwinghammer, Agata Szymanek, Jihze Jin, Yaching Yu, Geraldine Rühl, Jörn Martens, Marcos Kettner und Aom Oruthai für die nette Zusammenarbeit, die mir viel Spaß gemacht hat.

…meiner Familie möchte ich besonders für die Unterstützung danken, ohne die dieses Studium nicht möglich gewesen wäre.

# I. Zusammenfassung

Die vorliegende Arbeit beschreibt die Synthese und Charakterisierung der ersten Vertreter der Substanzklasse meso-strukturierter Imidazolat Netzwerke (**MIF**, mesostructured imidazolate framework). Diese weisen sowohl Eigenschaften meso-strukturierter Verbindungen als auch metall-organischer Koordinationspolymere (hier Zink-Imidazolate) auf. Die dabei entstandenen lamellaren Systeme sind sowohl auf der atomaren als auf auch auf der Nanometer-Skala geordnet und sind damit die ersten Beispiele von hierarchisch geordneten Hybrid-Materialien an der Grenze zwischen Mesophasen und supramolekularen Koordinationsverbindungen.

Die Materialien sind im präparativen Maßstab unter inversen Mikroemulsionsbedingungen unter Verwendung eines kationischen Trialkylammonium-Tensids darstellbar. Die allgemein geringe Kristallinität und Strahlempfindlichkeit der **MIFs** erschwerte eine detaillierte Beschreibung der atomaren und der übergeordneten Nanostruktur. Eine Kombination aus Pulverdiffraktometrie, Festkörper-NMR-Spektroskopie (FK-NMR) und Elementaranalyse, Elektronenspektroskopie (EELS, EDX) und verschiedenen Mikroskopie-Methoden (TEM, AFM) wurde verwendet um die wesentlichen strukturellen Eigenschaften der **MIFs** herauszuarbeiten. Weitere Struktur-Informationen wurden durch klassisch-chemische Methoden erhalten. So wurde zum Beispiel durch Wahl eines längeren oder kürzeren Tensids die periodische Mesostruktur variiert.

Im ersten Teil der Arbeit (Kapitel 4) wurde die bekannte Analogie zwischen Zeolithen und zeolith-anlogen Imidazolat-Netzwerken (engl. *zeolitic imidazolate frameworks*, ZIF = Unterklasse von MOFs) erweitert, um die Existenz einer Zink-Imidazolat Mesophase zu zeigen, welche analog zur silica-ähnlichen Mesophase *MCM-50* ist. Ein Strukturbild basierend auf den eingangs erwähnten analytischen Methoden wurde entwickelt. Die *in-situ* Umwandlung des **MIFs** in einen mikroporösen ZIF verdeutlicht dabei die enge topologische Beziehung zwischen **MIFs** und ZIFs.

Im weiteren Teil der Arbeit (Kapitel 5) konnte durch Substitution von (2-Methyl-)Imidazol durch Benzimidazol in Gegenwart von Zinkacetat unter gleichen Bedingungen eine Struktur mit einer deutlichen größeren Periodizität auf der Nanometerskala erhalten werden. Auf atomarer Ebene zeigt sich das Vorliegen eines zweidimensionalen Poly[$\mu_2$-Acetato-$\mu_2$-Benzimidazolato Zink(II)] Koordinationspolymers (Schichtdicke ca. 1.1 nm), welches in Schichten aufeinandergestapelt ist. Circa alle fünf Schichten interkaliert das Tensid (Schichtdicke ca. 2 nm) und bildet so eine hierarchische Mesostruktur, mit einer Translationsperiode von ca. 8 nm. Hier zeigte sich, dass die nicht-kovalenten Bindungen zwischen Tensid und metall-organischem Koordinationspolymer stark sind und ein Entfernen des Tensids aus dem **MIF** mit organischen Lösemitteln, in denen das freie Tensid gute Löslichkeit zeigt, nur durch mehrstündiges Erhitzen der Verbindung möglich ist.

Im weiteren Teil der Arbeit (Kapitel 6) wurde das Acetat im Koordinationspolymer Poly[$\mu_2$-Acetato-$\mu_2$-Benzimidazolato Zink(II)] durch Carbonsäuren mit längeren Alkylketten

ersetzt. Hinweise auf ein Vorliegen einer hierarchischen Struktur analog zu Kapitel 5 konnten erhalten werden.

In Kapitel 7 und Kapitel 8 wurden weitere mesostrukturierte Phasen erhalten, in denen sich die zugrunde liegende Substruktur Poly[Acetato-Benzimidazolato Zink(II)] vermutlich zu anderen lamellaren Strukturen anordnet. Über den genauen Aufbau konnte nur gemutmaßt werden.

In Kapitel 9 wurden mehrere Benzimidazolderivate synthetisiert und verwendet, um verschiedene funktionelle Bausteine in das Poly[$\mu_2$-Acetato-$\mu_2$-Benzimidazolato Zink(II)] Koordinationspolymer einzubauen. Hiermit bietet sich die Perspektive einer kovalenten Postfunktionalisierung – analog zur Funktionalisierung von MOFs – von mesostrukturierten Imidazolat-Netzwerken zur Einbringung spezieller chemischer Eigenschaften.

# II. Abstract

This thesis describes the synthesis and characterisation of the first members of the class of mesostructured imidazolate frameworks (**MIFs**). This family of compounds combines structural features of both mesostructured materials and metal-organic coordination polymers (here zinc imidazolate frameworks). The obtained lamellar systems are ordered on the atomic as well as the nanoscale and hence are among the first examples of hierarchically ordered hybrid materials at the interface between mesophases and supramolecular coordination frameworks. The synthesis of these materials on a preparative scale can be done under inverse microemulsion by using a cationic surfactant of the trimethylammonium type.

The low crystallinity of mesostructured **MIFs** and their sensitivity to the electron beam hinders a detailed description of the atomic and supramolecular nanostructure. A combination of X-ray powder diffraction, solid-state NMR spectroscopy, elemental analysis, electron spectroscopy (EDX, EELS) and different microscopy techniques (TEM, AFM) were applied in order to work out essential structural aspects of the obtained **MIFs**. Further structural information was obtained by classical chemical methods. By the choice of shorter and longer surfactants, the periodic structure on the nanoscale was tuned.

In the first part of this thesis (chapter 4) the well-established analogy between the topologies of zeolites and zeolitic imidazolate frameworks (ZIFs, a MOF subclass) was extended to rationalize the observed existence of zinc imidazolate mesophases analogous to *MCM-50*-type silica mesophases. Furthermore, a structural model was developed based on the above named analytical techniques. The *in situ* transformation of the **MIFs** into ZIF nanoparticles demonstrates the close topological relationship between **MIFs** and ZIFs.

In chapter 5 a structure was obtained with a significantly longer periodicity on the nanoscale by substitution of (2-methyl)imidazole with benzimidazole in the presence of zinc acetate under otherwise similar conditions. On the atomic scale, the presence of a two dimensional poly[$\mu_2$-acetato-$\mu_2$-benzimidazolato zinc(II)] coordination polymer (layer thickness about 1.1 nm) was shown, where different layers are stacked consecutively. After approximately five layers the surfactant (layer thickness about 2 nm) is intercalated, creating a hierarchical structure with a translational period of about 8 nm. It was revealed that the non-covalent bonding between surfactant and metal-organic coordination polymer is strong and the extraction of the surfactant from the **MIF** material was only possible by boiling the compound in organic solvents for several hours, although the free surfactant shows a good solubility in these solvents.

In chapter 6 the acetate ion in the hybrid polymer poly[$\mu_2$-acetato-$\mu_2$-benzimidazolato zinc(II)] was replaced by carbon acids with extended alkyl chains. First indications were received about the existence of a hierarchical structure, analogous to the benzimidazolate mesostructures in chapter 5.

In chapter 7 and chapter 8 further mesostructured phases were obtained in which the poly[acetato-benzimidazolato zinc(II)]substructure presumably assembles into different lamellar mesostructures. The exact structures of these materials are still subject to speculation.

In chapter 9 several benzimidazole derivates were synthesized and used to install different functional groups on the poly[$\mu_2$-acetato-$\mu_2$-benzimidazolato zinc(II)] coordination polymer. Hereby the possibility of postfunctionalisation of mesostructured imidazolate frameworks by covalent bonding is opened up – analogous to MOF chemistry – which enables the generation of specific chemical functionality.

# III. List of abbreviations

All physical units agree with the International System of Units (SI).

| | |
|---|---|
| Å | Ångström, $10^{-10}$ m |
| AFM | Atomic force microscopy |
| ATR | Attenuated total reflection (IR spectroscopy) |
| Buto | Butyric acid |
| calc. | calculated |
| C | Carbon |
| °C | Temperature in degree Celsius |
| cm | Centimeters |
| $cm^{-1}$ | Wavenumbers |
| d | Days |
| DMF | Dimethylformamide |
| DTA-TG | Differential Thermal/Thermogravimetric Analysis |
| EDX | Energy-dispersive X-ray spectroscopy |
| *et al.* | *et alii*; And others |
| eV | Electron volts |
| exp | experimental |
| g | Grams |

| | |
|---|---|
| h | Hours |
| IR | Infrared |
| L | Liters |
| LMU | Ludwig Maximilians University |
| MS | Mass Spectrometry |
| MIF | Mesostructured Imidazolate Framework |
| min | Minutes |
| mL | Milliliters, $10^{-3}$ L |
| $\mu$L | Microliters, $10^{-6}$ L |
| mm | Millimeters, $10^{-3}$ m |
| $\mu$m | Micrometers, $10^{-6}$ m |
| mmol | Millimols |
| MOF | Metal Organic Framework |
| nm | Nanometers, $10^{-9}$ m |
| NMR | Nuclear magnetic resonance |
| OAc | Acetyl |
| Pro | Propionic acid |
| ppm | Parts per million |
| PXRD | Powder X-ray diffraction |

| | |
|---|---|
| rpm | Rounds per minutes |
| TEM | Transmission electron microscopy |
| SEM | Scanning electron microscopy |
| wt% | Weight percent |
| ZIF | Zeolitic Imidazolate Framework |

# IV. Table of Contents

# 1 Introduction

At the end of the 19th century the Swedish mineralogist Axel F. Cronstedt discovered, by heating the zeolitic mineral stilbite, that large amounts of water vapor are released from the mineral. He termed the mineral zeolite, “boiling stone” – assembled from the two Greek words ζέω (*zéō*), meaning "to boil" and λίθος (*líthos*), meaning "stone".[1] Very soon afterwards, key characteristics for this new material class such as reversible dehydration and ion exchange properties were discovered.[2-3] Around 1930 the two pioneers Tailor and Pauling revealed the regular arrays of channels and cavities (ca. 3 – 15 Å) by the first structure analysis of these crystalline materials, which contained a nanoscale labyrinth that can be filled with water or other guest molecules.[4-5] In zeolites, the [$SiO_4$]-tetrahedrons is replaced systematically by [$AlO_4$]-tetrahedrons. Zeolites have specific Lewis and Brønsted-acid cation-exchange centers suitable for multitudinous catalysis reactions relying on acid catalysis. Size and shape selectivity occur due to different combinations of the corner sharing tetrahedra. In the following years the number of known zeolite structures was extended by Richard Barrer and Robert Milton who presented new, synthetic zeolites obtained under hydrothermal conditions.[6-8] Today, there are 48 natural and more than 150 synthetic zeolitic minerals known.[9] In 1950 the synthesis of zeolite X, which is isostructural with the mineral faujasite, led to important industrial applications like the fluidized catalytic cracking (FCC) of petroleum, air separation and purification.[10-11] Nowadays zeolites are the most important heterogeneous acidic catalysts used in the chemical industry.[12-13] For example, the majority of the world’s gasoline is produced using zeolites as catalysts.[14] In 1982 scientists started to replace silicon and

aluminum by other elements creating many new zeotypes (zeolite-like materials), e.g. (silico-)-aluminophosphates.[15] Additionally, many phosphate structures with different transition metals are known,[16-17] as well as a large variety of open framework structures with metallosilicates, containing e.g. Fe, B, Ti, Ga, among others.[18] Moreover, lots of porous structures of nitrides, sulfides and halides were discovered recently.[19] Today zeolites are used and applied in a variety of research fields such as heat storage,[20] medicine,[21-23] detergents,[24] molecular sieves,[25] biological carriers,[26] photovoltaics,[27] chemical sensors,[28] and gas storage[29] (e.g. $NH_3$,[30] $CH_4$[31]), just to name a few.

In 1989 IUPAC classified porous materials according to their pore size. They were named microporous with pore sizes below 2 nm, as mesoporous with pore sizes 2 - 50 nm, or as macroporous with pore sizes > 50 nm (Figure 1.1).[32]

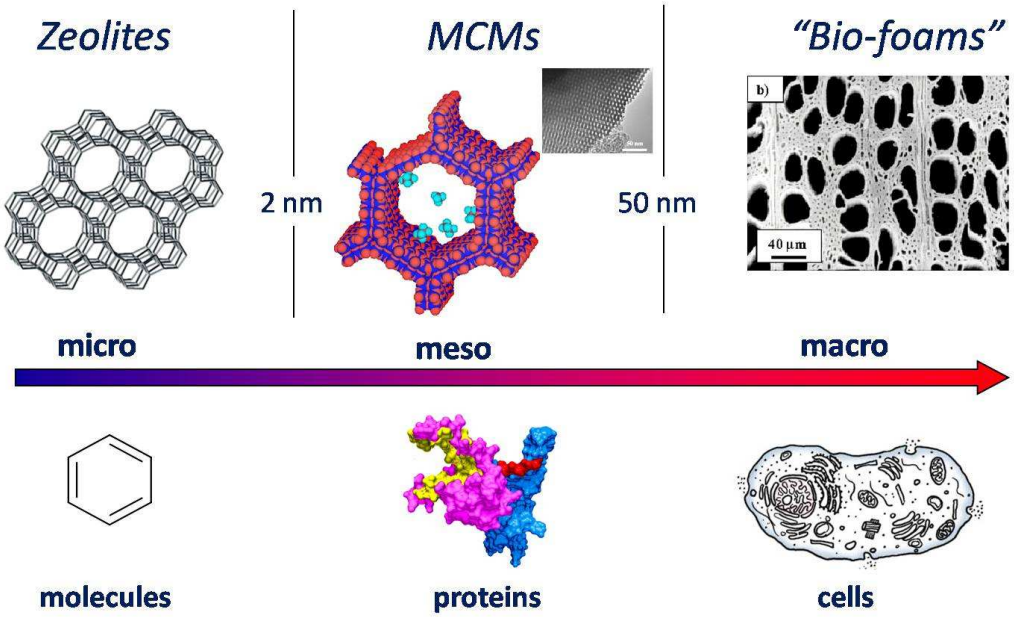


**Figure 1.1** Classification of porous materials in different size regimes.[33]

In 1992 Kresge *et al.* from the Mobil Oil company presented a further milestone of silica-based porous materials, the MCM-family (MCM = Mobile Composition of

Matter).[34-35] Typical for these materials are the amorphous silica walls, which can form uniform mesopores (3 – 5 nm), regular pore arrangements and have high specific surface areas (1000 $m^2 \cdot g^{-1}$). While in zeolites the template typically is a single molecule or ion, the new approach is based on self-assembled molecular arrays of amphiphilic surfactants (surface active agents), which are used as structure directing agents.

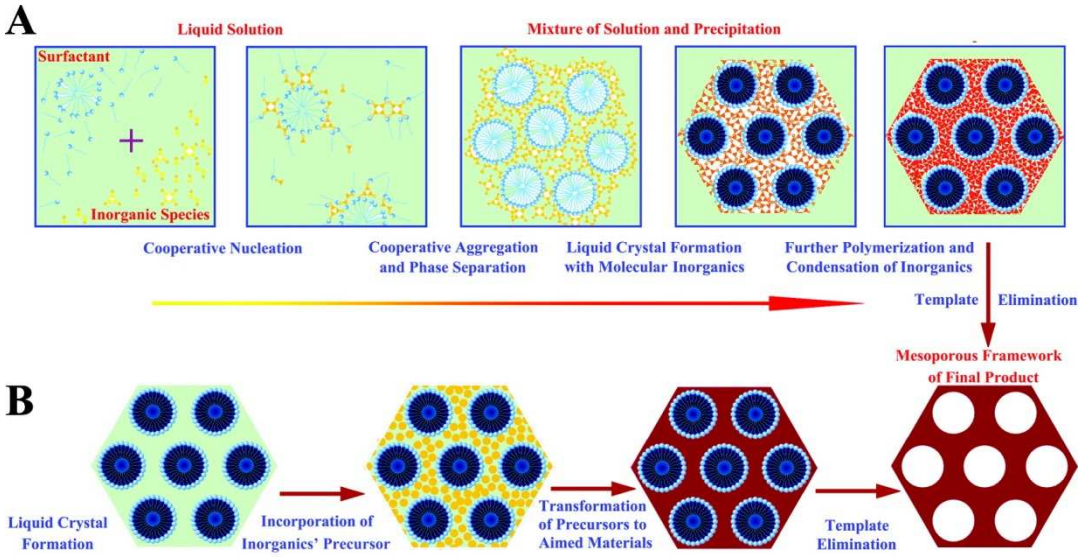


**Figure 1.2** Possible formation mechanisms of mesoporous systems. A) Self-Assembly and B) True liquid crystal templating. Reprinted with permission from ref. 36 Copyright © 2007 American Chemical Society.

In general, two mechanisms for the formation of mesoporous materials are discussed (Figure 1.2): Firstly, *cooperative self-assembly*: For example, positively charged surfactants $S^+$ such as CTAB (cetyltrimethylammonium bromide) generate micelles by forming supramolecular assemblies under hydrothermal conditions.[36] Around these positively charged head groups $S^+$ the anionic inorganic species $I^-$ assemble, driven by Coulomb forces. The inorganic silica species originate from the hydrolysis of monomeric precursors such as TEOS (tetraethyl-orthosilicate) in a sol-gel reaction, which condense in both basic and acidic media into inorganic oligo- and polymers

(here: oligomeric and polymeric silicates). On the boundary surface $S^+I^-$ the charge density changes drastically, which leads to formation and assembly of micelles.

The final mesostructure results from the polymerization and cross-linking of the oligomers (Figure 1.2A). The driving force is the minimization of interfacial energy. Reaction conditions (e.g. pH-value, molar ratios ($S^+ : I^-$), temperature, concentrations, amount and type of solvents) influence pore size, the structural order, stability and topology of the mesostructure. Based on the geometrical arrangement of the pores, the materials are classified as cubic,[34, 37-41] hexagonal,[35] or lamellar structures (Figure 1.3).[42]

The second formation mechanism is called *true liquid crystal templating* (TLCT). For TLCT, the lyotropic liquid crystalline phase is already present in the reaction mixture, before the addition of the inorganic species and before the polymerization process begins. The surfactant template can be removed by different procedures, e.g. calcination at high temperatures, plasma,[43] microwave irradiation,[44] exchange of the trimethylammonium surfactant with ammonium nitrate solution in ethanol,[45] or under supercritical $CO_2$ to convert the mesostructured compound in a mesoporous material.[46]

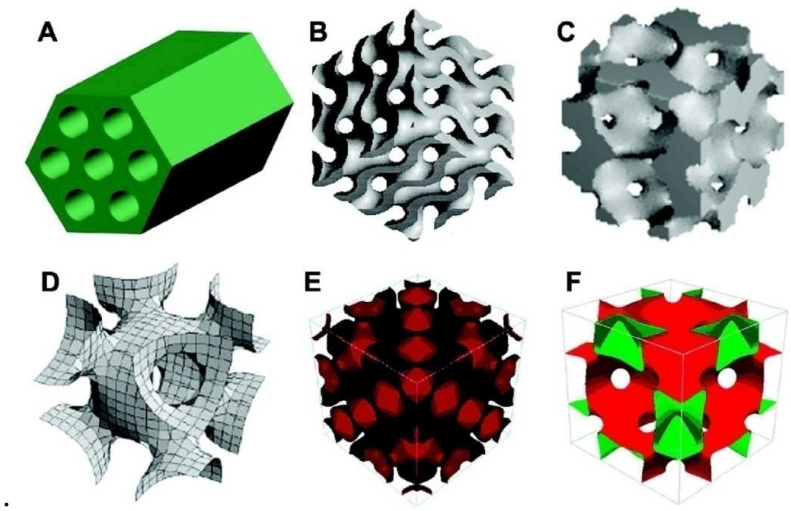


**Figure 1.3** Pore models of mesostructures with symmetries (A) P6mm, (B) Ia-3d, (C) Pm-3n, (D) Im-3m, (E) Fd-3m, and (F) Fm-3m.[38-41]Reprinted with permission from ref. 36 Copyright © 2007 American Chemical Society.

Mesoporous materials are also accessible by using neutral surfactants. In 1995, Taneva *et al.* succeeded to generate mesoporous silica, named HMS (Hexagonal Mesoporous Silica), by using primary amines as template.[47] Also, MSU-materials[48] (Michigan State University) were presented by using neutral poly(ethylene oxides) as templates, and SBA materials[49] (Santa Barbara) by using pluronics-type surfactants as a template, respectively. Pluronics are nonionic triblockcopolymers, composed of a central hydrophobic chain of poly(propylene oxide), sandwiched between two hydrophilic chains of poly(ethylene oxide). The obtained SBA-materials exhibit remarkable mesopore sizes and a larger morphological variety[50] than MCM-materials and in addition, they feature micropores due to poly(ethylene oxide) templating effects.[49, 51] Due to thicker pore walls an increasing thermal and chemical stability was observed.[52] The obtained mesostructured materials can be converted very easily into mesoporous systems by washing with ethanol.

The modification of the inorganic precursors reveal a variety of new mesoporous materials e.g. mesoporous metal oxides using Nb, Ta, Ti, Zr, Ce, Sn and many non-oxide systems like metals[53], sulfides[54], nitrides[55], selenides[56] and phosphates,[57] to name a few. Ordered mesoporous carbon materials, named $CMK_n$ (Carbon Meso-structured by KAIST = Korea Advanced Institute of Science and Technology), employ in a first step a mesoporous MCM-type material as a hard template, where the pores are filled with an organic compound (e.g. sugar). Finally, the MCM material is destroyed by pyrolysis, thus releasing the replica of the initial MCM template.[58]

Tremendous efforts were made to synthesize mesoporous materials with crystalline microporous walls. The Ryoo group could establish a series of different hierarchically structured compounds by using gemini surfactants (polyquarternary ammonium type). The microporosity arises from the charge compensation of the ammonium molecules with the negative charge of the zeolite framework, while the mesopores are generated from the supramolecular templating effect of the long alkyl chains of the gemini surfactants.[59-60]

As mentioned before, zeolites are built-up of $SiO_4/AlO_4$ tetrahedrons (each tetrahedron = primary building unit), which are linked *via* corner-sharing oxygen atoms to form secondary building units (SBUs). These SBUs consist of rings with different sizes and can be linked to form a variety of cages and channels. By formally replacing the oxygen as a linker with polytopic organic linkers, a new material class is established, the so-called metal-organic frameworks (MOFs). The term MOFs, which is sometimes substituted by “Hybrid Organic Inorganic Frameworks”, or “coordination polymers”, was coined in 1995 by *Yaghi* and co-workers,[61] although it should be mentioned that the first synthesis of a crystalline coordination polymer was reported

as early as 1965.[62] Today, the term MOF represents all crystalline porous materials consisting of metal centers joined by organic linkers, resulting in a three dimensional periodic network. Conceptually, there is no fundamental difference between zeolites and MOFs, therefore MOFs with zeolite-like structures can in principle be considered as zeotypes with widened and modified pore systems through the assembly of organic linkers with different types of metal ions. By replacing the tetravalent metal centers in zeolites with two-, three-, four- or sixfold coordinated metal centers in MOFs, each connectable to different polytopic linkers (mono-, di-, tri- or tetravalent ligands), the number of combination possibilities for generating networks increases drastically in comparison to zeolites (Figure 1.4). This concept is summarized under the term "*Reticular chemistry*". *Reticular chemistry* is one of the most important concepts towards network design and to new materials with unparalleled diversity.[63-65] This term, which was developed at the beginning of the 1990s, signifies the linking of molecular building blocks through strong bonds into predetermined structures.[66] MOFs consist of metal clusters which are joined over polytopic linkers to form finite SBUs. Different SBUs are assembled into specific network geometries and, hence, topologies through a periodic net. A crucial aspect here is that the number of default nets is limited due to the given default geometry of the molecular building units.[67] The different topologies (also called nets) of MOFs result from the varied arrangement of SBUs.[64, 68]

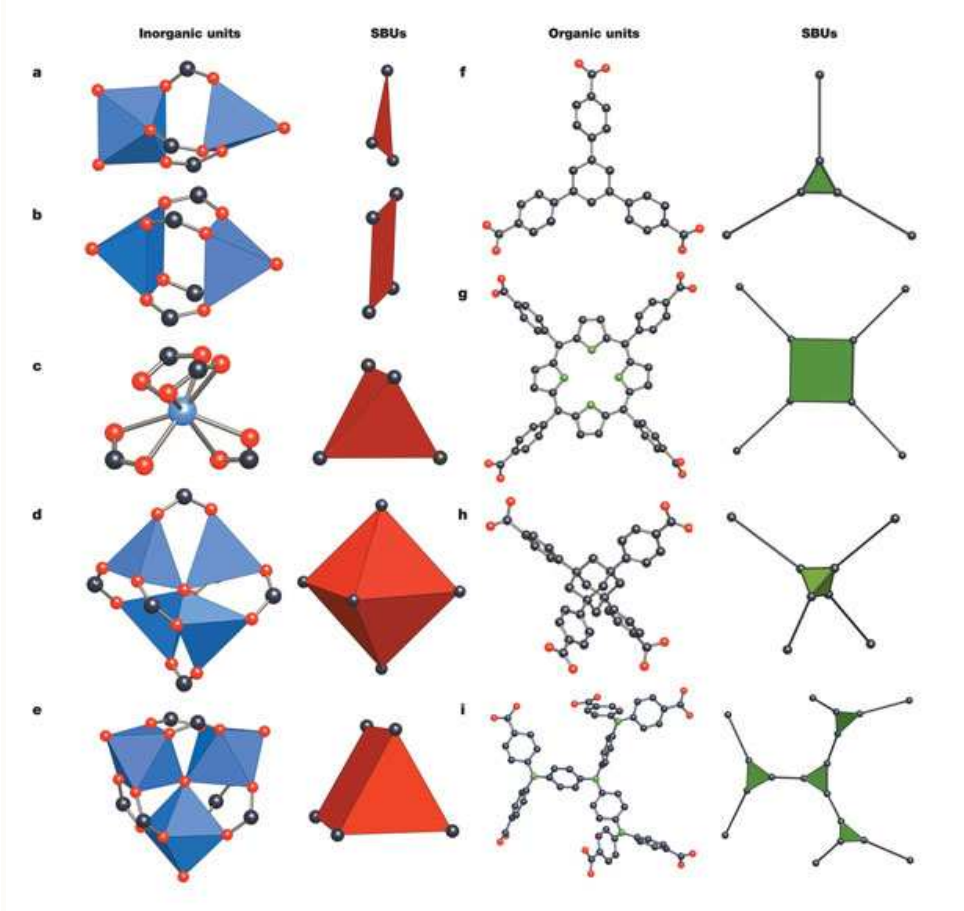


**Figure 1.4** Examples of secondary building blocks (SBU) from carboxylate-based MOFs. O, red; N, green; C, black. In inorganic units metal-oxygen polyhedra are blue, and the polygon or polyhedron defined by carboxylate carbon atoms (SBUs) are red. In organic SBUs the polygons or polyhedrons to which linkers (all $–C_6H_4–$ units in these examples) are attached are shown in green. Reprinted with permission from ref. 63 Copyright © 2003 by Nature Publishing Group.

Nets of equal topology are termed IRMOFs (= Isoreticular Metal-Organic Frameworks). Using the example of cubic MOF-5, prepared by a reaction of $Zn(NO_3)_2$ and terephtalic acid, Yaghi *et el.* firstly demonstrated the versatility of pore size and network functionality tuning of MOFs, by using 16 different organic linkers which gave rise to 16 isoreticular nets (Figure 1.5).[69] Interpenetrating three-dimensional networks result from the usage of large ligands (Figure 1.5, structures 9, 11, 13, 15). Their ability of storing gases is higher than the corresponding non-catenated struc-

tures due to the reduced pore diameter.[70-71] The challenges of interpenetration were overcome by using alkyl modified ligands as presented for MOF-74 $M_2$(2,5-DOT) (M = $Zn^{2+}$, $Mg^{2+}$, DOT = dioxidoterephthalate), creating a series of IR-74 MOFs with pore sizes up to 85 Å.[72] Recently *Choi et al.* showed for MOF-123 ($[Zn_7O_2(NBD)_5$-$(DMF)_2]$ (NBD= 2-nitrobenzene-1,4-dicarboxylate, DMF = *N*,*N*-dimethylformamide) the reversible interpenetration triggered by addition or removal of the solvent (DMF).[73]

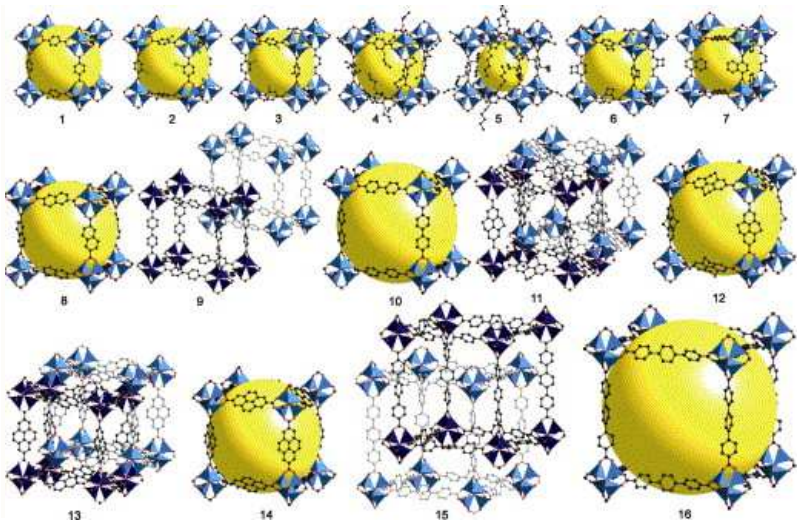


**Figure 1.5** Illustration of the isoreticular MOF principle based on different cubic network topologies. The varied organic linkers differ in functionality and length. Reprinted with permission from ref. 74. Copyright © 2004 Elsevier.

A common disadvantage of MOFs in comparison to zeolites is their relative thermal instability and sensitivity towards air/moisture. Especially MOFs containing zinc metal centers are less stable than other metal analogues.[75]

As organic polytopic linkers carboxylates, phosphonates, sulfonates, pyridine, imidazole, triazole, tetrazole derivates and many others are usually applied.[76-79] In order to generate rigid, porous networks, aromatic systems are used as organic backbones.

Recently, new networks were published focusing on chiral ligands[80] like sugar (γ-cyclodextrin),[81] crown ethers,[82] amino acids[83] and polypeptides.[83-84]

Generally MOFs and zeolites are synthesized by solvothermal methods in water, dimethylformamide, ethanol, methanol, acetonitrile and many others, with temperatures varying from room temperature up to almost 300 °C.[85] Also solvent-free solid-state methods lead to a range of crystalline MOFs.[86] New approaches also use ionic liquids as a solvent medium to produce new network topologies.[87]

Possible applications of MOFs are envisioned in gas purification,[88] gas storage,[89] catalysis,[90-92] or for biomedical applications[93], nonlinear optics[94] and as sensor devices.[95]

*Férey* and co-workers presented the MOF family of MILs (Materiaux de Institute Lavoisier), the first crystalline mesoporous MOF materials, synthesized in a hydrothermal reaction of $Al(NO_3)_3$ with terephthalic acid (MIL-53).[96-97] Usually, MILs are more chemically (in water and air) and thermally (up to 500 °C) stable in comparison to *Yaghi's* MOFs (such as MOF-5). To overcome the problem of hydrolysis, metal - ligand bonds which are less prone to hydrolysis where employed. This leads to a subgroup of MOFs, termed zeolitic imidazolate frameworks (ZIFs),[98] featuring more than 100 different topologies.[99] ZIFs are composed of tetravalent transition metal $M^{2+}$ ions ($M^{2+}$ = Fe, Co, Cu, Zn) bridged by organic imidazolate linkers. Since the metal-imidazole-metal (M-IM-M) angle in ZIFs is about ~145°, which is similar to the Si-O-Si angle in zeolites (Scheme 1.1), ZIFs tend to take on zeolite-like topologies[100-101] (Figure 1.6), but also structures which have not been known from zeolites.[102] The microporous ZIFs have remarkable thermal stability (up to 550 °C)

and can be boiled in water or organic solvents for a long time without decomposition, which was typically pointed out for ZIF-8 ($Zn(MeIM)_2$) (MeIM = 2-methylimidazole) and ZIF-11 ($Zn(BeIM)_2$) (BeIM = benzimidazole). Furthermore, ZIFs exhibit unusual selectivity for $CO_2$ capture and extraordinary capacity for storing $CO_2$, e.g. one liter of ZIF-69 can hold ~83 liters of $CO_2$at 273 K under ambient pressure.[101] These characteristics make ZIFs an attractive target for developing gas selective membranes[103-104] and for sensor devices[105] like in photonic crystals.[106] Some lines of research also focus on drug delivery approaches. ZIF-8 ($Zn(MeIM)_2$) can highly efficiently encapsulate caffeine within a one-step reaction.[107]

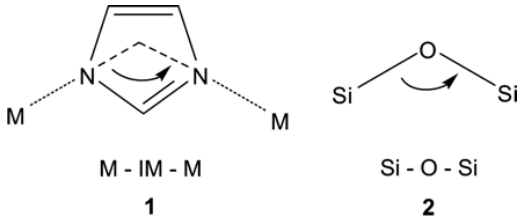


**Scheme 1.1** M-X-M (X=O, IM) bridging angles are about 145° in metal IMs (1) and zeolites (2), thus leading to zeolite-like topologies in ZIFs.

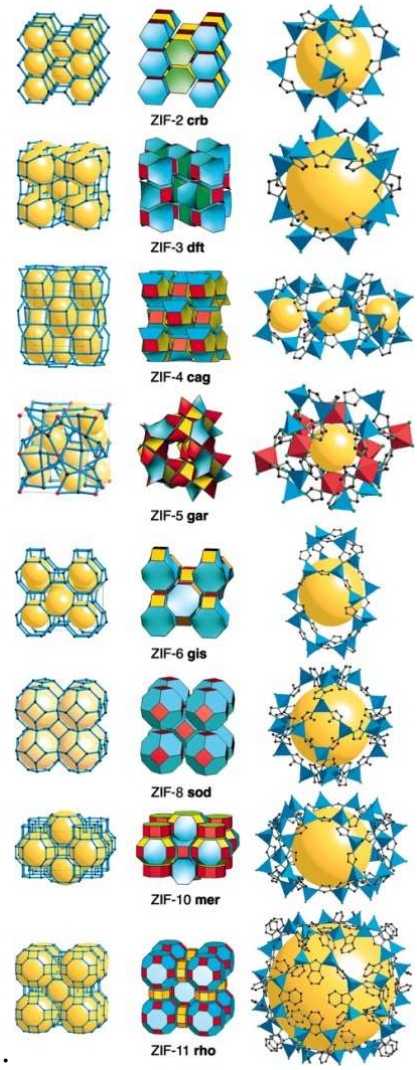


**Figure 1.6** Zeolite-like examples of crystal structures of certain ZIFs. Reprinted with permission from ref. 100 Copyright © 2006 National Academy of Sciences.

The presence of organic ligands as integral parts of MOF structures makes these solid-state materials more attractive targets for manipulation by organic reactions than other inorganic materials (e.g. zeolites). By targeting the organic linking component of the MOF, one can exploit the vast array of organic reactions available to transform the original MOF into a new MOF with altered functional groups and thus different physical and chemical properties. In 1999 *Lee and Kim* first demonstrated postsynthetic functionalization modifications (PSM) on a homochiral MOF.[108] They could show enantioselective catalytic transesterfication by inclusion of metal complexes in

the pores. *Cohen et al.* developed the concept of PSM on IRMOF-3 (space group *Fm*-3*m)*[69], synthesized from $Zn(NO_3)_2 \cdot 4H_2O$ and 2-amino-1,4-benzene dicarboxylic acid ($R_3$-BDC), by presenting numerous PSMs.[109-113] In IRMOF-3 the free amino group of the $R_3$-BDC ligand does not coordinate to the Lewis acid $Zn^{2+}$. In the first example of PSM the MOF was treated with acetic anhydride and yielded an acetamide-MOF in a single-crystal-to-single-crystal fashion.[109] Also a covalently bounded chelating ligand can be attached to the organic linkers, which is suitable for the complexation of Pd(II).[114] Likewise, the condensation of IRMOF-3 with isocyanates generates MOFs with urea functionality.[115] Under the appropriate conditions, also tandem reactions (multi step reaction) for PSM are possible.[116] The precursor ligand is varied in different steps and after this the network is destroyed by digestion. In this role the MOF-network has the functionality of a protection group. Also diastereoselective reactions on the organic linker can be achieved by PSM in a MOF.[117]

PSM can also be transferred to a series of different MOFs, e.g. Al-based (MIL-53(Al)-$NH_2$-MOFs)[118] and Zr-based[119] MOFs. Modified (Fe)-MIL-101 is an interesting candidate for biomedical applications.[120] The coupling process between the preinstalled precursor ligand on the MOF-lattice and the reactive species requires high chemical stabilities of the network with respect to the chemical conditions. However, all these modifications on the organic linkers are typically mild reactions and ZIFs have good thermal and chemical stabilities.[100-101] Modified ZIF-8 with sodalite topology bearing an additional carboxylaldehyde functionality on the imidazolate linker can be reduced even with the strong reducing agent $NaBH_4$.[121] In general, however, MOFs are very sensitive and collapse under the presence of strong ac-

ids/bases. Cr-MIL-101, on the contrary, “survives” even the PSM through nitration with $HNO_3/H_2SO_4$.[122]

Light can also be used for a postsynthetic modification of the network, e.g. to remove protecting groups from the organic components of the MOF-lattice.[123] When Cr-MIL-101-$NH_2$ (prepared by $CrCl_3$ and the $R_3$-BDC-ligand in a solvothermal reaction) was treated with *p*-phenylazobenzoylchloride/4-(phenylazo)-phenylisocyanate such that the azo groups point into the free mesoporous cages, it was possible to observe a *cis/trans* isomerization by irradiation with UV light.[124]

Oftentimes, multi-PSM steps cause a partial or a complete collapse of the framework, because the framework does not sustain the chemical conditions. The so-called “click reaction” is another promising route for the access to modified MOFs. In this reaction developed by *Sharpless et. al.*[125] an alkine and an azide perform an azide-alkyne [3+2] *Huisgen*-cycloaddition under copper(I) catalysis. High yields even at micromolar concentrations, mild reaction conditions (even in water), readily available starting materials and reactants are characteristic for this reaction and led to a broad application range, e.g. in polymer science[126-128] and in bioconjugation (*in vitro*[129-130] and *in vivo*[131-132]). Two routes are typically pursued in MOF chemistry: Firstly, the direct modification of an azide containing MOF,[133-134] and secondly, the other way round by a silyl-protected acetylene bearing framework, which is deprotected by aqueous KF, and functionalized in a controlled way by the click reaction.[135-136] Therefore, this reaction allows the accurate control over the loading, density and functionality of the inner pores of a MOF, by installing different functionalities close to each other, and through this influence the physical and chemical properties of a PSM-MOF.[137-138]

Around 2006 different groups (especially those of *W. B. Lin and G. Férey*)[139] started to draw attention on developing nano-sized MOFs (NMOFs) as drug delivery vehicles[140-142] and for medical imaging.[143-144] Two routes were taken for delivery of the active agent: First by incorporating active agents into the framework backbone or second, by loading active agents into the pores and channels of the NMOFs.[145] The stability and bio-availability of MOF nanoparticles can be improved by coating with organic polymers or silica based materials.

Controlling the size of the nanoparticles is one of the main challenges in MOF chemistry, as the rapid growth of most MOFs at room temperature invariably leads to macroscopically sized particles.[85, 146-147] Different synthetic strategies (solvothermal, nanoprecipitation, reverse microemulsion, surfactant templating under solvothermal conditions etc.) were employed to obtain NMOFs.[148] Surfactant-mediated reactions should not only control the particle size by impeding growth or through micelles acting as "nano-reactors", but also the stability of these particles against agglomeration. Important contributions in understanding the growth mechanism of NMOFs were developed in the past years.[149-151]

Recently, an increased interest in the development of mesoporous MOFs (called meso-MOFs) started to emerge. The first kind of meso-MOF was synthesized 2011 under the conditions of supercritical $CO_2$ in ionic liquids (1,1,3,3-tetramethylguanidinium acetate (TMGA)). As supramolecular template N-ethyl perfluorooctylsulfonamide (N-EtFOSA) was applied.[152] Other approaches to meso-MOFs, where the walls of the mesopores are constructed by a microporous framework, could only be achieved by chelating agents such as citric acid (CA). The CA creates Coulomb attractions and acts as a kind of mediator between the surfactant

molecule and the metal ions (Scheme 1.2).[153] Without citric acid no meso HKUST - 1 ($Cu_3(BTC)_2$) (BTC= benzene 1,3,5-tricarboxylic acid) could be produced. The analysis of this phase is based on sorption measurements. Small angle XRD measurements, evidencing the mesostructure, are not contained in this paper.

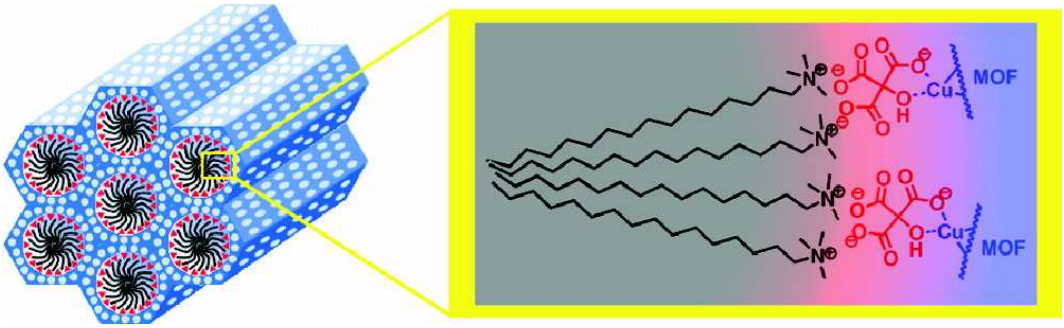


**Scheme 1.2** Cooperative template directed synthesis of meso-MOFs via self-assembly of metal ions and organic ligands. Reprinted with permission from ref. 153 Copyright © 2011 American Chemical Society.

These kinds of meso-MOFs often collapse after removal of the surfactant. COK-15 (COK = Centrum voor Oppervlaktechemie en Katalyse) is a HKUST-1-based MOF, but the structure is stabilized by a Keggin polyoxometalate.[154] This MOF exhibits uniform 5 nm large mesopores with crystalline micropore walls of the same thickness. A supramolecular template such as neutrally charged Pluronic molecules, can be used for the synthesis of meso-MILs.[155-156]

Owing to the similar geometry relationship between zeolites (silica based) and ZIFs (metal-organic based), both material classes reveal a topological relationship toward each other. MCM phases are built by the combination of surfactants with inorganic silica. This thesis addresses the question whether it is possible to extend the existing analogy between zeolites and ZIFs on the one hand to an anticipated analogy between mesoporous silica materials and mesoporous zinc imidazolates (dubbed **MIFs**) on the other hand (Scheme 1.3).

| | **Microporous (sub-nanoscale)** | **Mesoporous (nanoscale)** |
|---|---|---|
| **Silica-based** | Zeolites | MCM |
| **Metal + Linker** | MOFs / ZIFs | **?** |

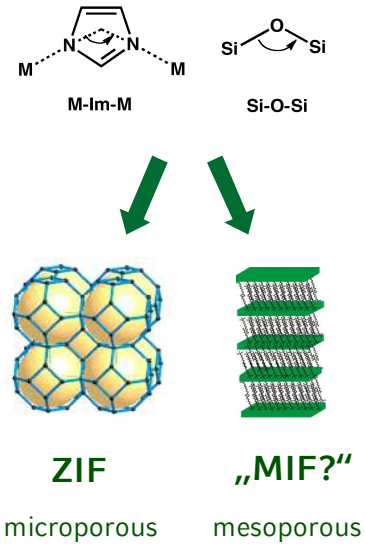


**Scheme 1.3** Schematic overview of the relationships between ZIFs, zeolites and the mesoporous/ meso-structured materials of the MCM type and **MIFs** (Mesostructured Imidazole Frameworks).

# 2 Characterization Methods

## 2.1 X-ray diffraction (XRD)

In order to identify materials and determine their phase purity, crystallinity, particle size symmetry and structure, powder X-ray diffraction is an excellent characterization method. According to Bragg's law, X-rays are scattered by sets of crystal lattice planes, the spacing of which being on the same order of magnitude as the wavelength of the radiation used:

$$n\lambda = 2d\ sin\theta$$

where $n$ is the diffraction order, λ is the used X-ray wavelength (in this work $CuK_{\alpha 1}$ radiation with λ = 1.540562 Å), $d$ the distance of the lattice planes and $\theta$ is the so-called Bragg angle at which constructive interference occurs. Constructive interference can only be observed for a periodic, i.e. crystalline lattice, giving rise to diffraction patterns which are characteristic of the particular material under study (Figure 2.1).

X-ray diffraction experiments were carried out on a D8 Discover Avance diffractometer (Bruker) in reflexion geometry and on two STOE diffractometers (Stadi P and Stadi P Combi, both in transmission geometry, Figure 2.2). All X-ray devices used employ Cu-$K_{\alpha 1}$ radiation (λ = 1.540562 Å). All samples were grinded before measuring.

The D8 diffractometer with a Bragg Brentano geometry is suitable to measure samples with large lattice parameters like mesostructured compounds up to *d*-values of

maximum 17.5 nm for 0.5 °= *2θ*. The powdered samples were compacted on glass slides, resulting in a flat surface for the measurements.

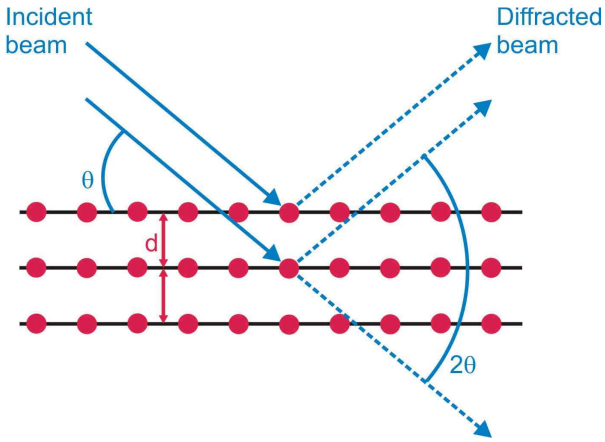


**Figure 2.1** Schematic of X-rays impinging on a periodic lattice at an angle fulfilling the Bragg condition.[157]

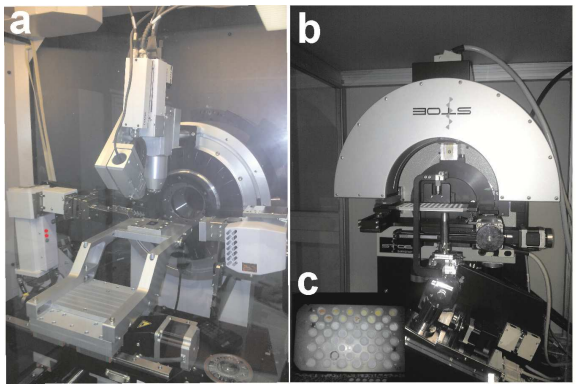


**Figure 2.2** a) D8 Discover Avance diffractometer and b) Stoe Stadi P Combi diffractometer c) with sample holder.

In the Stoe Stadi P Combi diffractometer equipped with a high-throughput device and an imaging plate detector, the samples were placed in a sample holder consisting of two pot plates, with a cellulose foil between them (Figure 2.2c). The instrument is suited for high-throughput-screening and short measurement times, such that this instrument was used primarily for phase identification. However, due to the static arrangement during the measurement, the powder patterns show preferred orientation. To minimize preferred orientation effects, samples were measured in a capillary

(diameter 0.2 – 0.5 mm, Hilgenfeld) under rotation in Debye-Scherer geometry on the Stoe Stadi P by a position sensitive detector. The evaluation of the recorded XRD patterns was done with the software package WINX$^{POW}$ by the Stoe Company.[162] Already known phases were identified by comparing measured data with those in the Joint Committee on Powder Diffraction Standards (JCPDS) database,[163] or by comparison with the literature. Indexing and Pawley fits of the XRD powder patterns were carried out with the Software TOPAS Academic Version 4.1.

## 2.2 Transmission electron microscopy (TEM)[158-161]

Transmission electron microscopy furnishes structural and compositional information of a material, including nanostructured samples. Electrons interact with matter much more strongly than X-ray radiation as they interact with both the nucleus and the electrons of the scattering atoms through Coulomb forces. The electron beam is generated either by a thermal emission source which may be a tungsten filament/$LaB_6$crystal, or by a Schottky field emitter. A complex magnetic lens system focuses the electron beam on the sample and the detector (CCD camera or fluorescent screen).

In scanning transmission electron microscopy (STEM) the focused electron beam spot rasters across the sample and the transmitted electrons are detected as a function of the scattering angle. In bright field mode (BF) imaging is formed directly by occlusion and absorption of electrons in the specimen. In annular dark field (ADF) the correlation of the electron count close to the direct beam is measured and high annular dark field mode (HAADF) uses electrons scattered into high angles. This is a highly sensitive method due to variations in the atomic number of atoms in the sam-

ple and gives information about the elemental composition and the thickness of the sample

When highly energetic electrons interact with a thin specimen by irradiation, several types of signals are emanated from a sample (Figure 2.3). A core state electron is removed by the electron beam and leaves behind a hole. This unstable state of the core hole can be filled by a higher shell electron, whereby the energy difference between both orbital energies is either released by emission of a characteristic X-ray radiation or by an Auger electron from the outer shell.

Elastic scattered transmitted electrons do not interact well with the specimen and do not suffer a direction change or an energy loss. The fraction of transmitted electrons is dependent on different factors such as the thickness of a sample, the chemical composition, and its periodic structure. Diffracted electrons and backscattered electrons are elastically scattered electrons with high energy and different angle of diffraction. Secondary electrons are emitted by inelastic interactions when high-energy primary electrons strike valence electrons of atoms in the specimen such that they are emitted from the sample. Their energy is rather low and they can only leave the specimen when they originate from within a volume close to the surface.

TEM Measurements were done by V. Duppel, Dr. W. Sigle (both MPI stuttgart) and K. S. Virdi (LMU-Munich). Cross-section experiments were done by B. Bußmann (MPI-Stuttgart). TEM experiments were performed on a Philips CM 30 ST equipped with a $LaB_6$ thermal source operated at 300 kV and on a JEOL 2011 instrument with a tungsten cathode operating at 200 kV, respectively. SAED simulations were carried out with the software EMAP. EDX linescans, EELS (Electron energy loss spectroscopy) measurements and Scanning Transmission Electron Microscopy in High Angle

Annular Dark Field mode (STEM-HAADF) were performed with a VG HB 501UX microscope. For cross-section experiments the sample was embedded in EpoFix resin, trimmed (Leica EM Trim 2) and cut with an ultramicrotome (Leica EM UC6). The resulting sample thickness was ~ 50 nm. The images were analyzed with the software Digital Micrograph version 3.6.1 (Gatan company).

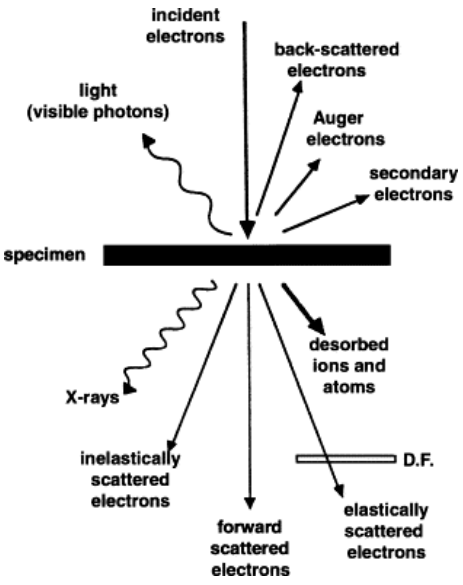


**Figure 2.3** Elastically and inelastically scattered electrons in electron microscopy. Reprinted with permission from ref. 158. Copyright © 2004 Elsevier.

## 2.3 Scanning electron microscopy (SEM) and Energy-dispersive X-ray spectroscopy (EDX)

Scanning electron microscopy (SEM) was used to investigate the morphology of the samples and to determine their composition by EDX spectroscopy. A focused beam of electrons, which is generated by an electron gun (with much smaller accelerating voltages of 0.1 - 30 eV compared to TEM), rasters over the sample surface in a rectangular scan pattern. The electrons interact with electrons in the sample and produce various signals which are detected. The produced secondary electrons ($E_{kin}$ < 50 eV)

are used for imaging the surface of a specimen. In EDX spectroscopy X-ray radiation is detected resulting from electron transitions between inner shells of atoms. All SEM/EDX measurements were done by Christian Minke (LMU Munich) and Viola Duppel (MPI-Stuttgart). The samples were located on a sample holder, sputtered with graphite and examined with a JSM-6500F microscope (Jeol, maximum voltage: 40 kV) or a Zeiss Merlin instrument. Qualitative and semi quantitative measurements were carried out with an integrated EDX spectrometer (Model 7418, Oxford Instruments).

## 2.4 Solid-State NMR spectroscopy[162-163]

Using solid-state NMR the investigation of local environments of NMR active cores is possible. Nuclear spins interact with a magnetic field. Spatial vicinity and/or a chemical bond between two atoms influence the interactions between different nuclei. In general, these interactions are orientation dependent. In crystals and powders these molecules are not rotating and therefore these anisotropic interactions have a substantial influence on the behavior of a system of nuclear spins. Through this the number of different chemical environments for an atom that exist can be differentiated.

By application of magic angle spinning (MAS) at an angle of 54.74° the anisotropy of interactions in a solid can be averaged out to a large extent, breaking down the powder pattern of the static sample into the isotropic resonances and a spinning sideband pattern, which is reminiscent of the powder pattern. The intensity of NMR signals of nuclei with low natural abundance and magnetogyric ratio can be increased by cross-polarization experiments (CP). Here, the magnetization of an abundant nuc-

leus (e.g. $^{1}H$) is transferred on the rare spin (e.g. $^{13}C$) to enhance the sensitivity of the latter.

The samples were grinded to a fine powder and transferred in $ZrO_2$ rotors (Ø = 4 or 2.5 mm). The spectra were recorded on a DSX Avance 400 spectrometer (Bruker) at room temperature. Depending on the examined nucleus and sample, the contact time, rotation frequency, number of scans and recycle delay differ. All parameters for the different measurements are summarized in Tables S1, S2 and S3.

## 2.5 Solution NMR spectroscopy

In contrast to solid state NMR, in solution NMR Brownian motion leads to an averaging of anisotropic interactions. These interactions can be neglected here on the time-scale of the NMR experiment. Organic molecules soluble in organic solvents (such as $d_6$-DMSO) were analyzed by solution NMR spectroscopy with regard to phase purity and identification. $^{1}H$, $^{13}C$ and $^{15}N$ spectra were recorded on a Varian Gemini 200, Varian Gemini 300, Bruker DRX 200, Bruker AMX 400 and Bruker AMX 600. TMS ($^{1}H$, $^{13}C$) and nitromethane ($^{15}N$/ $^{14}N$) were used as external standards. Measurements were carried out by Christine Neumann, Peter Meyer and Prof. Konstantin Karaghiosoff.

## 2.6 Infrared Spectroscopy (IR)[164]

IR spectroscopy is based on the fact that the energies of the most common vibrational transitions of molecules (covalently bonded atom groups) are located in the IR-range of the electromagnetic spectrum. IR spectra in the range of 650 – 4000 $cm^{-1}$ were recorded on a Spectrum BXII FT-IR spectrometer (Perkin Elmer) equipped with an ATR device (Dura SamplII R II diamond, by Smith Detection).

## 2.7 Atomic Force Microscopy (AFM)[165]

Atomic force microscopy (AFM) gives information about the height profile and morphology of a sample. Resolution in both vertical and lateral directions is on the order of a fraction of a nanometer. A cantilever scans over the sample controlled by piezo-electronic elements. When the surface diversifies during the scan process, the cantilever changes its orientation in *z*-direction, which is registered by a laser system and a photodiode. A computer collects the data to construct a three dimensional image of the sample. The samples were spincoated on Si-Wafers and AFM images were recorded on an Asylum Research MFP 3D Stand Alone in “tapping mode”.

## 2.8 Mass Spectrometry (MS)[164]

In mass spectrometry (MS) ions are generated from a sample which are separated by mass and electric charge and registered by a detector. Molecular ions, quasi molecular ions and cluster ions can arise from the sample during the ionization process. Fragmentation occurs only as a secondary process. The individual MS methods differ in ion sources, separating processes and detector systems. All measurements were done by Dr. Werner Spahl and Brigitte Tschuk.

## 2.9 Differential Thermal/Thermogravimetric Analysis (DTA-TG)

In differential thermal analysis the temperature of a sample is compared with an inert reference material, both heated with the same rate. The change of mass as a function of temperature is measured in a thermogravimetric experiment. For a combined DTA-TG measurement, a thermoanalyzer TGA- 92-2400 (Seteram) with a DTA system was used. All samples were heated with a rate of 1 °C · $min^{-1}$ from RT to 800

°C, while the sample was contained in an unsealed $Al_2O_3$ crucible and the measurements were conducted under helium atmosphere. The results were evaluated with device specific software (Data Acquisition). All measurements were carried out by Sophia Makowksi.

## 2.10 Elemental analysis: CHNS and Inductively coupled plasma atomic emission spectroscopy (ICP-AES)

The elements H, N, C were determined by oxidative pulping of the exactly weighted-samples with He as carrier gas. Subsequently $CO_2$, $H_2O$ and $N_2$were detected separately using a thermal conductivity detector. All these processes were carried out with an elementar analyzer system VARIO EL by the microanalytical laboratory of the Department of Chemistry (LMU). The weight percent of bromine was analyzed by oxidative pulping, followed by potentiometric titration (Metrohm 888 Titrando) of the evolved hydrogen bromide. The quantitative determination of the metals was carried out by inductively coupled plasma emission spectrometry (ICP-AES). Here, the wavelength of transition states is recorded between the outer shells of an atom. The elements are evaporated at very high temperatures, whereby the atoms in the molecules dissociate into ions and atoms. These generated atoms emit at wavelengths which are specific for each element. By comparison with a reference, quantitative statements about the content of the elements are possible. The zinc content was measured on the wavelengths 202.548 nm and 213.857 nm, respectively. All measurements were done by Hartmut Hartl (LMU-Munich), or Marie Luise Schreiber (MPI-FKF Stuttgart).

# 3 Operative procedures

## 3.1 Orbital Shaker

For exfoliation of samples into nanosheets two orbital shakers from GFL (type GFL 3005 and type GFL 3017, Gesellschaft für Labortechnik GmbH, Burgwedel), were used.

## 3.2 Ultrasonic Bath

Exfoliation was also effected with an ultrasonic bath (*Elmasonic S 100 H* ultrasonic) with a power of 550 W and a tank volume of 9.5 liters (Elma Hans Schmidbauer GmbH & Co. KG, Singen).

## 3.3 Furnace

Solid-state reactions were carried out in sealed glass ampoules under vacuum or argon in a home-built tube furnace with an Eurotherm control module.

## 3.4 Centrifuge

To collect products from reactions carried out in organic solvents, the solvents were removed from the product by a centrifuge type Sigma 3-30K Spin control Comfort (Co. Sigma Laborzentrifugen GmbH, Osterode am Harz),with a fixed angle rotor (no. 12158) at a maximum angular frequency of 26,200 rpm and a maximum gravitational force of 60,628 x g.

## 3.5 Spin coating

To produce smooth thin films for AFM measurements, the samples were spin-coated on substrates such as silicon wafers. Spincoating was performed on a WS-650SZ-6NPP/LITE spin coater (Laurell Technologies Corporation).

## 3.6 Chemicals

All chemicals used are listed in Table 3.1.They were purchased from commercial sources and used without further purification.

**Table 3.1** Source of supply and purity of the chemicals used in this work.

| Chemical | Formula | Purity | Supplier |
|---|---|---|---|
| Aceticacid | $C_2H_4O_2$ | p.a. | Bisterfeld-Graen |
| 1H-Benzimidazole | $C_7H_6N_2$ | 99% | AlfaAesar |
| 5-Bromo-1H-benzimidazole | $C_7H_5BrN_2$ | 97% | Aldrich |
| Butanoicacid | $C_4H_8O_2$ | 99% | AlfaAesar |
| Cetyltrimethylammoniumbromide (CTAB) | $C_{19}H_{42}NBr$ | 98% | Fluka |
| Cetyltrimethylammoniumchloride (CTAC) | $C_{19}H_{42}NCl$ | 98% | Molekula |
| Chloroform | $CHCl_3$ | p.a. | Merck |
| 2-Chloromethylbenzimidazole | $C_8H_7ClN_2$ | 96% | AlfaAesar |
| Decyltrimethylammoniumbromide (DTAB) | $C_{13}H_{30}NBr$ | 98% | Aldrich |
| Dodecyltrimethylammoniumbromide (DTAB) | $C_{15}H_{34}NBr$ | 98% | Aldrich |
| Ethanol | $C_2H_6O$ | p.a. | Aldrich |
| *n*-Heptane | $C_7H_{16}$ | 99% | Merck |
| 1-Hexanol | $C_6H_{14}O$ | 98% | Aldrich |
| Imidazole | $C_3H_4N_2$ | 99% | Aldrich |
| 2-Methylimidazole | $C_4H_6N_2$ | 99% | Aldrich |
| 5-Nitrobenzimidazole | $C_7H_5N_3O_2$ | 98% | AlfaAesar |

| Chemical | Formula | Purity | Supplier |
|---|---|---|---|
| Sodium azide | $NaN_3$ | 99% | AcrosOrganics |
| Sodiumnitrite | $NNaO_2$ | 99% | Appl. Chem |
| Tetradecyltrimethylammoniumbromide (TTAB) | $C_{17}H_{38}NBr$ | 98% | Aldrich |
| Tetrahydrofurane | $C_4H_8O$ | p.a. | AcrosOrganics |
| Toluene | $C_7H_8$ | p.a. | Merck |
| Trimethyloctadecylammoniumbromide (TMODA) | $C_{21}H_{46}NBr$ | 98% | Aldrich |
| Zincacetatedihydrate | $C_4H_{10}O_6Zn$ | 99.5 | Merck |
| Zincoxide | ZnO | puriss. | Merck |
| Zincpropionate | $C_6H_{10}O_4Zn$ | 98% | AlfaAesar |

# 4 Towards Mesostructured Zinc Imidazolate Frameworks

**This chapter is based on the article "Towards Mesostructured Zinc Imidazolate Frameworks", published as a highlight in *Chemistry – a European Journal, 2012, 18 (7), 2143-2152* by Sebastian C. Junggeburth, Katharina Schwinghammer, Kulpreet S.Virdi, Christina Scheu and Bettina V. Lotsch.[166]**

## 4.1 Abstract

The transfer of supramolecular templating to the realm of metal-organic frameworks opens up new avenues to the design of novel hierarchically structured materials. We demonstrate the first synthesis of mesostructured zinc imidazolates in the presence of the cationic surfactant CTAB, which acts as a template giving rise to ordered lamellar hybrid materials. A high degree of order spanning the atomic and mesoscale was ascertained by powder X-ray diffraction, electron diffraction, as well as solid-state NMR and IR spectroscopy. The metrics of the unit cells obtained for the zinc methylimidazolate and imidazolate species are $a$ = 11.43±0.45 Å, $b$ = 9.55±0.35 Å, $c$ = 27.19±0.34 Å, and $a$ = 10.98±0.90 Å, $b$ = 8.95±0.95 Å, $c$ =26.33±0.34 Å, respectively, assuming orthorhombic symmetry. The derived structure model is consistent with a mesolamellar structure composed of bromine terminated zinc (methyl)imidazolate chains interleaved with motionally rigid cationic surfactant molecules in all-*trans* conformation. The hybrid materials exhibit unusually high thermal stability up to 300 °C, at which point CTAB is lost and evidence for a thermally induced transformation into poorly crystalline mesostructures with larger feature sizes is obtained. Treatment with ethanol effects the extraction of CTAB from

the material, followed by facile transformation into pure microporous ZIF-8 nanoparticles within minutes, thus demonstrating a unique transition from a mesostructured into a microporous zinc imidazolate.

## 4.2 Introduction

In recent years, metal-organic frameworks (MOFs) have garnered attention owing to their exceptional porosity and hence, application potential, and continue to intrigue due to their rational synthesis and plethora of intricate framework topologies.[61] Although currently a major thrust in MOF chemistry is the extension of pore sizes from the micropore to the mesopore regime, only a limited number of MOFs with pore sizes larger than 2 nm have been reported to date.[167-170] Along similar lines, the design of hierarchical MOFs with bimodal pore size distributions featuring micro- and mesopores would be highly desirable for applications where facile diffusion of molecules, coupled with molecular specificity, is a key requirement, such as in catalysis.[171-172] As opposed to MOFs, siliceous materials constitute an abundant class of compounds that cover different pore size regimes by featuring topologies on the micro-, meso- and macroscale, where microporous zeolites and mesoporous silica are amongst the most famous representatives of ordered porous materials.[34-35] While zeolites comprise 3D crystalline silicate and alumosilicate frameworks with pore sizes typically below 2 nm, periodic mesoporous silica (PMS) are replicas of liquid crystal-like mesophases. They combine periodic order on the nanoscale through arrays of mesopores composed of amorphous silica walls. Since their discovery by Kresge and co-workers at Mobile in 1992, PMS of the MCM (mobile compound of matter) type excel by their ease of synthesis, versatility, and chemical as well as thermal robustness.[34-35] Depending on subtle variations in the reaction conditions,

such as temperature, precursor ratio and pH, hexagonal (MCM-41), cubic (MCM-48),[34] and lamellar (MCM-50)[173] mesophases can be obtained, and myriad silica and non-silica mesophases have been realized to date.

Given the successful track record of supramolecular templating for the design of mesostructured materials, the transfer of mesophase synthesis to the realm of microporous materials in general and metal-organic frameworks in particular is intriguing. Among the few examples of mesostructured coordination frameworks reported so far is a Prussian Blue analogue obtained from specifically designed cationic templates.[174] Metallomesogens constitute a closely related class of compounds, featuring metal-containing ionic liquids with predominantly lamellar structures, where metallo-supramolecular metal-ligand arrays are sandwiched between amphiphile layers. These organic-inorganic hybrid architectures, which have been prepared, for example, from alkylimidazolium surfactants and various metal salts, combine liquid crystal templating with coordination chemistry, yet often at the expense of stable, highly condensed structures.[175-176]

Recently, Ryoo et al. have developed an interesting class of hierarchically micro- and mesoporous MFI zeolite nanosheets stacked into pillared arrays mediated by gemini-type surfactants.[177-178] Along similar lines, hierarchically porous silicates were obtained from layered zeolites pillared by arylic silsesquioxanes, thus generating multifunctional hybrid materials combining acidic and basic properties in the inorganic and organic compartments of the structure, respectively.[179]

Similar biphase architectures may be expected for a subclass of MOFs that combines coordinative bonds with zeolite-like topologies, christened zeolitic imidazolate

frameworks (ZIFs).[100-101, 180] Owing to the formal replacement of the bridging oxygen in zeolites by imidazolate (IM) units, the cages and hence, pores in ZIFs are augmented versions of the secondary building units in zeolites. As the local geometry, in particular the bonding angle of the Zn-IM-Zn units in ZIFs largely corresponds to the Si-O-Si linkage in zeolites, the design of zinc imidazolate (Zn-IM) analogues of MCM-type or even hierarchically porous mesophases in the presence of a structure-directing agent appears highly plausible. The chemical diversity of imidazolate-derived ligands containing functional groups renders zinc imidazolates inherently functional, as opposed to pure mesoporous silica architectures. Whereas the latter typically have to be converted into their surface-modified analogues by post-functionalization,[123, 181] the corresponding mesostructured zinc imidazolates bear functional groups already homogeneously attached to the framework.

Considering the well-established structural analogy between zeolites and ZIFs on the one hand, and the large family of periodic mesoporous silicates and mesolamellar zeolites on the other hand, we would like to address the elusive class of mesostructured imidazolate frameworks, dubbed **MIFs**. Although these hybrid materials present bimodal organization rather than hierarchical porosity, they may nevertheless lay the grounds for the future synthesis of micro- and mesoporous metal-organic frameworks.

Here we report on the synthesis and characterization of the first lamellar **MIF** species and document their close relationship to microporous zeolitic imidazolate frameworks.

## 4.3 Results and Discussion

### *4.3.1* Synthesis and Characterization

In an attempt to study the nucleation and growth of ZIFs using micellar nanoscale reactors, a zinc precursor and imidazole ligand were combined under reverse microemulsion conditions using CTAB, CTAC or other trimethylalkylammonium bromide surfactants with C10 to C18 alkyl chains as emulsifiers.[139] Reflux of the microemulsion at 100 °C for 2 h furnished a white precipitate, which was isolated and washed to remove excess surfactant. The ligand to metal ratio significantly affects the product composition in the system Zn/MeIM/CTAB, leading to ZIF-8 for a 2 : 1 ratio, while a new phase, denoted mesostructured imidazolate framework (**MIF-1**) in the following, starts to nucleate at ligand to metal ratios of 1 : 1 and smaller. When using water as a reaction medium instead of heptane/1-hexanol, quantitative formation of ZnO is observed. If CTAC is employed instead of CTAB, a product similar to **MIF-1**, denoted **MIF-3**, is obtained. Reaction of zinc acetate and imidazole (IM) at equimolar amounts under otherwise similar conditions gives rise to a zinc imidazolate species denoted as **MIF-2** in the following.

### 4.3.2 X-ray powder diffraction

The products **MIF-1** (Zn/MeIM/CTAB), **MIF-2** (Zn/IM/CTAB) and **MIF-3** (Zn/MeIM/CTAC) obtained with a ligand to metal ratio of 1 : 1 were characterized by X-ray powder diffraction (XRD) (Fig. 4.1, S1 and S2). All XRD patterns show no resemblance with any of the starting materials, nor do they correspond to the respective ZIFs (ZIF-8 and ZIF-4 for MeIM and IM, respectively),[100] indicating the forma-

tion of new phases and essentially total conversion of the starting materials. Notably, all XRD data exhibit a set of four sharp, equidistant peaks starting at low angles, which are assigned to the (00*l*) series of reflections of a lamellar mesophase. The small peak widths and the appearance of reflections up to the 4th order indicate a rather high degree of long range order along the stacking direction and hence, layer registry.

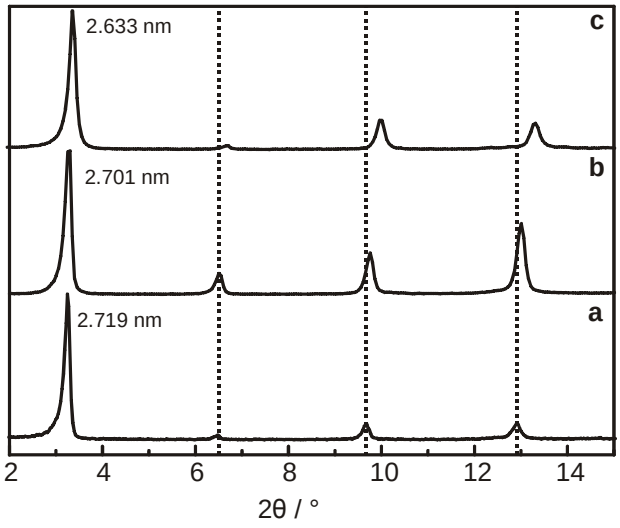


**Figure 4.1** XRD powder patterns of different lamellar **MIFs**: a) CTAB/MeIM (**MIF-1**), b) CTAC/MeIM (**MIF-3**), and c) CTAB/IM (**MIF-2**). The first peaks correspond to the basal spacing of the lamellar mesostructures.

The presumed 001 peaks ($2\theta$ = 4.2° for **MIF-1** and $2\theta$ = 4.4° for **MIF-2**) correspond to lamellar structures with a basal spacing of $d_{001}$ = 27.19 Å for **MIF-1** and $d_{001}$ = 26.33 Å for **MIF-2**, respectively. A similar scenario holds for **MIF-3** ($d_{001}$ = 27.01 Å), thus giving rise to an increasing basal spacing with increasing ligand and halogenide size in the order CTAB/IM < CTAC/MeIM < CTAB/MeIM (Fig. 4.1). This preliminary finding suggests the incorporation of ligand and surfactants, including counter ions, into the as-obtained materials.

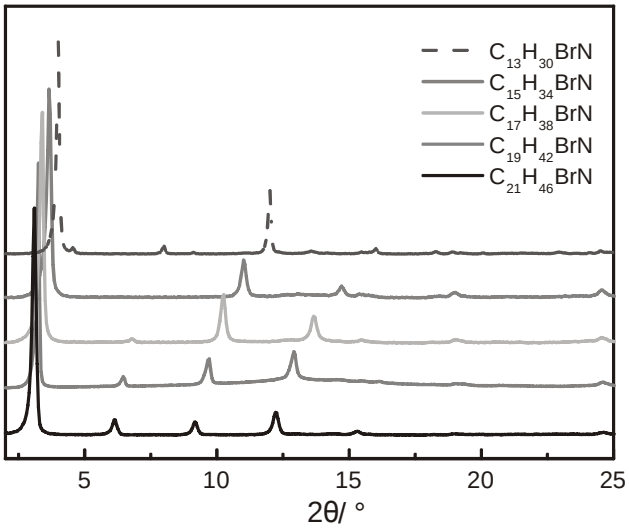


**Figure 4.2** XRD powder patterns of **MIFs** based on MeIM ligands obtained in the presence of different surfactants with varying chain lengths ($C_{13}H_{30}NBr$ - $C_{21}H_{46}NBr$), suggesting the incorporation of the surfactants and their role as templates.

Interestingly, the observed $d_{00l}$ values closely correspond to that of crystalline CTAB[182] ($P2_1/c$, $a$ = 5.638(1) Å, $b$ = 7.260(2) Å, $c$ = 52.072(7) Å; $\beta$ = 93.7°, hence $d_{002} \approx 26.03$ Å, $2\theta \approx 4.4°$), which is known to crystallize with an antiparallel bilayer arrangement of interdigitated hydrophobic chains separated by a polar headgroup layer. For comparison, prototypic MCM-50 silica templated by CTAB exhibits a basal plane spacing of around 31 Å, whereas other lamellar mesophases obtained with CTAB or CTAC as structure directing agents such as zinc phosphates, aluminum phosphates, $GeX_2$/CTAB superstructures (X = S, Se), metallotropic liquid crystals, or zinc oxide, exhibit basal spacings ranging from only 17 Å up to 48 Å.[183-188] The observed variations in basal spacing are generally attributed either to different compositions of the inorganic layer sandwiched between the surfactants, or the formation of phases with different surfactant layer packing (single *vs.* bilayer), or different degrees of interdigitation and tilt angles of the hydrophobic surfactant chains.[187, 189] Notably, for all compounds the intensity of the 002 peaks is lower than

that of all higher order (00*l*) reflections (Fig.4.1), which may be indicative of "accidental extinction" resulting from a particular constellation of scattering factors for the organic and inorganic layers, respectively.[177, 190]

In order to verify the incorporation of surfactant and formation of layered phases templated by the respective surfactant, different mesophases were synthesized in the system MeIM/CTAB using alkylammonium surfactants with different chain lengths ($C_{13}H_{30}NBr$ - $C_{21}H_{46}NBr$). As expected, the (00*l*) reflections for surfactants shorter than CTAB are shifted to higher angles, while those pertaining to surfactants with longer chains are shifted to lower angles (Fig.4.2), which adds evidence to the incorporation of the surfactants into the products and similar geometric arrangements of the different surfactants.

### 4.3.3 IR spectroscopy

The presence of surfactant in the products is also unambiguously evidenced by IR spectroscopy (Fig. 4.3 and 4.4). The strong CH-stretching vibrations of CTAB (CTAC) at 2850 $cm^{-1}$and 2915 $cm^{-1}$ ($\nu(CH_2)$) are the dominating feature of the IR spectra of **MIFs**, whereas the broad $\nu$(NH) stretching region characteristic of solid imidazole and 2-methylimidazole extending from 3200 $cm^{-1}$ down to 1800 $cm^{-1}$ is essentially absent, as analogously found in ZIF-8 and ZIF-4 (Fig. 4.3and4.4).[191] This clearly suggests the presence of deprotonated imidazolate moieties in the products, although different local environments compared to the respective ZIFs are likely as seen by slight shifts in the band positions.

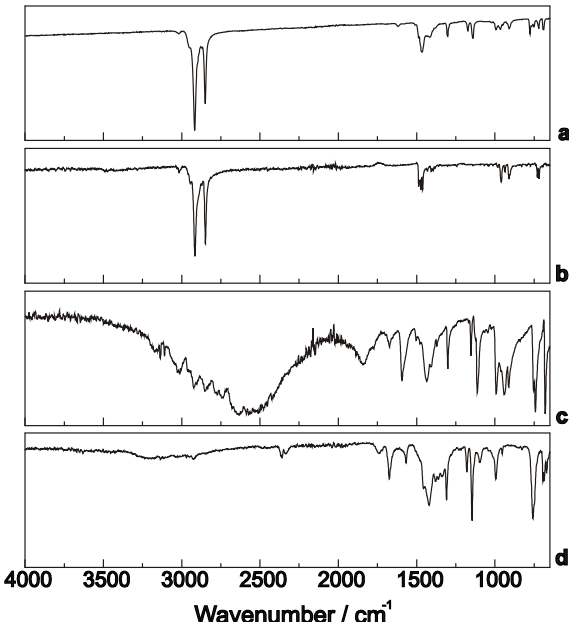


**Figure 4.3** IR spectra of a) **MIF-1** (CTAB/MeIM), b) CTAB, c) MeIM and d) ZIF-8.

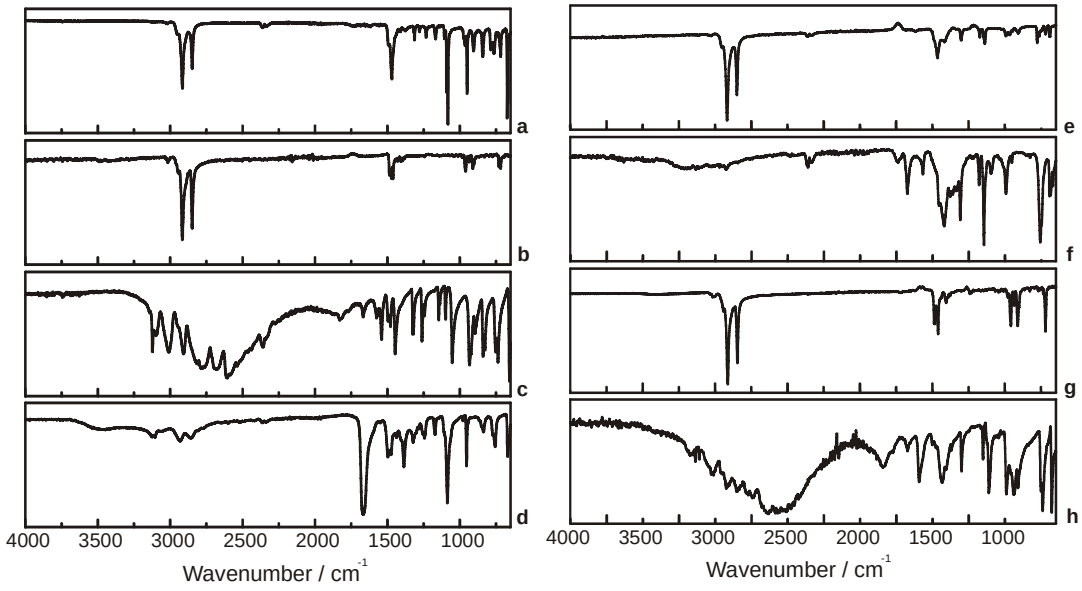


**Figure 4.4** IR spectra of a) **MIF-2** (CTAB/IM), b) CTAB, c) IM(H), d) ZIF-4, e) **MIF-3** (CTAC/MeIM), f) ZIF-8, g) CTAC and h) MeIM(H). The band at 1665 $cm^{-1}$ in d) is due to DMF contained in the pores of non-activated ZIF-4 after synthesis.

### 4.3.4 Solid-state NMR spectroscopy

The solid-state $^{13}C$ CP-MAS NMR spectra of **MIF-1**, **MIF-2**, MeIM/IM and CTAB, as well as that of ZIF-8/ZIF-4 are shown in Figures 4.5 and 4.6. In the following, the NMR spectra of **MIF-1** will be discussed exemplarily, while the major findings equally hold for **MIF-2**. The presence of both CTAB and MeIM is again confirmed, and it is evident that the spectrum ofboth **MIFs** is not a mere overlay of the spectra of their constituents. Two of the three low-field signals pertaining to MeIM (150.1, 148.0 and 124.8 ppm for C3-C1) in **MIF-1** are deshielded with respect to the free, proton-bearing base MeIM (144.1, 125.0 and 115.6 ppm, Tab. 4.1) and show a different splitting pattern. The strongest MeIM signals in **MIF-1** correspond closely to those found in ZIF-8 (150.0 and 125.2 ppm), which suggests complete deprotonation of the MeIM ligand and a similar coordination environment.

The peaks at 150.1/148.0 ppm are both tentatively assigned to C3, yet owing to the observed splitting we infer at least two crystallographically nonequivalent MeIM sites in **MIF-1**.

The above scenario is confirmed by the $^{15}N$ solid-state NMR spectrum recorded for **MIF-1** (Fig. 4.7), which exhibits only two signals, one pertaining to the two nitrogen atoms in MeIM (-169.9 ppm) and the other one to CTAB (-331.3 ppm). This clearly points to the deprotonation of the MeIM moiety, rendering the chemical shifts of the two nitrogen atoms almost identical. However, the width of the MeIM nitrogen is significantly broader (109 Hz) than that of the CTAB nitrogen (29 Hz) and also than the MeIM signal in ZIF-8 at -179 ppm (30 Hz). This finding corroborates the assumption that although the MeIM unit does not bear a proton, the nitrogen atoms are

not equivalent. Furthermore, the MeIM signal in **MIF-1** is shifted downfield with respect to that of MeIM in ZIF-8 by -9.2 ppm. It has been noted earlier that the chemical shift of the basic nitrogen in imidazoles is very sensitive to the local environment and subtle changes in the hydrogen bonding strength. According to these studies, the observed deshielding in **MIF-1** would be consistent with coordination of the imidazole moiety to $Zn^{2+}$ ions, which due to differences in their coordination sphere are slightly less strong Lewis acids than those in ZIF-8.[192-194]

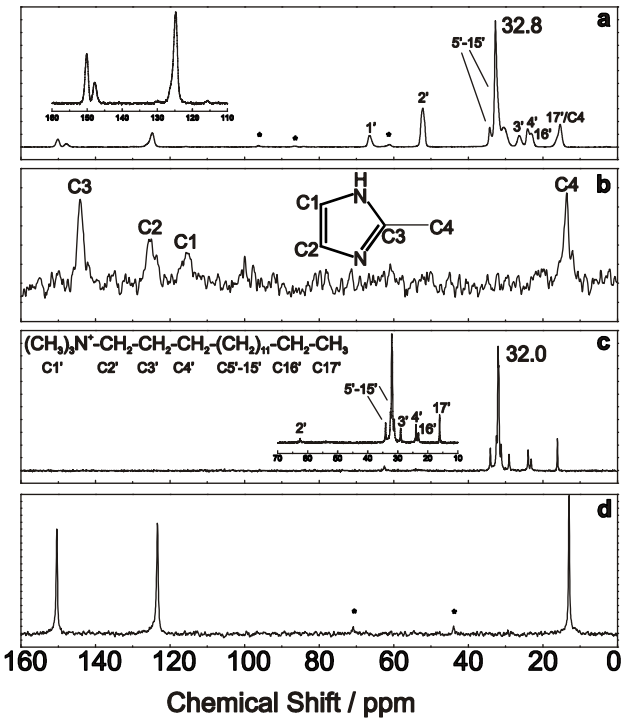


**Figure 4.5** Solid-state $^{13}C$ CP-MAS NMR spectra of a) **MIF-1** (CTAB/MeIM), b) MeIM(H), c) CTAB, d) ZIF-8. Signals marked with an asterisk are spinning-side bands.

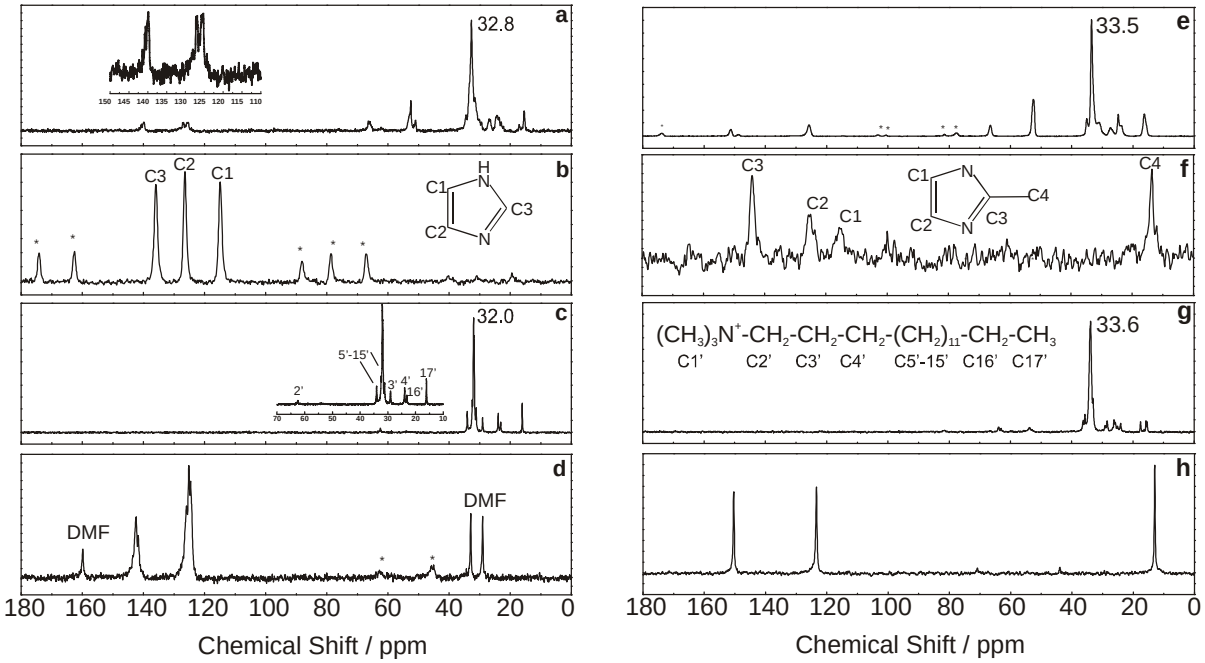


**Figure 4.6** Solid-state $^{13}C$ CP-MAS NMR spectra of a) **MIF-2** (CTAB/IM), b) IM(H), c) CTAB, d) ZIF-4,e) **MIF-3** (CTAC/MeIM), f) MeIM(H), g) CTAC, and h) ZIF-8. Solvent signals belong to DMF contained in the pores of non-activated ZIF-4. Signals marked with an asterisk are spinning-side bands.

**Table 4.1** Experimental $^{13}C$ NMR chemical shifts (in ppm) of ZIF-8, IM(H), MeIM(H), CTAB, CTAC, TTAB, TMODA, and various **MIFs**.

| | ZIF-8 | IM | MeIM | CTAB | CTAC | TTAB | TMODA | **MIF-2**(CTAB/IM) | **MIF-1**(CTAB/MeIM) | **MIF-1B** (TMODA/MeIM) | **MIF-1C** (TTAB/MeIM) | **MIF-3**(CTAC/MeIM) | **MIF-1**(CTAB/MeIM), 320 °C |
|---|---|---|---|---|---|---|---|---|---|---|---|---|---|
| $C_{aromatic}$ | 150.0 | 133.3 | 144.1 | | | | | 140.2 | 150.1 | 149.5 | 150.2 | 151.3 | 145.9 |
| | | | | | | | | | 148.0 | 147.8 | 147.7 | 149.0 | 134.1 |
| | 125.2 | 127.2 | 125.0 | | | | | 126.9 | 124.8 | 125.0 | 124.8 | 126.2 | 125.8 |
| | | | | | | | | 125.3 | | | | | 121.5 |
| | | 113.0 | 115.6 | | | | | | | | | | |
| $C_{aliphatic}$ | | | | 62.5 | 63.9 | 62.5 | 62.5 | 66.4 | 66.5 | 66.6 | 66.5 | 66.6 | |
| | | | | | 63.0 | | | | | | | | |
| | | | | - | 53.8 | 54.7 | | 52.5 | 52.5 | 52.5 | 52.5 | 52.5 | 46.2 |
| | | | | | | | | 51.0 | | | | | |
| | | | | 32.0 | 33.6 | 32.0 | 32.0 | 32.8 | 32.8 | 32.7 | 32.2 | 33.5 | 29.4 |
| | 14.6 | | 13.5 | | | | | | * | * | * | * | |

*The exact assignment of the -$CH_3$ group of MeIM in **1**, **1B**, **1C** and **3** is hampered by signal overlap with the methylene groups of the surfactant.

**Table 4.2** Experimental $^{13}C$ NMR chemical shifts (in ppm) and assignments pertaining to the surfactant moiety in **MIFs** and the respective surfactants CTAB/CTAC.

| | C1 | C2 | C3 | C4 | C5-C15 | C16 | C17 |
|---|---|---|---|---|---|---|---|
| CTAB | - | 62.5 | 29.1 | 23.9 | 31.2-34.1 | 23.1 | 16.1 |
| **MIF-1** CTAB/MeIM | 52.5 | 66.5 | 26.3 | 23.1 | 30.5-34.2 | 23.1 | 15.3 |
| **MIF-2** CTAB/IM | 52.6/51.5 | 66.1 | 26.9 | 23.9 | 29.9-34.2 | 22.8 | 15.3 |
| **MIF-3** CTAC/MeIM | 52.5 | 66.8 | 27.3 | 24.8 | 31.1-35.1 | 23.8 | 16.3 |
| CTAC | 53.8 | 63.9 | 26.2 | 25.0 | 29.1-36.2 | 24.0 | 15.4 |

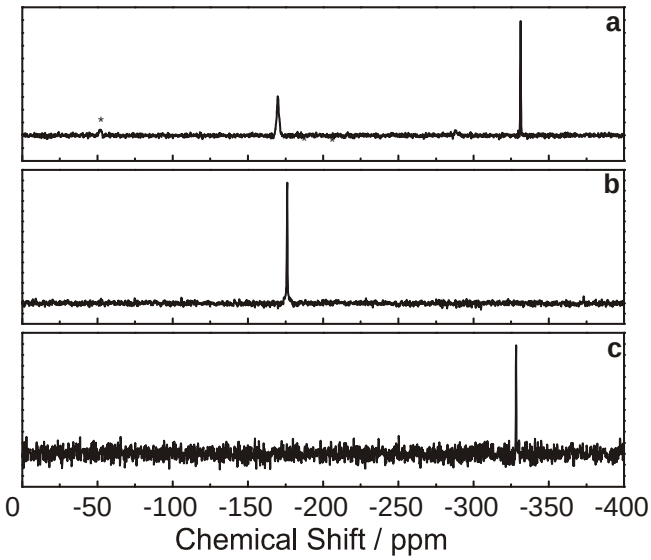


**Figure 4.7** Solid-state $^{15}$N CP-MAS NMR spectra of a) **MIF-1** (CTAB/MeIM), b) ZIF-8, and c) CTAB. Signals marked with an asterisk are spinning-side bands.

It has been pointed out previously that the chemical shifts and peak widths of the different carbon atoms of the surfactant are a sensitive probe of the conformation of the template confined in inorganic hosts and host-guest interfacial interactions.[195-196] The $^{13}$C signals of all **MIFs** show a downfield shift of the inner-chain methylene and terminal carbon of the surfactant chain (C4-C15 and C16 and 17, for labeling see scheme in Fig. 4.5) by about 1-2 ppm with respect to that typically found for CTAB molecules occluded in hexagonal mesostructures, and are consistent with those found for lamellar mesostructures. In particular, a chemical shift of the methylene carbons around 31 ppm has been assigned to a more mobile *gauche* conformation found predominantly in hexagonal mesostructures, whereas a peak at ≈ 33 ppm corresponds to a more rigid all-*trans* conformation, which is found in well-ordered lamellar morphologies.[162, 195] Free CTAB and CTAC with an established all-*trans*-conformation exhibit peaks at 32.0 ppm and 33.6 ppm, respectively. The chemical shifts of the respective methylene carbons in **MIFs-1**/**2** (Fig. 4.5 and 4.6) and **MIF-3** (Fig.4.6) are found around 32.8 ppm and 33.5 ppm, respectively, which clearly indicates a predominant all-

*trans* conformation at room temperature. Furthermore, the chemical shift of the methylene carbon C2 is significantly shifted downfield in all **MIFs** compared to CTAB/CTAC (Table 4.2). This can be taken as evidence of an interaction between the surfactant head groups and the inorganic slabs sandwiched between them.[196] Restricted motion due to an ordered, close packed surfactant arrangement as well as strong interfacial interactions are further confirmed by the high cross-polarization efficiency for C2 and C1 in **MIF-1** compared to the free surfactant,[196-197] as well as by the observed line broadening in **MIF-1** compared to CTAB (115 Hz *vs.* 60 Hz).

### *4.3.5* Elemental analysis

Whereas ZIFs based on bivalent metal ions feature metal to ligand ratios of $[M^{2+}] : [IM^{-}] = 1 : 2$, the rational composition of **MIFs 1**-**3** was consistently and reproducibly determined as $[Zn^{2+}] : [IM^{-}] : [Br^{-}/Cl^{-}] : [CTA^{+}] = 1 : 1 : 2 : 1$ (CTA=$C_{19}H_{42}N^{+}$; Tables 4.3 - 4.8). The Zn : Br ratio of 1 : 2 was further corroborated by energy dispersive X-ray spectroscopy (Fig. 4.9). Hence, the tentative formula of **MIF-1** and **MIF-2** is given by $[Zn(MeIM)_{2/2}Br_2]CTA$ and $[Zn(IM)_{2/2}Br_2]CTA$, respectively. Thus, the incorporation of excess halogenide ions (e.g. CTAB + $Br^{-}$) at the expense of ligand anions with respect to ZIF-8, the assumption of a tetrahedral zinc coordination environment, and electroneutrality arguments require the formation of zinc imidazolate chains $Zn(IM)_{2/2}$ rather than zinc imidazolate networks $Zn(IM)_{4/2}$ as observed in ZIFs. We assume anionic corner-sharing $Zn(IM)_{2/2}Br_2^{-}$ chains electrostatically bonded to positively charged $CTA^{+}$ ions. Similar zinc imidazolate chains, albeit without surfactant templates, have been reported in the literature (see below).[198]

**Table 4.3** Elemental analysis of **MIF-1** with formula M($C_{23}$ $H_{47}Br_2N_3Zn$) = 590.83 g·mol$^{-1}$.

| | **N** | **C** | **H** | **Br** | **Zn** |
|---|---|---|---|---|---|
| 1$^{st}$ sample | 7.15 | 46.69 | 7.82 | 26.96 | 10.43 |
| 2$^{nd}$ sample | 7.05 | 47.42 | 8.06 | 28.22 | 11.39 |
| 3$^{rd}$ sample | 7.16 | 46.86 | 7.84 | 28.41 | 11.50 |
| average | 7.12 | 46.99 | 7.91 | 27.86 | 11.11 |
| calc. | 7.11 | 46.76 | 8.02 | 27.05 | 11.07 |

**Table 4.4** Elemental analysis of **MIF-2** with formula *M*($C_{22}H_{45}Br_2N_3Zn$) = 576.81 g·mol$^{-1}$.

| | **N** | **C** | **H** | **Br** | **Zn** |
|---|---|---|---|---|---|
| exp. | 7.33 | 45.73 | 7.57 | 27.98 | 11.45 |
| calc. | 7.28 | 45.81 | 7.28 | 27.71 | 11.33 |

**Table 4.5** Elemental analysis of **MIF-3** in the system (CTAC/MeIM) with formula M($C_{23}$ $H_{47}$ $Cl_2N_3Zn$) = 501.93 g·mol$^{-1}$.

| | **N** | **C** | **H** | **Cl** | **Zn** |
|---|---|---|---|---|---|
| exp. | 8.36 | 55.02 | 9.12 | 14.13 | 13.55 |
| calc. | 8.37 | 55.04 | 9.44 | 14.13 | 13.03 |

**Table 4.6** Elemental analysis of **MIF-1**A in the system TMODA/MeIM with formula M($C_{25}H_{51}Br_2N_3Zn$) = 618.89 g·mol$^{-1}$.

| | **N** | **C** | **H** | **Br** | **Zn** |
|---|---|---|---|---|---|
| exp. | 6.70 | 49.10 | 8.50 | 26.87 | 10.17 |
| calc. | 6.79 | 48.52 | 8.31 | 25.82 | 10.56 |

**Table 4.7** Elemental analysis of **MIF-1**B in the system TTAB /MeIM with formula M($C_{21}H_{43}Br_2N_3Zn$) = 562.78 g·mol$^{-1}$.

| | **N** | **C** | **H** | **Br** | **Zn** |
|---|---|---|---|---|---|
| exp. | 7.44 | 45.04 | 7.89 | 29.39 | 11.40 |
| calc. | 7.47 | 44.82 | 7.70 | 28.4 | 11.62 |

**Table 4.8** Elemental analysis of **MIF-1**C in the system DTAB/MeIM with formula $M(C_{19}H_{39}Br_2N_3Zn)$ = 534.7268 $g \cdot mol^{-1}$.

| | **N** | **C** | **H** | **Br** | **Zn** |
|---|---|---|---|---|---|
| exp. | 7.80 | 42.96 | 7.39 | 30.08 | 11.77 |
| calc. | 7.86 | 42.68 | 7.35 | 29.89 | 12.23 |

### 4.3.6 **Transmission electron microscopy**

The information extractable from the XRD patterns, measured in reflection mode, was limited by the preferred orientation of the lamellae perpendicular to the [001] direction. Therefore, SAD experiments were conducted in TEM to gather in-plane information about the crystal structure. As has been reported for similar lamellar mesophases,[146] **MIFs** are extremely unstable under the electron beam and hence, imaging by TEM was strongly hampered. Most of the areas imaged implied the region to be amorphous, which can be attributed to electron beam damage induced destruction of the structure. However, in some areas the initial crystalline structure and its disintegration could be depicted with SAD by a rapid change in the diffraction pattern from rectangular arranged spots to diffused rings within seconds.

To extract information on crystallinity, phase purity and possible long range order of the sample, SAD measurements were therefore performed on MeIM and IM structures for very short acquisition times. These SAD patterns unambiguously ascertain the existence of a highly crystalline majority phase in the **MIF** samples studied (Fig. 4.8). The relatively high noise in the patterns can be attributed to the very short acquisition times for capturing the images and the acquisition to be undertaken as soon as the region was exposed to the electron beam.

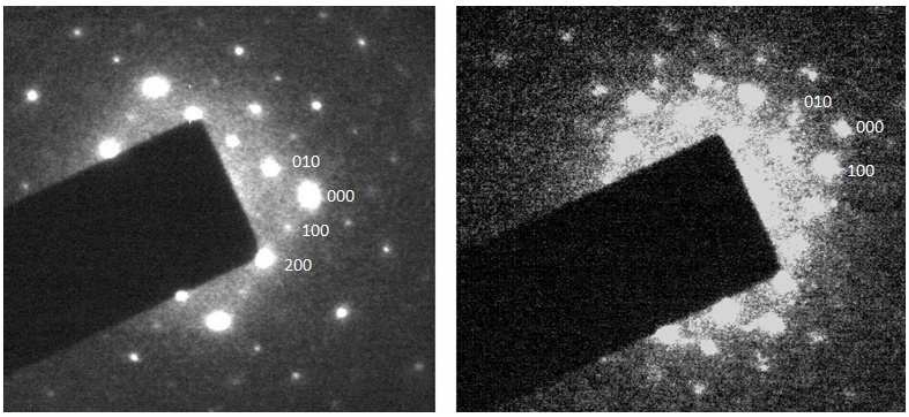


**Figure 4.8** SAD patterns taken parallel to the *c*-axes for **MIF-1** (left) and **MIF-2** (right). Due to beam sensitivity only short acquisition times were possible resulting in highly noisy patterns.

The lattice plane distances $d_{1a}$, $d_{1b}$ for **MIF-1** and $d_{2a}$, $d_{2b}$ for **MIF-2** were determined to be 11.43±0.45 Å, 9.55±0.35 Å and 10.98±0.90 Å, 8.95±0.95 Å respectively (Fig.4.8). The tolerance values for these measurements are considerably higher than in conventional SAD experiments, however beam sensitivity hindered more accurate measurements. The value 10.98 Å has previously been reported as the translational parameter of a zigzag zinc imidazolate chain.[199] As such, we assume that the found values represent the in-plane lattice parameters of the respective unit cells (see below). If we assume the structure to be orthorhombic (see next section) the alternating intensity in the spots in Figure 4.8 (left) likely stems from the symmetry-allowed 200 / 400 reflections giving rise to high intensity and the 100 / 300 reflections resulting in less intensity. For an orthorhombic structure the 100 / 300 reflections are forbidden, however due to the thickness of the sample and dynamic scattering, points representing these planes become visible in electron diffraction patterns with intensities considerably less than the *h00* (*h=2n*) planes. The EDX spectrum from a crystalline domain in **MIF-1** is shown in Figure 4.9, which clearly indicates the presence of Zn and Br.

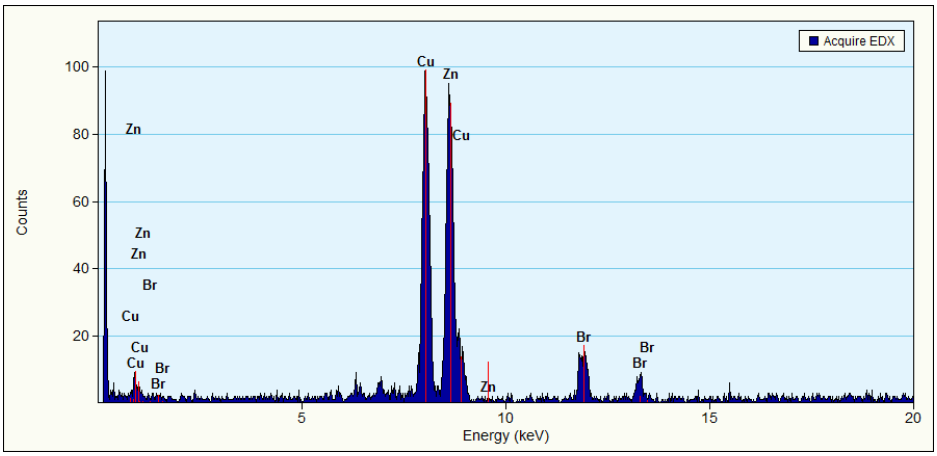


**Figure 4.9** EDX spectrum of **MIF-1** showing the presence of Zn and Br.

### 4.3.7 Structure Discussion

On the basis of the above spectroscopic evidence and diffraction results from TEM, we put forward a tentative model for the structure of **MIF-2** based on simulations using the software package *Materials Studio* (Fig. 4.10).[200] The structures of other **MIFs** may be constructed analogously. According to elemental analysis, we assume Zn-IM chains rather than $Zn(IM)_2$ nets to constitute the inorganic slabs. The metrics of the unit cell can be extracted from XRD and TEM, respectively, yielding $a$ = 10.98 Å and $b$ = 8.95 Å, and $c$ = 26.3 Å. For simplicity, we use a primitive orthorhombic unit cell as working model, although we cannot exclude monoclinic metrics as found in CTAB. Since the observed basal spacing is reminiscent of that in crystalline CTAB, an interdigitated monolayer arrangement featuring an antiparallel stacking of surfactant molecules rather than a tail-to-tail bilayer arrangement likely constitutes the surfactant slab.[182] As stated above, the metrics of the *ab*-plane is consistent with the metrics of an IM-Zn-IM *zigzag*-chain running along the *a* axis. The *b* parameter is then determined by the spacing of adjacent chains, which is influenced by the packing of the surfactant molecules extending along the stacking direction.[199] According to this model, two $[ZnBr_2IM]^-$ units may be accommodated in a single unit cell, which requires two $CTA^+$ molecules according to ele-

mental analysis and for charge compensation. For the Zn-Br bond length within the tetrahedral Zn environment a value of 2.3 Å was adopted according to common Zn-Br bond lengths, and Br···H contacts in our model (3.1 Å) slightly exceed the sum of Van der Waals radii for Br (1.83 Å) and H (1.10 Å).[201-202] H-atoms were added by the software and H···H distances between different alkylchains are set to about 2.5 Å (CTAB: 2.5 Å).

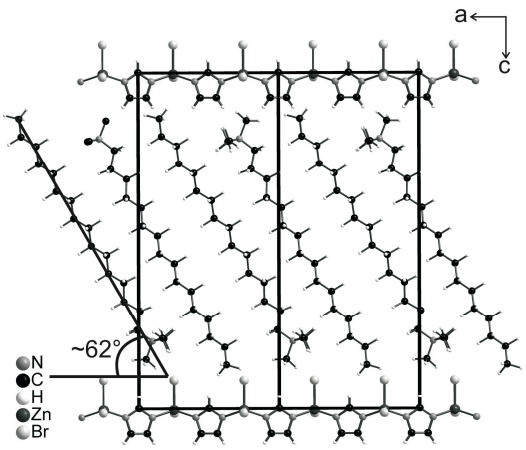


**Figure 4.10** Structural model of **MIF-2** (CTAB/IM) viewed along [010], constructed with the program *Materials Studio*.

Assuming a basal spacing of 26.3 Å obtained from XRD and an *all-trans* conformation of the $CTA^+$ cations ascertained by solid-state NMR, the CTAB molecules have to be inclined with respect to the *c* axis, forming a tilted monolayer arrangement. The tilt angle with the *ab*-plane can be determined by adding up all space increments given by bonds and van der Waals contacts along the *c* axis and taking into account the projected length of the CTAB molecule along the same direction.[203-204] Using this scheme, a tilt angle of roughly ≈ 62° for the $CTA^+$ molecules can be extracted (CTAB: 65°). The SAED results imply a perfect registry between the organic and inorganic slabs, which is rarely observed in lamellar mesophases.

CTAB is characterized by an ABAB-type stacking and hence, the observed (00*l*) reflections are indexed based on the condition 00*l*: $l = 2n$. In principle, we cannot distinguish between an

AAA-type stacking (00*l*: $l = n$) with a basal spacing of 26.3 Å and an ABAB-type stacking with extinction of the 001 reflection due to a glide plane and a doubled basal spacing of 52.6 Å. An AAA-type model structure constructed based on the above considerations is shown in Fig. 4.10. Although details of the structure such as conformation and tilting of the Zn-IM chain, exact $CTA^+$ tilt angle and, in particular, the relative arrangement of the $CTA^+$ and $[ZnBr_2IM]^-$ units cannot be predicted unambiguously based on the data available, the proposed arrangement represents a reasonable model consistent with the experimental data, including powder XRD (Fig.4.11).

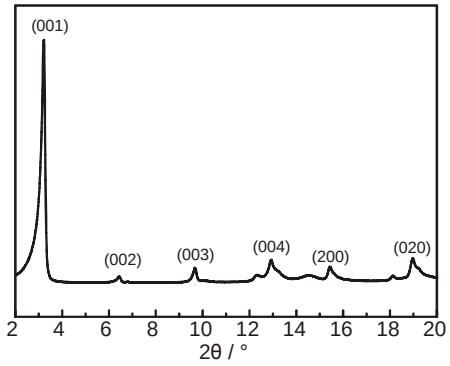


**Figure4.11** Indexing of a XRD powder pattern of **MIF-1** (CTAB/MeIM) measured in a rotating glass-capillary in Debye-Scherrer geometry.

### 4.3.8 **Thermal behaviour**

The thermal behaviour was investigated *in situ* by combined DTA-TG measurements (Fig. 4.12 and 4.13) as well as *ex situ* experiments in sealed glass ampoules.A slight mass loss (6%) associated with an endothermic event is seen around 210 °C in **MIF-1**, followed by further decomposition in two steps at 300-350 °C (mass loss of 44%) and above 420 °C. Mass loss in **MIF-2** is less well resolved and proceeds in three broad steps between 210 °C and 450 °C. The mass loss slightly above 200 °C may be due to the commencing decomposition of CTAB into cetylbromide and trimethylamine and subsequent gradual loss of the

decomposition product (boiling point of cetylbromide: 190 °C) as observed in pure CTAB (Fig. 4.12b).

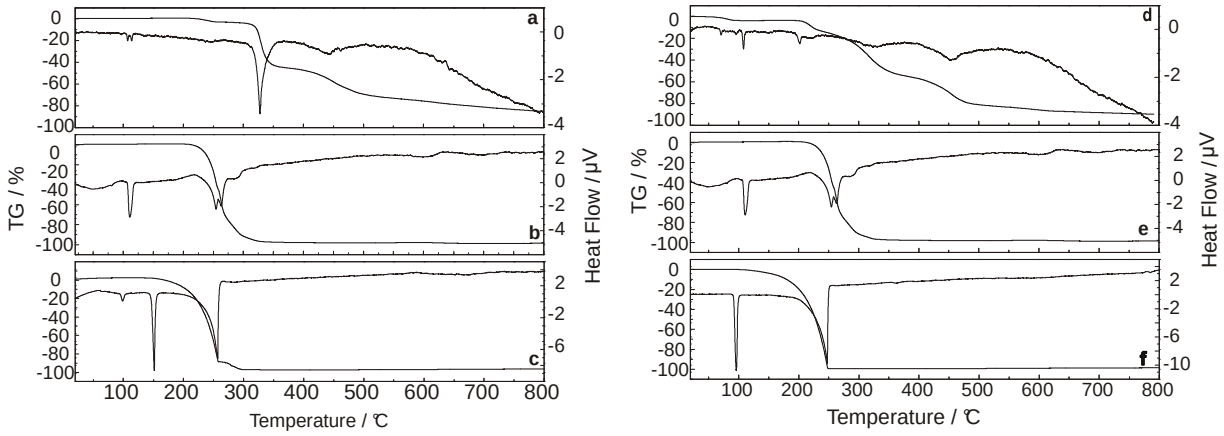


**Figure 4.12** DTA/TG of a) **MIF-1** (CTAB/MeIM), b) CTAB, c) MeIM(H) d) **MIF-2** (CTAB/IM), e) CTAB and f) IM(H).

Notably, the thermal stability of all **MIFs** exceeds that of the individual components (MeIM/IM and CTAB/CTAC, respectively) alone, indicating an exceptional thermal robustness of the hybrid material compared to other lamellar mesophases.[185, 205] Small endothermic events around 100 °C (**MIF-1**) and between 70 and 100 °C (**MIF-2**) may correlate with a reversible *trans* ↔ *gauche* conformational phase transition due to enhanced mobility of the $CTA^+$ chains familiar from other lamellar mesophases.

This is corroborated by *ex situ* XRD studies recorded of **MIF-1** heated in evacuated glass ampoules in steps of 50 °C up to 320 °C. No changes were detectable in the XRD pattern of as-obtained **MIF-1** up to a temperature of 290 °C, at which point decomposition of the samples into a brownish resin commenced. A white sublimate was identified by NMR as CTAB. The amorphous product obtained after heating for 30 min at 320 °C still contains residual CTAB and MeIM as confirmed by IR and solid-state NMR (Fig. 4.14 and 4.15). Based on the TG results and consistent with elemental analysis of the calcinated product, about 70% of CTAB is lost upon calcination up to 320 °C, indicating retention of about 30% within the material

(Tab. 4.9). The XRD patterns of the residue exhibit a small shoulder to the primary beam decay at very small angles (0.6° – 0.8°, *d* values of 14.6 nm – 11.0 nm), which suggests the formation of a disordered mesostructure with a large distribution of pore sizes upon thermal treatment (Fig. 4.16). Porosity may be generated by a rearrangement of the zinc imidazolate chains into 2D or 3D mesophases concomitant with partial CTAB release. However, the observed mesostructure may also be due to textural mesoporosity originating from gradual framework destruction as CTAB and its volatile decomposition products are released.

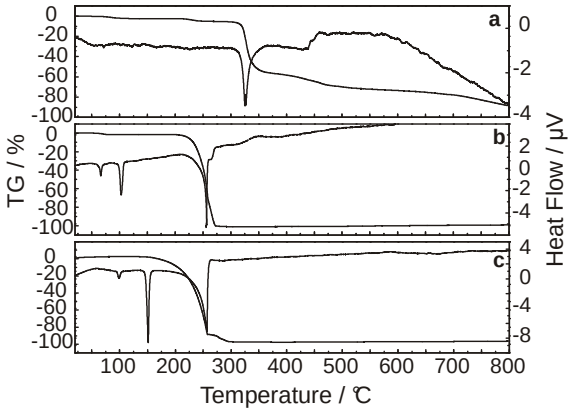


**Figure 4.13** DTA-TG curves of a) **MIF-3** (CTAC/MeIM), b) CTAC and c) MeIM.

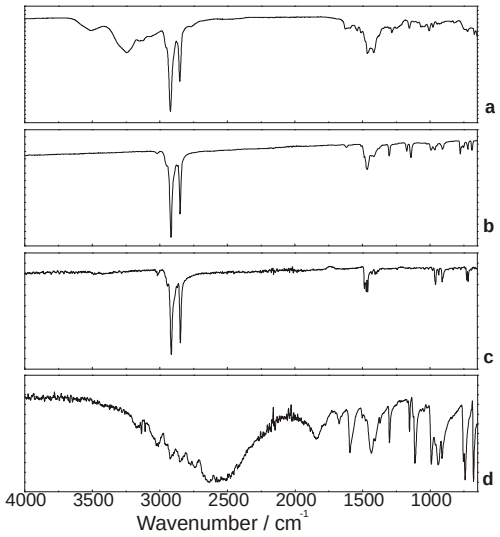


**Figure 4.14** IR spectra of **MIF-1** (CTAB/MeIM) a) heated to 320 °C, b) as-obtained, c) CTAB, and d) MeIM.

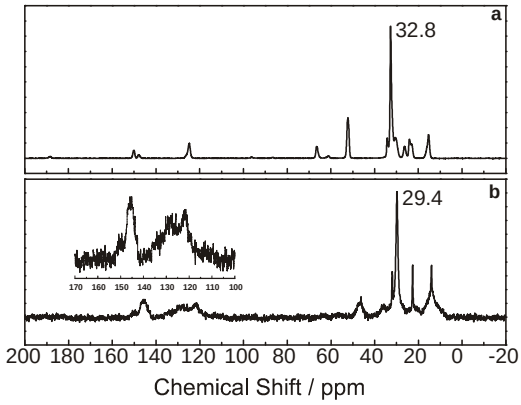


**Figure 4.15** Solid-state $^{13}C$ CP-MAS NMR spectra of **MIF-1** (CTAB/MeIM) a) as-obtained, and b) heated at 320 °C.

**Table 4.9** Elemental analysis of the decomposition product of **MIF-1** after heating at 320 °C, corresponding to the composition $C_{10.7}H_{17.6}Br_{1.3}N_3Zn$. The composition is consistent with that calculated from the DTA/TG data.

| | **N** | **C** | **H** | **Br** | **Zn** |
|---|---|---|---|---|---|
| exp. | 8.12 | 31.95 | 5.24 | 37.97 | 17.27 |
| calc. | 8.25 | 31.70 | 4.80 | 37.72 | 17.74 |

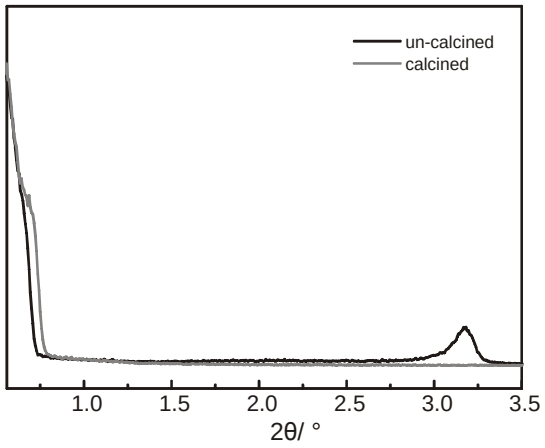


**Figure 4.16** XRD of **MIF-1** (MeIM/CTAB) before calcination (black line) and after calcination (gray line). The rising background below ≈ 0.5° is due to the primary beam.

### 4.3.9 **Conversion into ZIF-8**

In order to explore the framework stability upon removing CTAB, **MIF-1** was treated with ethanol at 100 °C. Remarkably, the obtained product turned out to be pure ZIF-8. Hence, the reaction occurring in ethanol can be described by the following formula:

$$[Zn(MeIM)_{2/2}Br_2]CTA \rightarrow ½\ ZIF\ 8 + ½\ ZnBr_2 + CTAB \qquad (I)$$

**MIF-1** was completely converted to ZIF-8 within 1 h, while when using an ultrasonic bath at 80 °C the reaction was completed within 5 min. The conversion yield is about 80-90%. However, upon treating the lamellar network with strong acids like HBr and HCl in EtOH, it was completely destroyed and a clear solution was obtained.[206] Treatment with mild solvents such as $CHCl_3$ left the structure intact.

Throughout the CTAB extraction process, a white powder was observed at all times, suggesting a heterogeneous transformation of **MIF-1** into ZIF-8. Figures 4.17 and 4.18 outline the structural evolution of ZIF-8 as a function of ethanol treatment time. In the sequence of IR spectra a gradual disappearance of the CTAB C-H stretching bands (2850 $cm^{-1}$/ 2915 $cm^{-1}$) and an increase of the ZIF-8 signature in the fingerprint region is observed.

The formation of ZIF-8 is evidenced in the XRD patterns by the gradual increase of the most prominet ZIF-8 peak (011) as time progressed (Fig. 4.18). At the same time, the intensity of the (00*l*) peaks of **MIF-1** diminish. The onset of ZIF-8 formation is visible even after 5 minutes of ethanol treatment at 100 °C. The fact that sharp ZIF-8 reflections are observed even at short reaction times suggests that the transformation proceeds by direct conversion of **MIF-1** rather than dissolution of **MIF** followed by nucleation and growth of the new phase.

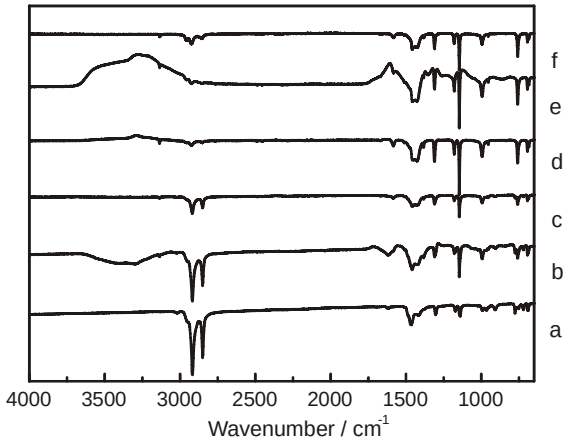


**Figure 4.17** IR spectra obtained after refluxing **MIF-1** in EtOH at 100 °C for different times: a) Untreated, b) 5 min., c) 10 min., d) 1 h, e) 2 h, and f) ZIF-8.

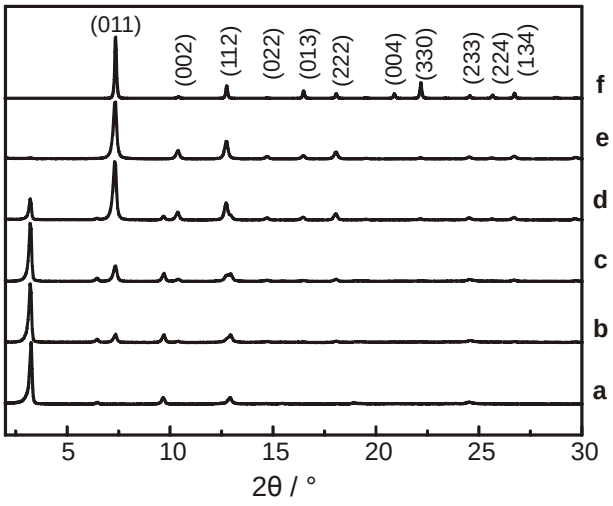


**Figure 4.18** XRD patterns illustrating the structural evolution of ZIF-8 after refluxing **MIF-1** in EtOH at 100 °C for different times. a) Untreated, b) 5 min., c) 10 min., d) 1 h, e) 2 h, and f) simulated powder pattern of ZIF-8.

Accordingly, the intensity of the 011 reflection is consistently higher than that of the 112 and 222 reflections at all times, which is different from a homogeneous nucleation and growth scenario described by Venna *et al.* for the synthesis of ZIF-8 from methanol solutions.[207] Analysis of the 001 (**MIF-1**) and 011 (ZIF-8) peak areas as a function of time reveals an exponential decay or increase, respectively, corresponding to a first-order reaction kinetics (Fig. 4.19). The **MIF-1**→ ZIF-8 transformation was also followed by SEM by taking images

after different ethanol treatment times (Fig. 4.20). Unreacted **MIF-1** exhibits a characteristic platelet-like morphology consistent with its lamellar structure. After extraction for 1 h, the coexistence of material with a layer-like morphology and particles is visible, whereas after 2 h only agglomerates of particulate material are observed. From these images, we infer the gradual formation of rather monodisperse, spherical ZIF-8 nanoparticles with dimensions around 100 nm from an intermediate stage of ZIF-8 particles embedded in a matrix of unreacted lamellar **MIF-1**.

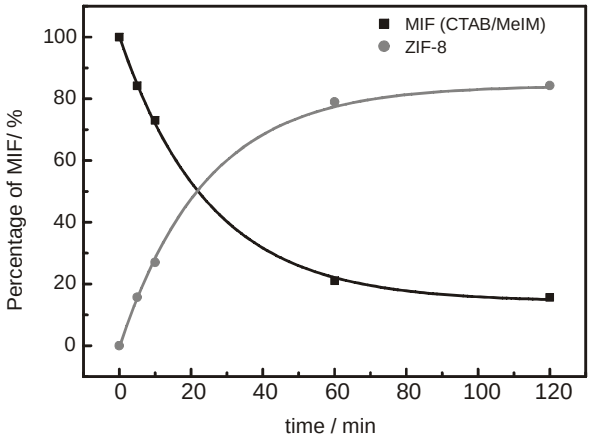


**Figure 4.19** Kinetics of the transformation of **MIF-1** (MeIM/CTAB) into ZIF-8 as a function of time. % conversion was calculated by integrating the area under the 011 and 001 peaks of ZIF-8 and **MIF-1**, respectively.

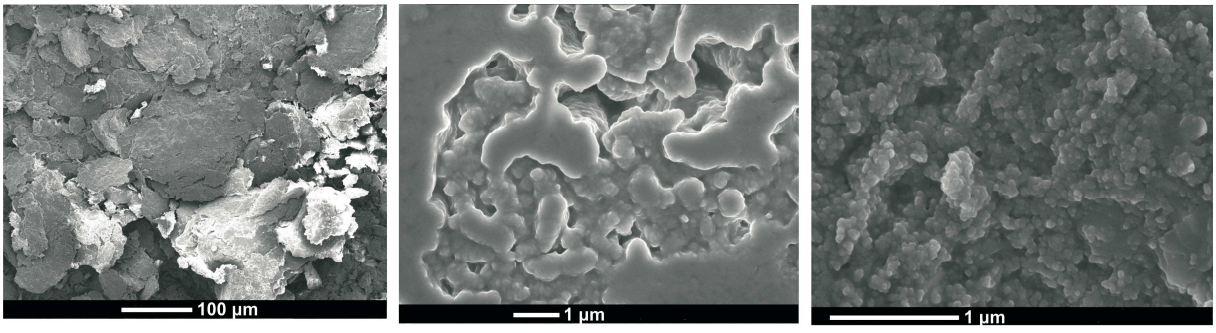


**Figure 4.20** SEM images of **MIF-1** treated with EtOH at 100 °C for different times. Untreated (left), 1 h (middle), 2 h (right). Note the different length scales.

### 4.3.10 Discussion

The facile transformation of **MIF-1** into ZIF-8 without prior dissolution of the starting material suggests a close topological relationship between the zinc imidazolate network in **MIF-1** and ZIF-8. Hence, **MIFs** may be considered a metastable precursor for ZIFs, the latter being generated by extraction of CTAB from the interlayer space. In addition, the transformation may be considered an alternative pathway for the synthesis of ZIF nanocrystals, which is feasible in different solvents and under a range of reaction conditions. Nevertheless, the stoichiometry of **MIFs** found by elemental analysis and EDX does not allow for $Zn(IM)_2$-type networks with connectivities in three dimensions. 1D zinc imidazolate chains terminated by bromine ions on either side account for both the observed elemental composition and geometric requirements: The inorganic slabs sandwiched between the surfactants show layer thicknesses around 5.4 Å, consistent with an interdigitated CTAB monolayer, which is likewise found in CTAB and several other metallomesogens based on, for example, the $[Zn(C_nH_{2n-1}IM)_2Cl_2]$ moiety.[198] The observed exceptional thermal stability of the lamellar **MIFs** is further testament to the strong electrostatic interaction between the Zn-IM chains and cationic surfactants, which is consistent with anionic $[Zn(IM)_{2/2}Br_2]^-$ chains sandwiched between cationic $CTA^+$ molecules “glueing” them together. This could also explain the fact that even at temperatures as high as 320 °C, still about 30% of CTAB is retained in the structure. The observation of crystalline domains in the **MIF** samples by SAED is remarkable, as it implies a periodic mesophase which is not only ordered on the mesoscale like MCM-type materials, but in addition it exhibits translational order on the atomic scale. In general, this type of ordered arrangement on two different lengthscales is barely found in mesophase materials.[208] Also, the observed crystallinity implies excellent layer registry between

the inorganic and organic slabs, which is consistent with strong interactions at the inorganic-surfactant interface as suggested by our model.

## 4.4 Conclusion

With the above first example of a zinc imidazolate mesophase we have transferred the concept of mesostructured silica materials to zinc imidazolates, which is rationalized by the similar Si-O-Si and Zn-IM-Zn bonding geometries. Thus, the structural analogy between microporous ZIFs and zeolites has been demonstrated to also hold for mesostructured silica materials on the one hand, and mesostructured zinc imidazolate coordination networks on the other hand. Comprehensive characterization of the obtained **MIF** materials gives evidence of a lamellar hybrid structure composed of bromine-terminated zinc imidazolate chains, which are sandwiched by cationic surfactant layers. The observed facile *in situ* transformation into ZIF-8 nanocrystals suggests a close topological relationship between **MIFs** and ZIFs, thus boding well for a new generation of mesostructured imidazolate frameworks derived from different types of imidazolate linkers. What is more, **MIFs** can adopt a range of functional groups attached to the imidazole linkers, demonstrated here by the use of methylimidazole, which are introduced into the framework in a one-step reaction and homogeneously distributed, rendering post-modification and grafting reactions as familiar from functionalized silica materials unnecessary. Although evidence for the transformation of mesoporous into microporous materials is still pending, the grounds have been laid for further studies in this system, which will include the synthesis of 2D and 3D zinc imidazolate mesophases and surfactant removal in order to liberate mesoporous imidazolate frameworks.

## 4.5 Experimental Section

Cetyltrimethylammonium bromide (CTAB, $C_{19}H_{42}NBr$, Fluka 98%), cetyltrimethylammonium chloride (CTAC, $C_{19}H_{42}NCl$, Molekula), decyltrimethylammonium bromide (DTAB, $C_{13}H_{30}NBr$), tetradecyltrimethylammonium bromide (TTAB, $C_{17}H_{38}NBr$), dodecyltrimethylammonium bromide (DTAB, $C_{15}H_{34}NBr$), trimethyloctadecylammonium bromide (TMODA, $C_{21}H_{46}NBr$, all Aldrich, 98%), imidazole, 2-methylimidazole (both Aldrich, 99%), 1-hexanol (Aldrich, 98%), *n*-heptane (99%), chloroform (Merck, p.a.), and zinc acetate dihydrate ($Zn(OAc)_2 \cdot 2H_2O$, Merck, 99.5%) were purchased from commercial sources and used without further purification.

*Syntheses.* Two separate microemulsions were formed by adding 0.10 M aqueous IM/MeIM (675 μL) and 0.10 M aqueous zinc acetate dihydrate (675 μL) to two separate mixtures containing 0.05 M CTAB (0.993 g), 0.50 M 1-hexanol, and 0.50 M *n*-heptane (50 mL each). The separated microemulsions were stirred vigorously for 10 min at room temperature, subsequently combined and refluxed at 100 °C for 2 h. When using MeIM a white precipitate can be observed after 5 min of stirring, while a white precipitate is observed when using IM after cooling to room temperature. The white powder was isolated by centrifugation at 13 000 rpm for 10 min, and washed with cold ethanol or chloroform. The yield of the air-dried powder was 35 mg (90 %). For surfactants other than CTAB the same concentrations were used. ZIF-8 was obtained by reaction of MeIM and zinc nitrate in methanol according to literature protocols.[146] ZIF-4 was produced according to the procedure described by *Park et al.*[100] CTAB extraction experiments with ethanol were performed by refluxing (100 °C oil-bath temperature) **MIF** (400 mg) in ethanol (25 mL) for up to 24 h in a round bottom flask.

*Instrumental.* Combined differential thermal and thermogravimetric analyses (DTA/TG) were carried out on a TG-DTA thermo balance (type 92-2400, Setaram). All samples were heated at a rate of 3 °C $min^{-1}$ under a helium atmosphere. Powder X-ray diffraction (XRD) data were collected on a D8 diffractometer (Bruker) and Stadi P powder diffractometer (Stoe), both using Cu-$K_{\alpha 1}$ radiation. Infrared (IR) spectra in the range 650 - 4000 $cm^{-1}$ were recorded in reflection geometry using a Spectrum BXII FT-IR spectrometer (Perkin Elmer) equipped with a DuraSamplIR II diamond ATR device (Smith Detection). Determination of the elements H, C, N, Cl and Br was carried out by oxidative pulping using a commercial elemental analyzer system with helium as carrier gas (VARIO EL, Elementar Analysensysteme GmbH). The zinc content was determined by inductively coupled plasma atomic emission spectrscopy (ICP-AES) on a VISTA simultan spectrometer (Varian). A JSM-6500F scanning electron microscope (SEM, Jeol) with integrated EDX detector (Oxford type 7418) was used to obtain particle size and morphology information. The software package Material Studio 5.5 (Accelrys) was used for setting up a suitable structural model. $^{13}C$ and $^{15}N$ solid-state cross polarization magic angle spinning nuclear magnetic resonance (CP-MAS NMR) spectra were recorded at room temperature with a DSX Avance 500 FT spectrometer (Bruker) equipped with a commercial 4 mm MAS NMR double-resonance probe at a magnetic field of 11.7 T, the chemical shifts being referenced with respect to TMS ($^{13}C$) and nitromethane ($^{15}N$) as external standards. The different NMR parameters for the single measurements are summarized in Table S1 (Supporting Information). For transmission electron microscopy, samples were prepared by drop coating the solutions on Cu grids with lacey carbon backing (Plano GmbH). TEM experiments were performed on a JEOL 2011 microscope equipped with a $LaB_6$ thermal source, operated at 200 kV.

## 4.6 Acknowledgements

We thank Dr. Markus Döblinger for TEM measurements and Dr. Steffen Schmidt for technical support and helpful discussions, as well as Christian Minke for EDX, SEM and solid-state NMR measurements. We are indebted to Geraldine Rühl and Danica Radmanovac for practical support. The author KSV would like to thank Elitenetzwerk Bayern for financial support. Financial support by the Nanosystems Initiative Munich (NIM), Center for Nanoscience (CeNS) and Fonds der Chemischen Industrie (FCI) is gratefully acknowledged.

## 4.7 Supporting Information

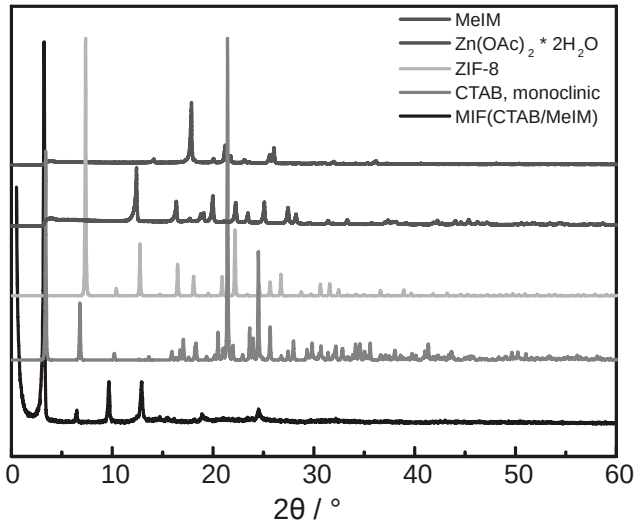


**Figure S1** XRD powder pattern of **MIF-1** (CTAB/MeIM), ZIF-8 and the starting materials $Zn(OAc)_2 \cdot 2H_2O$, MeIM and CTAB.

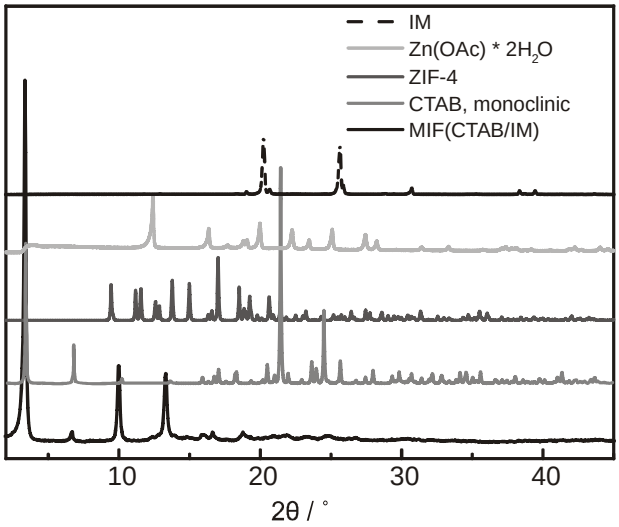


**Figure S2** XRD powder pattern of **MIF-2** (CTAB/IM) , ZIF-4 and the starting materials $Zn(OAc)_2 \cdot 2\ H_2O$, IM and CTAB.

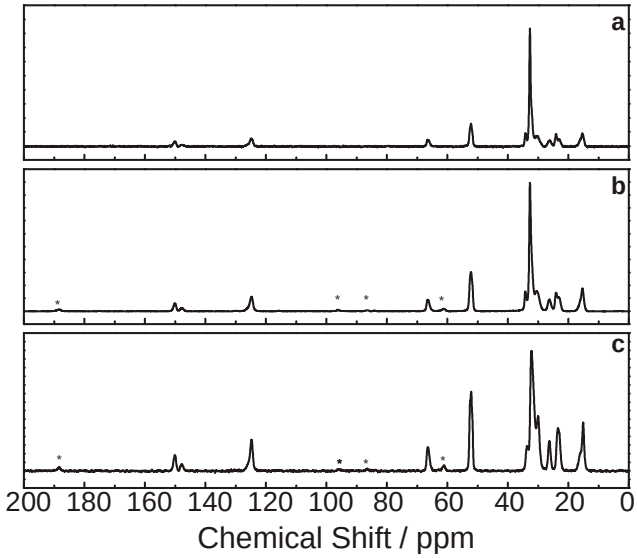


**Figure S3** $^{13}C$ solid-state NMR spectra obtained for **MIFs** based on surfactants with different chain lengths. a) TMODA($C_{21}H_{46}NBr$)/MeIM (**MIF-1B**), b) CTAB($C_{19}H_{42}NBr$)/MeIM (**MIF-1**), and c) TTAB ($C_{17}H_{38}NBr$)/MeIM (**MIF-1C**). Signals marked with an asterisk are spinning-side bands.

**Table S1** Experimental parameters for the solid-state $^{13}C$ and $^{15}N$ CP-MAS NMR measurements.

| **$^{13}C$** | Rotational frequency | Contact time [μsec] | reclay delay [sec] | scans |
|---|---|---|---|---|
| IM | 6 kHz | 5000 | 4096 | 16 |
| MeIM | 8 kHz | 2000 | 4 | 14268 |
| CTAB | 10 kHz | 5000 | 5 | 740 |
| CTAC | 6 kHz | 5000 | 5 | 379 |
| ZIF-8 | 8 kHz | 2000 | 4 | 15713 |
| ZIF-4 | 10 kHz | 5000 | 8 | 16 |
| **MIF-1** CTAB/MeIM | 8 kHz | 5000 | 5 | 10080 |
| **MIF-2**CTAB/IM | 8 kHz | 5000 | 5 | 220 |
| **MIF-3**CTAC/MeIM | 6 kHz | 5000 | 5 | 9393 |
| **MIF-1C** TTAB/MeIM | 8 kHz | 5000 | 5 | 1364 |
| **MIF-1B** TMODA/MeIM | 15 kHz | 5000 | 5 | 1254 |
| **MIF-1** CTAB/MeIM, 320°C | 8 kHz | 5000 | 5 | 10164 |
| **$^{15}N$** | | | | |
| **MIF-1**CTAB/MeIM | 6 kHz | 10000 | 4 | 15024 |
| ZIF-8 | 10 kHz | 10000 | 2 | 292 |
| CTAB | 6 kHz | 10000 | 4 | 16536 |

# 5 Ultrathin 2D Coordination Polymer Nanosheets by Surfactant-Mediated Synthesis

**This chapter is based on the article "Ultrathin 2D Coordination Polymer Nanosheets by Surfactant-Mediated Synthesis", published in *Journal of the American Chemical Society*, 2013, *135*, 6157–6164 by Sebastian C. Junggeburth, Leo Diehl, Stephan Werner, Viola Duppel, Wilfried Sigle and Bettina V. Lotsch.**

## 5.1 Abstract

Low-dimensional nanostructures offer a host of intriguing properties which are distinct from those of the bulk material owing to size-confinement effects and amplified surface areas. Here, we report on the scalable bottom-up synthesis of ultrathin coordination polymer nanosheets *via* surfactant-mediated synthesis and subsequent exfoliation. Layers of a 2D zinc coordination polymer are self-assembled in the interlamellar space of a reverse microemulsion mesophase into stacks of nanosheets interleaved with CTAB at regular intervals, thus giving rise to a lamellar hybrid mesostructure with a lattice period of ≈8 nm and an underlying highly crystalline substructure. The basic structural motif is composed of 2D acetato-benzimidazolato-zinc layers of tetrahedrally coordinated zinc joint together by anionic acetate and benzimidazolate ligands. The hierarchical structure was studied by PXRD, TEM, EDX, EELS, AFM and solid-state NMR spectroscopy, revealing a high level of order on both the atomic and mesoscale, suggesting fairly strong interactions along the organic-inorganic hybrid interface. Exfoliation of the hybrid material in organic solvents such as THF and chloroform yields sheet- and belt-like nanostructures with lateral sizes between tens and hundreds of nanometers and a height of about 10 nm measured by AFM, which precisely maps the basal

spacing of the lamellar mesostructure; further exfoliation results in nanobelts with minimum sizes around 4 nm. Finally, the sheet-like nanostructures behave as morphological chameleons, transforming into highly regular multiwalled coordination polymer nanotubes upon treatment with organic solvents.

## 5.2 Introduction

It is commonly accepted in nanoscience that the physical properties depend on the size of the nanomaterial.[209] Therefore, methods for controlling the size distribution of nanomaterials are key prerequisites to gain access to a plethora of interesting properties and size-dependent phenomena inherent to nanomaterials. While bottom-up synthesis methods are highly versatile and allow for a broad range of materials to be processed, they often give rise to products with a broad size distribution.[210] In contrast, physical top-down methods to nanomaterials such as electron beam or nanoimprint lithography offer a high level of size control and accordingly yield higher levels of monodispersity. However, the materials choice is limited for the latter and fabrication procedures are often elaborate and costly. Integrating bottom-up with top-down techniques within a *chemical* setting involving solution processing techniques is therefore highly desired. Exfoliation of layered bulk materials into their 2D constituents can be considered as such a “best of both worlds” approach, as it combines the versatility of “bottom-up” solid-state synthesis with the high precision formation of essentially monodisperse nanostructures by “top-down” delamination of pre-formed nanosheet building blocks. Nevertheless, control over the monodispersity is not always straightforward. Strong interlayer forces within the bulk material and insufficient control of the kinetics of exfoliation tend to break up the solid irregularly into nanosheets with different thicknesses and lateral dimensions. To alleviate such short-comings, the template-directed bottom-up – or direct – synthesis of 2D nanosheets has recently entered the stage as a powerful alternative to produce size-controlled na-

nosheets, which takes advantage of the lamellar mesophase of a surfactant acting as a template for the *in situ* generation of nanosheets.[211-219] Using this protocol, the layered assemblies can be broken up into individual nanosheets much easier, as the surfactant layers act as predetermined breaking points and stabilizing agents against re-agglomeration of the nanosheets at the same time. In addition, and as opposed to multi-step intercalation-exfoliation protocols, the direct synthesis of 2D nanomaterials involves a single step and hence can be carried out as one-pot reaction.

Layered materials carry a range of attractive anisotropic properties, including mechanical strength along two dimensions, size or shape-dependent electronic and optical properties, and high surface areas.[220] Processing schemes for layered materials are manifold and their susceptibility to soft chemistry protocols such as surfactant-assisted synthesis, intercalation, ion-exchange and exfoliation qualifies them for a number of applications ranging from catalysis,[221] adsorption,[222] chemical or biosensing[223] to solid-state nanoreactors,[224] anion/cation exchangers,[225] electrode materials,[226] and molecular sieves.[60] The large family of layered materials amenable to soft chemistry processing includes oxide and non-oxide species such as graphite, layered silicates,[227] titanates,[228] perovskites,[229] chalcogenides,[230-231] and layered double hydroxides (LDHs),[232-233] many of which have been exfoliated into individual nanosheets by exfoliation involving intercalation and ion-exchange of the pristine layered materials, or simply by mechanical or solvent-mediated exfoliation. Although bulk coordination (or "hybrid") polymers composed of metal ions and organic linkers joint *via* coordinative bonds, which have an inherent 2D structure are abundant, reports about their exfoliation into 2D nanostructures remain suspiciously scarce. The metal-organic framework MOF-2 and $[Cu_2Br(IN)_2]_n$ (IN =isonicotinato) are the first layered coordination frameworks that have been mechanically exfoliated down to the single sheet level,[234-235] while other groups used 1D and

2D nanomorphologies of Zn-BDC (BDC = 1,4-benzenedicarboxylate) as platforms for small molecule detection.[236-237] Cheetham and co-workers recently reported on the exfoliation-mediated synthesis of a range of highly crystalline, dense hybrid framework nanosheets based on dimethylsuccinic acid, which offer a host of interesting magnetic, electronic and mechanical properties, the latter studied by nanoindentation experiments.[238-244]

In this contribution, we present the direct surfactant-mediated bottom-up synthesis of 2D coordination polymer nanosheets as well as multiwalled nanotubes with a unique level of size control. In the present context, the term coordination polymer refers to a metal-organic substructure composed of metal centers (here $Zn^{2+}$) coordinated to organic linkers (here benzimidazole and acetate). Moreover, we demonstrate that exfoliation proceeds *via* a mesostructured hybrid phase featuring hierarchical order on the mesoscale as well as the atomic scale, mediated by *in situ* liquid-crystal templating during the formation of a highly crystalline, 2D layered acetato-benzimidazolato-zinc phase under reverse microemulsion conditions.

## 5.3 Results and Discussion

### 5.3.1 **Mesostructure Synthesis and Characterization**

As reported previously, the reaction of methylimidazole (MeIM) and imidazole (IM) with zinc acetate under reverse microemulsion conditions (cetyltrimethylammonium bromide (CTAB)/*n*-heptane/1-hexanol/water) leads to the formation of mesostructured imidazolate frameworks (**MIFs**) with a basal spacing of roughly 27 Å, composed of 1D zinc coordination polymers interleaved with CTAB.[166] Surprisingly, switching to benzimidazole (BeIM) as ligand gives rise to a mesostructured material with a dramatically enlarged lattice constant of ≈ 84 Å, dubbed **BeIM-MIF**. The observed basal spacing does not correspond to typical lamellar mesostructures containing single layer (26 Å) or bilayer (52 Å) arrangements of

CTAB.[166, 183-188] Besides a series of low angle reflections associated with the mesostructure, the XRD of the white product additionally shows a number of high angle reflections, indicative of a hierarchically structured material ordered both on the meso- and on the atomic scale (Fig.5.1, black line).

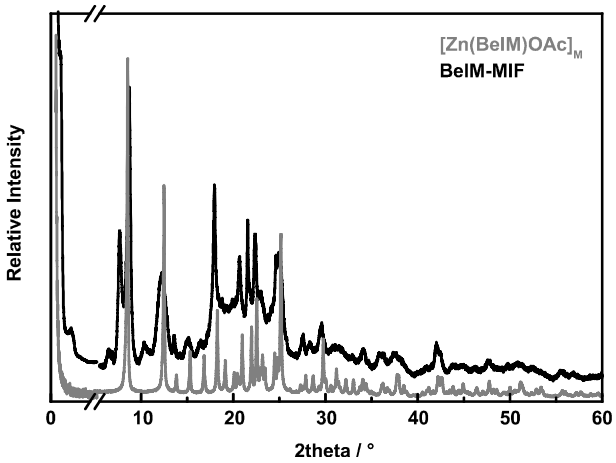


**Figure 5.1** XRD powder patterns of mesostructured **BeIM-MIF** and the underlying 2D layered coordination polymer **[Zn(BeIM)OAc]**. 00*l* reflections of the lamellar mesostructure are marked with an asterisk. The patterns at low angles (0.5 to 5°2θ) were measured in reflection mode, at high angles (5to 60° 2θ) in transmission mode.

Next, solid-state NMR and IR spectroscopy as well as mass spectrometry were used as local probes to elucidate the composition and bonding motifs in **BeIM-MIF**. The solid-state $^{13}C$ CP-MAS NMR spectrum of **BeIM-MIF** (Fig. 5.2, bottom) clearly indicates that both BeIM and CTAB are contained in the material; the presence of CTAB was also confirmed by mass spectroscopy ($C_{19}H_{42}N^+$peak at 284.6 *M*/*z*). On comparing the spectrum of **BeIM-MIF** with those of BeIM and CTAB, it is evident that the spectrum is not a mere overlay of the spectra of the starting materials. In **BeIM-MIF**, the $^{13}C$ positions next to N1/N3 (C8/C9 and C2) are shifted to lower field (139.5 ppm/140.3 ppm vs. 134.9 ppm (pristine BeIM) for C8/9 and 147.3 ppm vs. 141.7 ppm (pristine BeIM) for C2) and the remaining benzene signals (C4/7 at 114.7/113.6 ppm and C5/C6 at 121.5 ppm/120.4 ppm) are split. We therefore conclude that the chemical shifts and multiplett pattern of the$^{13}C$ signals are indicative of anionic [$BeIM^-$] as

found in ZIF-7 ($Zn(BeIM)_2$) (see Table 5.1), suggesting complete deprotonation of BeIM in contrast to proton bearing BeIM(H).[245] The shifting and splitting pattern of the CTAB $^{13}C$ signals ranging from 55.1 ppm to 14.3 ppm is similar to other mesostructured systems containing CTAB (Table 5.2).[166, 195] Notably, the $^{13}C$-MAS solid-state NMR shows two additional peaks at 182.9 and 19.3 ppm, which originate from acetate anions (OAc), and a minor peak at 178 ppm suggesting the presence of a small amount of protonated HOAc moieties. For comparison, HOAc (in $CDCl_3$) has signals at 178.4 and 20.0 ppm[164] and solid $Zn(OAc)_2 \cdot 2H_2O$ at 183.7 and 19.3 ppm (Table 5.1), respectively. Obviously, by using zinc acetate as starting material $OAc^-$is incorporated into the system. What is more, $OAc^-$ seems to play a crucial role for the formation of this compound as no precipitate was observed using alternative zinc sources such as $ZnCl_2$, $ZnBr_2$, $ZnI_2$, or $Zn(NO_3)_2$. While **MeIM-MIF** and IM-**MIF** are ternary systems Zn/(Me)IM/CTAB despite the presence of acetate ions in the microemulsion synthesis,[16613]$^{13}C$-NMR indicates that **BeIM-MIF** is in fact a quarternary system comprising Zn, BeIM, OAc, and CTAB.

**Table 5.1** Experimental and literature $^{13}C$ CP-MAS NMR chemical shifts (in ppm) of **BeIM-MIF**, **[Zn(BeIM)OAc]**, BeIM(H), ZIF-7, HOAc[164] and $Zn(OAc)_2 \cdot 2H_2O$, referenced to TMS.

| $^{13}C$ MAS NMR | $CH_3\delta CO_2$ | $\delta CH_3CO_2$ | $\delta$C2 | $\delta$C4,7 | $\delta$C5,6 | $\delta$C8,9 |
|---|---|---|---|---|---|---|
| **BeIM-MIF** | 182.9; 178.5 | 22.9 | 147.3;152.0 | 114.7;113.6 | 121.5;120.4 | 139.5; 140.3 |
| **[Zn(BeIM)OAc]** | 182.9 | 23.1 | 147.6 | 114.6;113.4 | 121.5; 120.4 | 140.3; 139.5 |
| ZIF-7 | | | 149.9 | 114.9 | 122.5;125.3 | 138.1;140.3 |
| BeIM(H) | | | 141.7 | 118.1;112.5 | 122.4;120.9 | 134.9 |
| HOAc[164] | 178.1 | 20.8 | | | | |
| $Zn(OAc)_2$ $2H_2O$ | 183.7 | 19.32 | | | | |

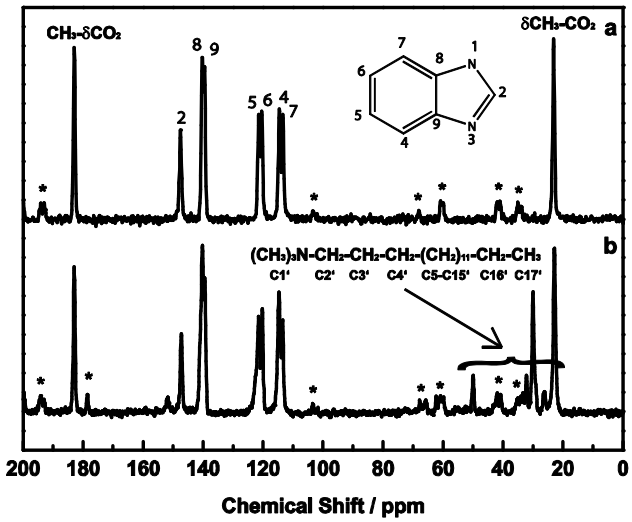


**Figure 5.2** $^{13}$C CP-MAS solid-state NMR spectra of A) **BeIM-MIF** and B) **[Zn(BeIM)OAc]**. Signals of the methylene chain partly overlap with the methyl group of acetate. Signals marked with an asterisk are spinning side bands.

**Table 5.2** Experimental $^{13}$C NMR chemical shifts (in ppm) and assignments pertaining to the surfactant moiety in **BeIM-MIF** and the surfactant CTAB, respectively.

| CTAB $^{13}$C NMR | CTAB[166] monoclinic | **BeIM-MIF** |
|---|---|---|
| C1’ | | 55.1 |
| C2’ | 62.5 | |
| C3’ | 29.1 | 26.2 |
| C4’ | 23.9 | [4] |
| C5’-C15’ | 31.2-34.1 | 29.99-32.3 |
| C16’ | 23.1 | * |
| C17’ | 16.1 | 14.4 |

[4]invisible due to overlap with the $CH_3$-group at 22.9 ppm of $Zn(OAc)_2$.

IR measurements are in agreement with the above findings (Fig. 5.3) and show the presence of small amounts of CTAB in **BeIM-MIF** through the two characteristic $\nu(CH_2)$-stretching vibrations at 2850 cm$^{-1}$and 2915 cm$^{-1}$.[166] Furthermore, characteristic BeIM and OAc ($\nu$(C=O)-stretching at 1542 cm$^{-1}$/1454 cm$^{-1}$) deformation and wagging modes are visible in the finger-print region. In line with the NMR measurements, the absence of broad $\nu$(OH) and $\nu$(NH)

stretching modes assignable to hydrogen-bonded proton bearing acetic acid and benzimidazole above 1800 $cm^{-1}$ points to fully deprotonated BeIM and OAc moieties.[164]

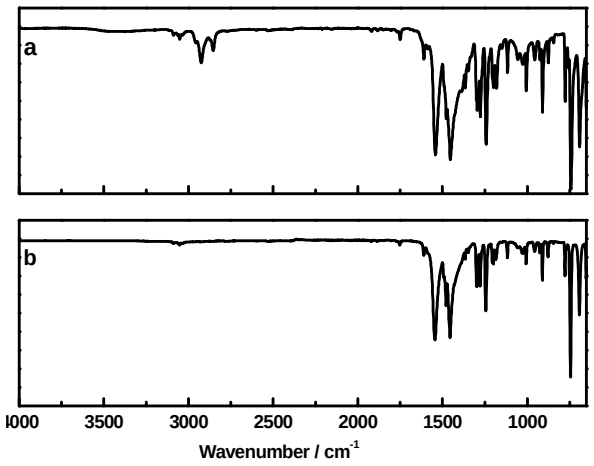


**Figure 5.3** IR spectra of a) **BeIM-MIF** and b) **[Zn(BeIM)OAc]**.

### *5.3.2* Basic Layered Structure

In order to shed light on the crystalline atomic-scale structure of the hybrid material as seen by high angle XRD we carried out the synthesis under the same reaction conditions as stated above, yet with a gradually decreasing amount of CTAB, starting from a 0.025 M solution (= 100%) of CTAB in a *n*-heptane/1-hexanol/water microemulsion. Incorporation of CTAB starts at a CTAB content of 40% (0.06 M) or higher, indicating the formation of micellarmesophases, which likely act as templates for the formation of the observed mesostructure. The XRD powder pattern of the product obtained without the addition of CTAB is depicted in Figure 5.1 (grey line). Clearly, the pattern no longer shows *00l*-reflections, indicating the absence of a mesostructure. The composition of the material was ascertained to correspond to the formula **[Zn(BeIM)OAc]** by elemental analysis (see Table 11). Strikingly, most of the high angle reflection positions and intensities are identical to those of **BeIM-MIF**, indicating the same underlying atomic ordering scheme in the mesostructured and the CTAB-free material. The close structural relationship between the two materials is confirmed by the $^{13}C$ sol-

id-state NMR measurements, which exhibit the same chemical shifts and splitting patterns of the anionic building blocks [BeIM$^-$] and [OAc$^-$], and, hence, similar chemical environments(Fig. 5.2). The XRD pattern of **[Zn(BeIM)OAc]** was indexed and refined by a Pawley Fit (*P*2$_1$/*c*, *a* = 10.814 Å, *b* = 9.833 Å, *c* = 8.813 Å, $\beta$ = 98.96° (Fig. 5.4)).

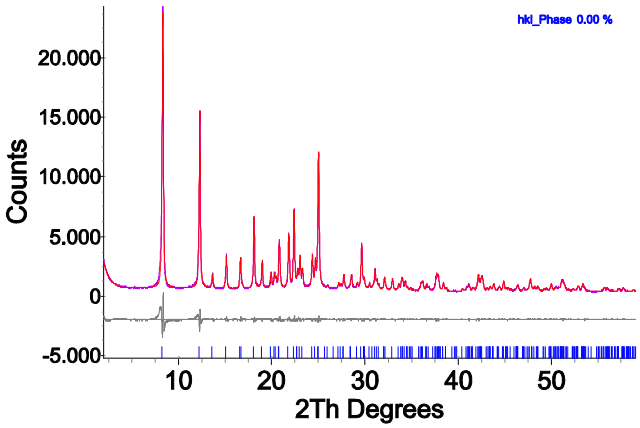


**Figure 5.4** Pawley fit of the XRD powder pattern of **[Zn(BeIM)OAc]**, yielding space group and lattice parameters *P*2$_1$/*c*, *a* = 10.814 Å, *b* = 9.833 Å, *c* = 8.813 Å, $\beta$ = 98.96°.

The metrics match well with that of a known poly[$\mu_2$-acetato-$\mu_2$-benzimidazolato-zinc(cobalt)(II)] coordination polymer with composition [M(BeIM)OAc] (M = Co$^{2+}$/Zn$^{2+}$),[246-247] consisting of M(BeIM)$_{2/2}$ chains running along *b* and M(OAc)$_{2/2}$ chains running along *c*, which are connected by tetrahedrally coordinated M$^{2+}$ions, forming a 2D non-interpenetrated network (Fig. 5.5a). In this layered hybrid framework, the 2D layers are oriented normal to the [100]-zone axis, connected by weak van der Waals interactions (Fig. 5.5b). We therefore infer that the basic atomic-scale structure of **BeIM-MIF** is composed of **[Zn(BeIM)OAc]** layers, which are interleaved periodically by CTAB through liquid-crystal templating during the synthesis under reverse microemulsion conditions (see below).

In line with these findings, elemental analysis (EA) of **BeIM-MIF** yields a [Zn$^{2+}$] : [BeIM$^-$] : [OAc$^-$] : [CTA$^+$Br$^-$] atomic ratio of roughly 7 : 7.5 : 6.5 : 1 (Table 5.3), while the composition of the CTAB-free material was determined as

$[Zn^{2+}] : [BeIM^{-}] : [OAc^{-}] = 1 : 1 : 1$ (Table 5.4). The fact that the ligand to metal ratio is essentially the same for both compounds ($\approx 1 : 1 : 1$) is consistent with the high tendency of high formation previously observed for hybrid compounds in the system Zn/(Be)IM/$RCO_2$.[199, 246, 248-249] The EA data of **BeIM-MIF** significantly differ from the **MIF-**systems Zn/MeIM/CTAB and Zn/IM/CTAB as the latter do not contain acetate ions, but have a much higher CTAB content.[166] Also, the elemental composition of **BeIM-MIF** is distinct from that of the 3D zeolitic imidazolate frameworks (ZIFs), which show ratios of $[Zn^{2+}] : [BeIM^{-}]$of1 : 2.[100]

**Table 5.3** Elemental analysis of **BeIM-MIF**, yielding an elemental composition of $\{[Zn_7(BeIM)_{7.5}(OAc)_{6.5}] \cdot CTAB\}$, corresponding to the formula $C_{84.5}H_{99}Br_1N_{16}O_{13}Zn_7$ with $M$ = 2084.37 g/mol.

| | **Zn** | **N** | **C** | **H** | **O** | **Br** |
|---|---|---|---|---|---|---|
| 1st sample | 22.35 | 10.85 | 48.37 | 4.66 | 9.56 | 4.21 |
| 2nd sample | 23.69 | 10.86 | 48.12 | 4.67 | 9.04 | 3.62 |
| 3rd sample | 21.65 | 10.44 | 49.31 | 5.09 | 9.87 | 3.64 |
| Average | 22.56 | 10.72 | 48.60 | 4.81 | 9.49 | 3.82 |
| calc. | 21.96 | 10.75 | 48.69 | 4.79 | 9.98 | 3.83 |

**Table 5.4** Elemental analysis of **[Zn(BeIM)OAc]** with elemental composition $C_9H_8O_2N_2Zn$ and $M$ = 241.55g $mol^{-1}$.

| | **Zn** | **N** | **C** | **H** | **O** |
|---|---|---|---|---|---|
| 1st sample | 26.79 | 11.65 | 44.63 | 3.27 | 13.21 |
| 2nd sample | 27.21 | 11.43 | 44.58 | 3.30 | 13.48 |
| 3rd sample | 27.49 | 11.38 | 44.54 | 3.27 | 13.32 |
| Average | 27.38 | 11.54 | 44.54 | 3.34 | 13.12 |
| calc. | 27.07 | 11.60 | 44.75 | 3.34 | 13.24 |

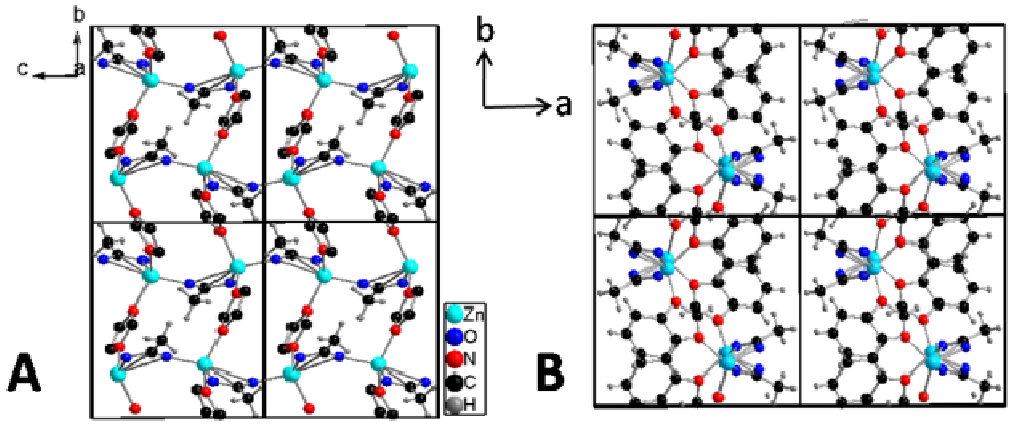


**Figure 5.5** A) Packing diagram of **[Zn(BeIM)OAc]** along the [100]-axis highlighting the 2D sheets formed by $Zn(BeIM)_{2/2}$ chains and $Zn(OAc)_{2/2}$ chains connected by $Zn^{2+}$ tetrahedra. The benzene rings of BeIM are omitted for clarity. B) View along [001] showing the weak van der Waals interactions between different sheets.[246]

### *5.3.3* Transmission Electron Microscopy

The above results suggest that layers of the coordination polymer **[Zn(BeIM)OAc]** constitute the basic structural units, while the presence of CTAB gives rise to a superstructure with nanoscale periodicity, which modulates the atomically ordered, layered arrangement of **[Zn(BeIM)OAc]** along the stacking direction. To probe the interrelation between atomic-scale and mesoscale structure in **BeIM-MIF** we carried out transmission electron microscopy (TEM) measurements along with EDX/EELS line scans and high angle annular dark field (HAADF)-STEM measurements. Measurements invariably reveal that the sample is extremely sensitive to the electron beam, thus requiring random selection of crystals and short acquisition times for the diffraction measurements, resulting in part in imperfect alignment of the sample with respect to the beam. TEM bright field measurements add evidence to the assumption of a lamellar mesostructure (Fig. 5.6a). Although the morphology of the material resembles that of closely stacked and slightly spliced rods at first sight, a tilt series enabling us to view the assembly at three different angles confirms the presence of thin slabs stacked on top

of each other (Fig. 5.6b-d). Notably, the slabs have a tendency to roll up at their edges, thus conveying the impression of a curled or rod-like morphology.

The morphology and elemental distribution within the mesostructure was analyzed by combined EDX/EELS line scans carried out on cross-section specimen of the material embedded in a polymer matrix (Fig. 5.7, resolution ~1 nm). The TEM cross-section image ascertains that the material is built up from lamellae featuring a periodic material contrast with a period of the dark and bright region of ≈ 8 nm. Notably, the elemental distribution profiles along the cross-section indicate a higher amount of Zn in the dark regions (bright regions in the HAADF image indicating elements with higher *Z*), while the carbon content peaks in the smaller, bright regions (dark regions in the HAADF image indicating elements with smaller *Z*). A slightly higher nitrogen content in the dark regions may be inferred from the nitrogen distribution (Fig. 5.7), thus suggesting that zinc and the nitrogen containing ligand BeIM reside in the larger slabs, whereas the surfactant acts as a spacer. Hence, the Zn containing dark slabs are composed of **[Zn(BeIM)OAc]** layers stacked along the [001] zone axis of the hybrid mesostructure, which are interleaved at regular intervals with a layer of CTAB, thus breaking up periodically the stacking of the **[Zn(BeIM)OAc]** layers of the pristine 2D structure as outlined in Scheme 5.1. This hypothesis is confirmed by selected area electron diffraction (SAED) patterns collected along [001] of the mesostructure, giving rise to diffraction patterns of the (*hk*0) planes of the stacked lamellae. Indeed, simulations of the corresponding in plane SAED patterns for pristine **[Zn(BeIM)OAc]** (along [100] in the CTAB-free structure)compare well with those observed experimentally for the mesostructured material, thus confirming the atomic level ordered structure of the lamellae, consistent with the composition and structure of **[Zn(BeIM)OAc]** (Fig. 5.8).

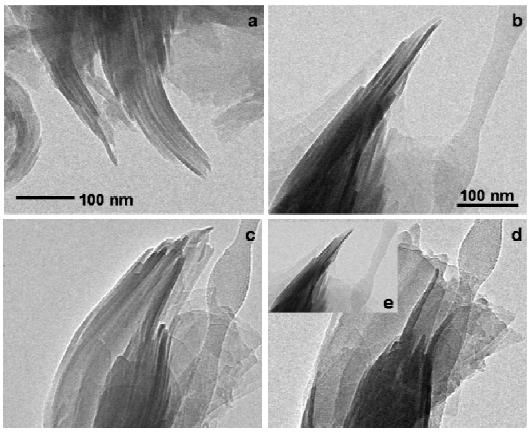


**Figure 5.6** a) Side view onto the lamellae and TEM tilt series (b-e) of **BeIM-MIF** showing the lamellar mesostructure. The images were obtained by rotating the TEM holder starting from b) -25°, to c) 0°, to d) +25°, and e) back to -25° (inset).

Evidence of the mesostructure is obtained by SAED patterns taken parallel to the lamellae along [010] to probe the stacking period and shed light on the mutual arrangement of the Zn-hybrid layers and CTAB, respectively (Fig. 5.9). The SAED pattern can be indexed on a series of *00l* reflections, corresponding to a lattice spacing of approx. 80 ±5 Å, which is consistent with the mesostructure seen by XRD (Fig. 5.1). The modulated intensity distribution with strong 007 and weaker 006 and 008 reflections suggests the presence of a superstructure arising from a more subtle scattering contrast along the stacking direction.

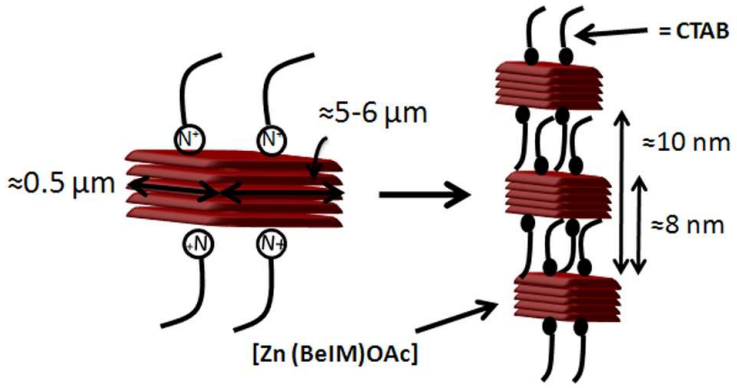


**Scheme 5.1** Schematic illustration of the composite mesostructure of **BeIM-MIF**, composed of layers of **[Zn(BeIM)OAc]** (in red) stacked along [001], and separated at regular intervals by CTAB (black). Typical lateral dimensions of the anisotropic sheets are shown on the left; the basal spacing of ~ 8 nm (10 nm for a stack covered by CTAB at the top and bottom) is indicated on the right.

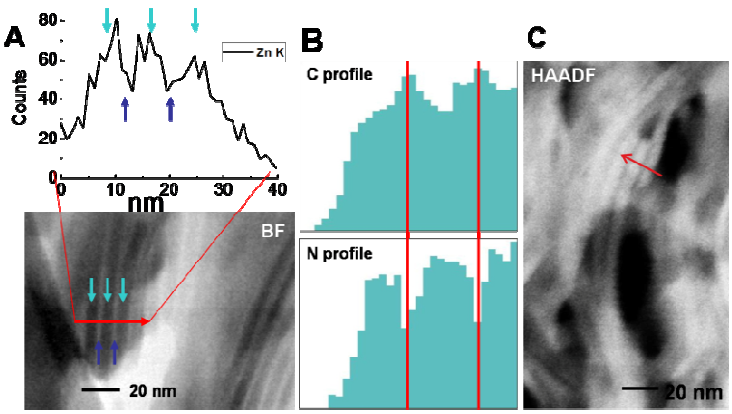


**Figure 5.7** A) EDX line scan of the Zn K-line intensity across **BeIM-MIF** layers in a polymer matrix, B) EELS line scan across an HAADF image (C) of **BeIM-MIF**. The elemental distribution of Zn, N and C was measured across several light and dark lamellae (spatial resolution ≈ 1 nm).

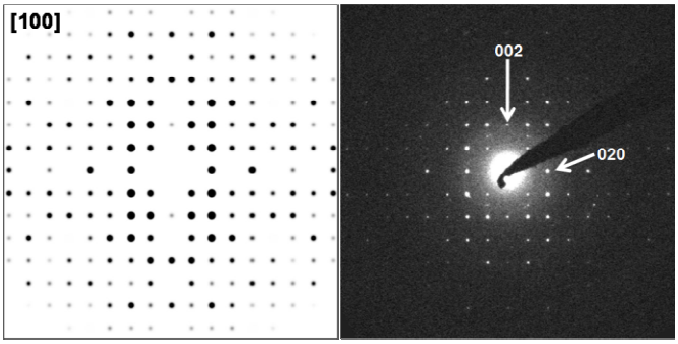


**Figure 5.8** SAED pattern (right) of **BeIM-MIF** sonicated for 5 min in $CHCl_3$, and simulation of the (*0kl*) plane (left) using the structure model of **[Zn(BeIM)OAc]**.

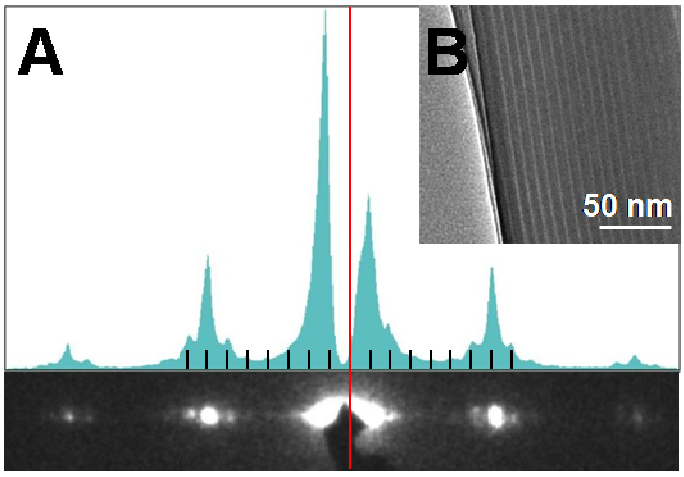


**Figure 5.9** A) SAED pattern and profile of **BeIM-MIF** viewed along [010] perpendicular to the corresponding lamellae (B) with a *d*-value of≈ 82 Å.

We associate the intensity modulation with the superposition of the layer stacking periodicity in the **[Zn(BeIM)OAc]** substructure (~ 1.1 nm) with the mesostructure period of ~ 8 nm, which results from the ordered insertion of CTAB between the layers at regular intervals after roughly five to six layers of **[Zn(BeIM)OAc]**. In other words, the systematic disruption of the layer stacking sequence of the 2D layered coordination polymer by CTAB insertion gives rise to a regular mesostructure, where the modulated intensity distribution is reminiscent of the layer stacking period in the pristine acetato-benzimidazolato-zinc substructure.[250]

### 5.3.4 **Surfactant Extraction**

To confirm the above model and to examine the strength of interaction between the surfactant and hybrid layers within this stacked arrangement we carried out surfactant extraction experiments aiming at the complete removal of CTAB from the mesostructure, which should result in pure **[Zn(BeIM)OAc]**. Remarkably, the surfactant could only be removed by refluxing the material in EtOH or $CHCl_3$ for many hours, which was verified by $^{13}C$ solid-state NMR by monitoring the intensity of a characteristic CTAB signal at 55.1 ppm (representing the $-N(CH_3)_3^+$-group of CTAB) relative to the acetate peak of the hybrid layers at 182.9 ppm for increasing reflux times (Fig. 5.10/5.11).

As outlined in Fig. 5.12, CTAB is gradually released during the course of several hours under reflux in EtOH, and is completely removed after 48 h, which is confirmed also by the XRD patterns of the extracted sample (Fig. 5.13 and Table 5.5). On the one hand, this again highlights the close relationship between **[Zn(BeIM)OAc]**and **BeIM-MIF**, as the latter is neatly transferrable into the former by surfactant extraction. On the other hand, the harsh conditions necessary to fully remove the surfactants indicate that strong interactions between the surfactants and the **[Zn(BeIM)OAc]** layers exist, which may even be an indication of grafting of the

surfactants into the zinc-hybrid layers by direct bonding of $Br^-$ to the neighboring **[Zn(BeIM)OAc]** layer, while $CTA^+$ is electrostatically attached to the layers *via* $CTA^+$ - $Br^-$ interactions.

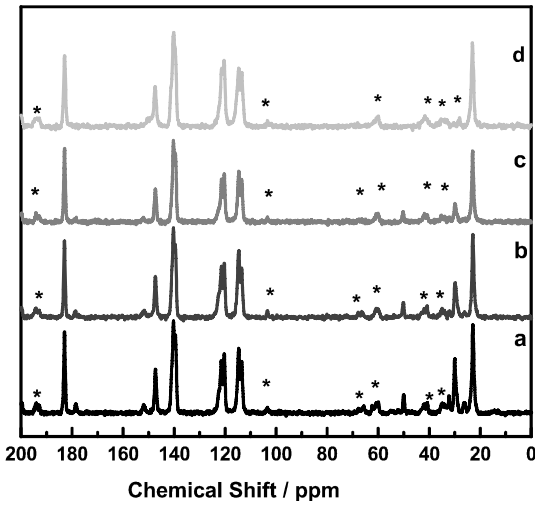


**Figure 5.10** Solid-state $^{13}C$ CP-MAS NMR spectra of a) **BeIM-MIF** and **BeIM-MIF** refluxed in ethanol for b) 16 h, c) 32 h and d) 48 h. Signals marked with an asterisk are spinning side bands.

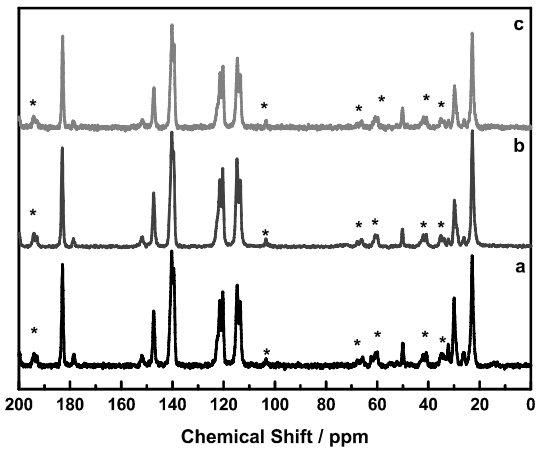


**Figure 5.11** $^{13}C$ MAS solid-state NMR spectra of a) **BeIM-MIF** and **BeIM-MIF** after refluxing in chloroform for b) 16 h and c) 32 h. Free CTAB can easily be dissolved in chloroform. Signals marked with an asterisk are spinning side bands.

The $^{15}$N CP-MAS NMR spectra of **[Zn(BeIM)OAc]** and **BeIM-MIF** (Fig. 5.14, Table 5.6) are largely in line with this hypothesis. The signal around -194.3 ppm can be assigned to the deprotonated nitrogen atoms N1/N3 of BeIM (-194.4 ppm for BeIM in **[Zn(BeIM)OAc]**, -192.4 ppm for ZIF-7, while proton-bearing BeIM(H) has two signals at 145.2 and 223.5 ppm for N1/N3, respectively). The minor signal at -187.2 ppm may evidence a slight charge redistribution at the BeIM nitrogen sites in the outer **[Zn(BeIM)OAc]**-layers, which are in direct contact with CTAB, due to an increased Zn coordination sphere. However, the presence of impurity phases giving rise to this signal cannot be excluded. The quaternary nitrogen of CTAB is not visible in the $^{15}$N NMR spectra, which may in part be due to the low concentration of CTAB compared to the hybrid layers, but may also point to a significantly decreased mobility of the surfactant through grafting to the Zn-containing layers.

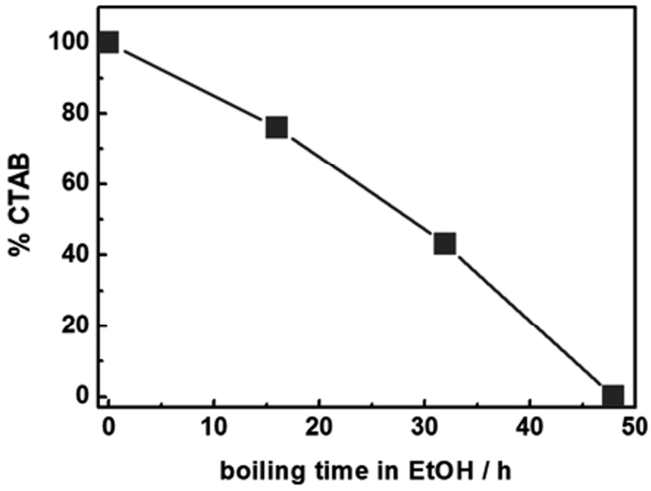


**Figure 5.12** Time evolution of the extraction of CTAB from mesostructured **BeIM-MIF**. The CTAB content of the mesostructure is extracted from solid-state NMR measurements and plotted for increasing reflux times.

**Table 5.5** Elemental analysis of **BeIM-MIF**, refluxed for 32 h in EtOH. The resulting elemental composition is about the same as for **[Zn(BeIM)OAc]** with $M[Zn(CH_3CO_2)C_7H_5N_2]$ = 241.55 g $mol^{-1}$).

| | **Zn** | **N** | **C** | **H** | **Br** | **O** |
|---|---|---|---|---|---|---|
| 1st sample | 25.19 | 11.65 | 45.99 | 3.83 | 0 | 11.11 |
| 2nd sample | 25.83 | 11.50 | 46.39 | 3.98 | 0 | 10.37 |
| average | 25.51 | 11.58 | 46.19 | 3.91 | | 10.74 |
| calc. | 27.08 | 11.60 | 44.75 | 3.34 | | 13.25 |

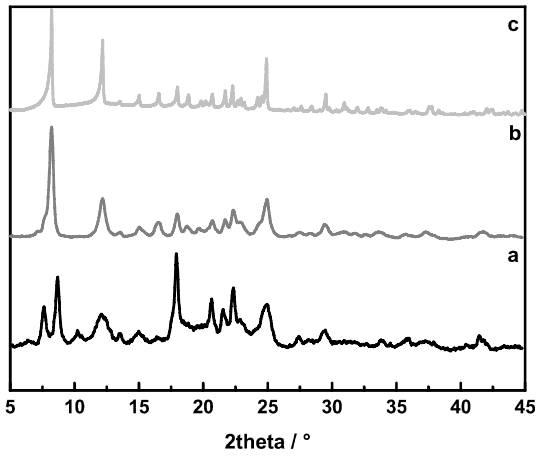


**Figure 5.13** XRD powder patterns of a) **BeIM-MIF**, b) **BeIM-MIF** refluxed for 48 h in EtOH and c) **[Zn(BeIM)OAc]**.

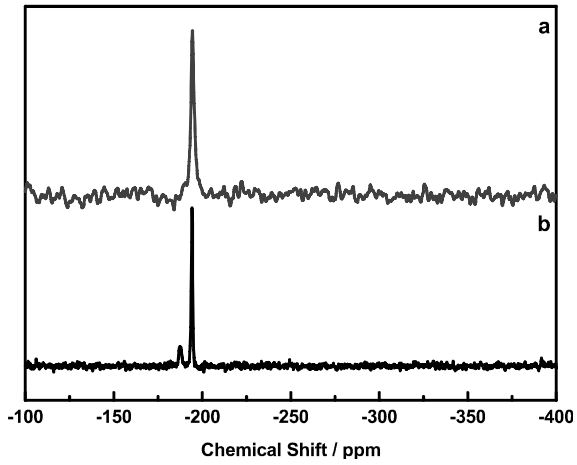


**Figure 5.14** Solid-state $^{15}N$ CP-MAS NMR spectra of a) **[Zn(BeIM)OAc]** and b) **BeIM-MIF**.

**Table 5.6** Experimental $^{15}N$ NMR chemical shifts (in ppm) of **BeIM-MIF**, **[Zn(BeIM)OAc]**, BeIM(H), and ZIF-7, referenced to nitromethane.

| $^{15}N$ NMR / ppm | δN |
|---|---|
| **BeIM-MIF** | 194.3; 187.2 |
| **[Zn(BeIM)OAc]** | 194.4 |
| BeIM(H) | 145.2; 223.5 |
| ZIF-7 | 192.4 |

### 5.3.5 **Exfoliation**

The lamellar morphology of the mesostructure with its rolled up edges together with the structure model outlined above suggests that the lamellae are held together only weakly by van der Waals interactions between the hybrid material and the CTAB layers. Therefore, exfoliation of the multilayer stacks or even individual **[Zn(BeIM)OAc]** layers should be feasible by employing mechanical and solvent-assisted exfoliation protocols. To probe this hypothesis, exfoliation experiments of **BeIM-MIF** were carried out using different solvents, including ethanol (EtOH), dimethylformamide (DMF), water, chloroform ($CHCl_3$), toluene (Tol), tetrahydrofurane (THF). The samples were shaken for 72 h until a milky colloidal suspension was obtained. The exfoliation efficiency decreases in the following order: THF > Tol > $CHCl_3$. Exfoliation in strongly polar solvents (i.e. water and DMF) was unsuccessful, as the solvent molecules apparently cannot efficiently penetrate between the hydrophobic interlayer space flanked by nonpolar benzene and methylgroups, and filled by CTAB. The colloidal character of the suspensions obtained by exfoliation in THF, Tol, and $CHCl_3$ is evidenced by the Tyndall effect upon irradiation with a laser beam, with the finely dispersed nanosheets being the reason for scattering of the incident laser light (Fig. 5.15).

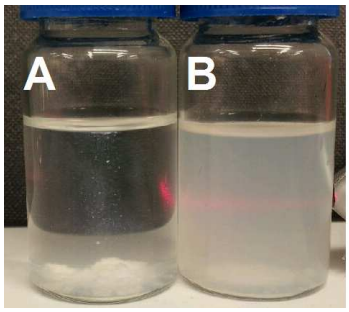


**Figure 5.15** Demonstration of the Tyndall effect of a suspension of **BeIM-MIF** in Toluene. While the red laser beam is invisible in the supernatant in (A) before exfoliation of **BeIM-MIF**, it is scattered by the colloidal suspension (B) containing **BeIM-MIF** nanosheets.

The colloidal suspensions were subsequently spin-coated on Si-wafers (~ 1.5 x 1.5 $cm^2$) for characterization by atomic force microscopy (AFM). Figure 5.16 shows typical AFM images of the morphology of **BeIM-MIF** after shaking in Tol and THF and subsequent spin-coating. The deposited particles display anisotropic lateral dimensions up to ~0.5 μm x ~5 - 6 μm (for Tol) with a belt-like morphology and a rhomboedral surface area of up 1.5 μm x 1.5μm (for THF), respectively. Mainly anisotropic nanobelts were observed by AFM after exfoliation in Tol and THF, rather than sheets with equidistant lateral dimensions as seen *via* TEM on imaging the powdered sample without previous solution treatment. We attribute this fact to the mechanical disruption of the sheets during the sonication/shaking process, which reduces their lateral size and gives rise to the observed ribbon-shaped morphology. Notably, the measured heights for the deposited nanostructures are very uniform and amount to roughly 10.2 nm, which is consistent with the thickness of one dark and two bright lamellae, as determined by EDX/EELS measurement (Figs. 5.7A and 5.7B).

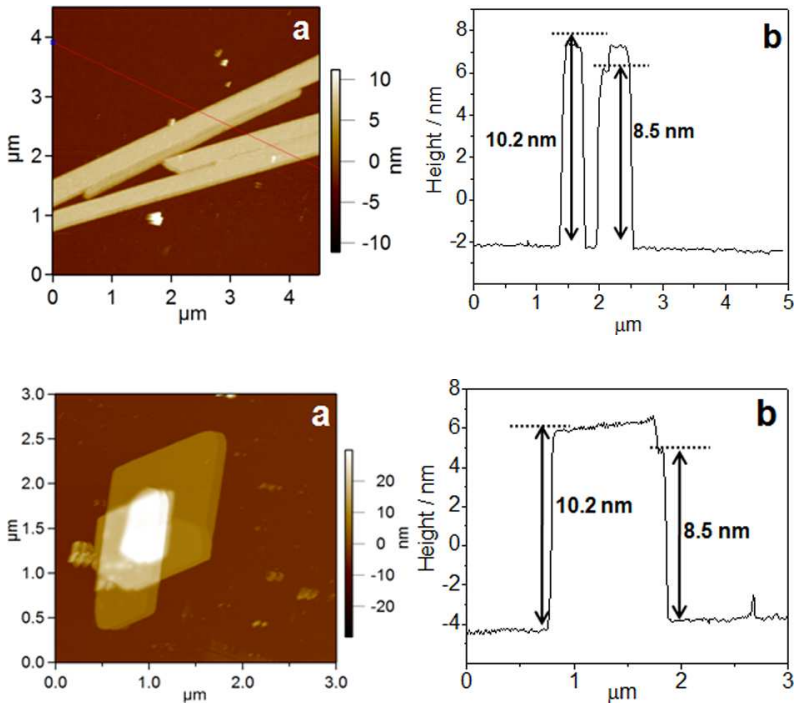


**Figure 5.16** AFM surface topographies of **BeIM-MIF** exfoliated in different solvents. Top row: nanosheets exfoliated in Tol: a) AFM image showing strongly anisotropic nanosheets (i.e. nanobelts/nanoribbons), b) height profile; bottom row: nanosheets exfoliated in THF: a) AFM image, b) height profile.

Similarly, we observe a surface step of around 2 nm at the top of most nanobelts, which we tentatively attribute to a layer of CTAB as well as water covering the belts at the top and likely also at the bottom. To test whether the nanobelts can further be delaminated into smaller stacks of **[Zn(BeIM)OAc]** layers, the wafers showing ribbon-like nanostructures were immersed in an EtOH solution for 5 h. The resulting AFM images are shown in Figure 5.18.

While the shape and lateral size of the nanostructures remains largely unchanged, the surface of **BeIM-MIF** roughens during the washing process. The measured heights after the washing step range from 4 – 7 nm, indicating that the nanobelts can in fact be reduced in height even further by ablating single **[Zn(BeIM)OAc]** layers from the top of the ribbon.

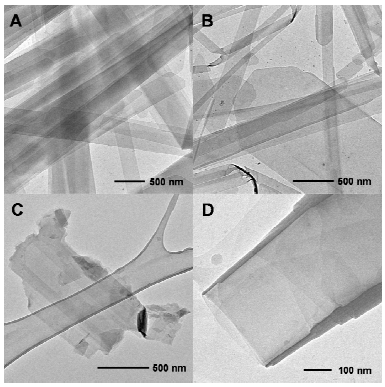


**Figure 5.17** TEM images of **BeIM-MIF** exfoliated in THF. The material exhibits various nanomorphologies, including nanobelts (A), sheets and intergrown belts (B+C), as well as multiwalled nanotubes (D).

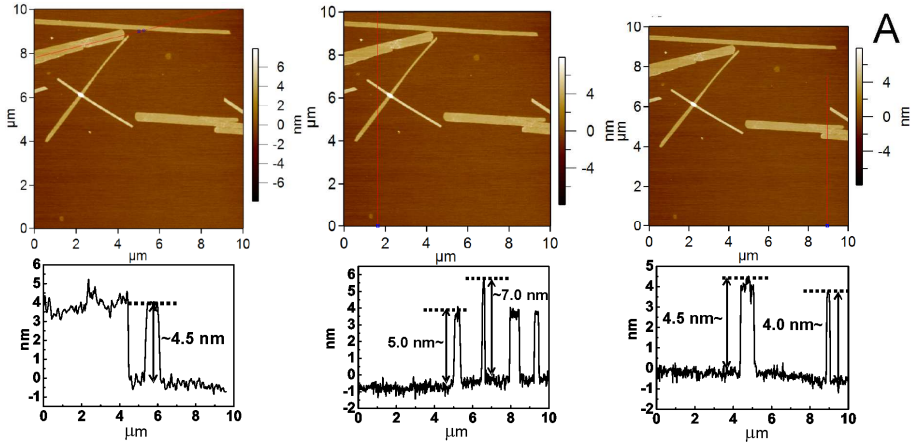


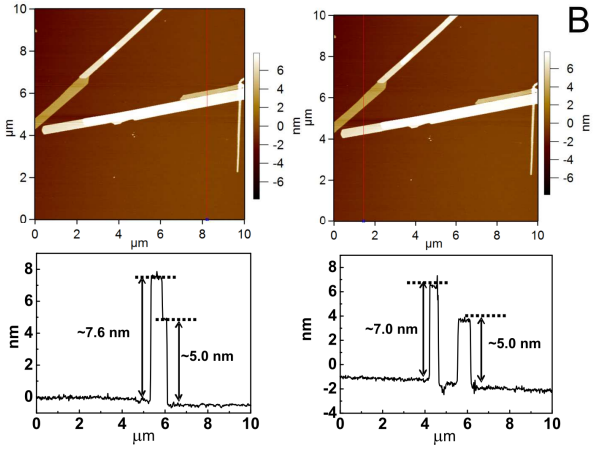


**Figure 5.18** AFM images of **BeIM-MIF** after shaking in Tol and spin-coating (shown in Fig. 5.16), and subsequent immersion of the Si-Wafer in an EtOH solution for 5 h. The two different displays (A and B) show imaging and the corresponding height profiles along three (A) or two (B) different lines (shown in red).

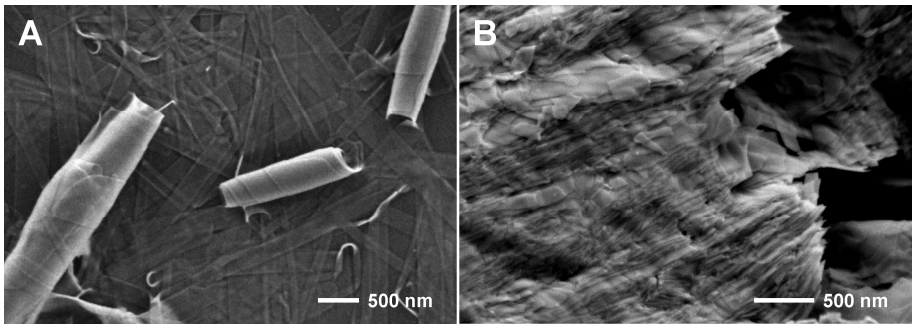


**Figure 5.19** SEM images of exfoliated **BeIM-MIF** (A), showing the formation of nanoscrolls next to nanobelts with varying lateral dimensions. (B) Non-exfoliated **BeIM-MIF**, revealing the regular stacking of tightly packed slabs.

### 5.3.6 Nanotube Formation

A peculiar feature observed *via* TEM is the formation of nanotubular structures apart from extended sheets or belts (Fig. 5.17D). SEM images reveal that these nanoscrolls are formed by self-rolling of one or more belts, similar to carbon nanoscrolls formed by rolling up of graphene (Fig. 5.19A).[251-252] The nanoscrolls share the same in-plane structure and layered mesostructure as the nanosheets and belts, from which they seem to roll up into open, tubular structures with diameters ranging between 400 and 600 nm. This is consistent with the previously observed tendency of the sheets to buckle at their edges. Interestingly, the underlying periodicity of the lamellar mesostructure in the tubes is larger than that observed for the sheet-like lamellar mesostructure and amounts to roughly 10 nm. Note that nanotube formation is not a quantitative process and is only observed for samples which have been shaken in an organic solvent for exfoliation. We therefore infer that nanoscrolling occurs *via* a solution-mediated process during which the CTAB layers are likely stripped off (Fig. 5.19B *vs*. 5.19A). Together with charge inhomogeneities and surface strain induced by a loss of CTAB, this may lead to a higher tendency for spiral wrapping of the sheets to reduce the surface free energy through increased van der Waals forces. The formation of coordination polymer nanotubes next to extended sheet-and belt-like structures highlights the potential of this bottom-up synthesis for

the creation of a diverse range of nanomorphologies, which can be tuned by varying the synthesis conditions.

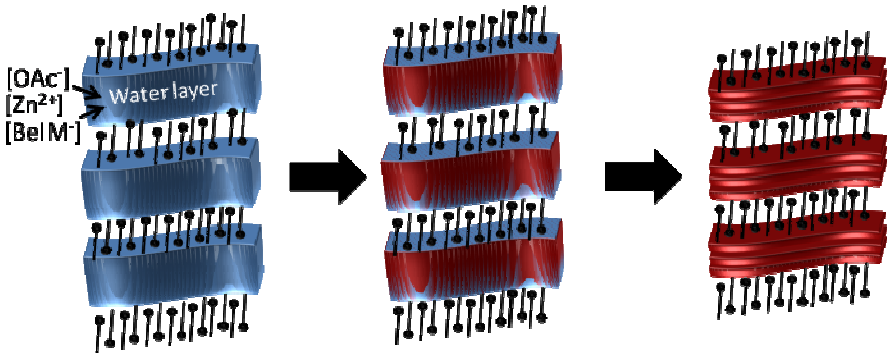


**Scheme 5.2** Schematic of the tentative formation mechanism of mesostructured **BeIM-MIF** by surfactant-mediated liquid crystal templating under reverse microemulsion conditions. CTAB forms a lamellar mesophase in the hydrophobic solvent, enclosing nanoscale water reservoirs (blue) as confined reaction space in which the coordination polymer nucleates. The consolidated structure (right) is composed of **[Zn(BeIM)OAc]** layers (red) interleaved with CTAB bilayers.

### 5.3.7 **Formation Mechanism**

The coordination polymer mesostructure was obtained under inverse microemulsion conditions in the presence of large amounts (>0.01 gew%) of CTAB, which points to the central role the surfactant plays in mesophase formation. The observed lamellar mesostructure featuring a precise pattern of hybrid inorganic slabs interleaved with organic slabs is in line with CTAB acting as a lamellar template, which is replicated by the spatially confined reaction of $Zn(OAc)_2$ and BeIM in the interlamellar space of the surfactant mesophase. The tentative formation mechanism is outlined in Scheme 2, highlighting the action of the CTAB mesophase as confining template, which directs the gradual formation of the layered Zn-hybrid phase within the water reservoirs sandwiched between the organic liquid crystal phase. This mechanism is in line with the observed hierarchical structure, which forms as a consequence of both geometric confinement and interfacial free energy minimization at the organic-hybrid interface.

## 5.4 Conclusion

In summary, we have demonstrated the formation of a hierarchical coordination polymer mesostructure, which is obtained under reverse microemulsion conditions by surfactant mesophase templating. The lamellar mesostructure with a periodicity of 8 nm results from incorporation of CTAB into a crystalline layered **[Zn(BeIM)OAc]** structure at regular intervals, thus giving rise to stacks of nanosheets with a precisely defined number of layers, each stack being separated by CTAB. As opposed to the bonding situation in the mesostructured imidazolate frameworks reported previously **(MIF-1** and **MIF-2**), the presence of acetate ions in **BeIM-MIF** apparently enables the formation of robust 2D nanosheets, which form the underlying building blocks of the mesostructure reported in this work, thus giving rise to a material which is ordered on both the atomic scale and mesoscale. The stacks of nanosheets can be isolated by ultrasonic treatment, featuring a uniform size distribution of around 10 nm as determined by AFM under ambient conditions. Notably, we observe the formation of multi-walled nanotubular structures by rolling up of the 2D slabs owing to their highly flexible morphology, a phenomenon which has rarely been observed to date in the context of crystalline 2D coordination polymers.[216]

## 5.5 Experimental Section

Cetyltrimethylammonium bromide (CTAB, $C_{19}H_{42}NBr$, Fluka 98%), benzimidazole (Fluka, 99%), 1-hexanol (Aldrich, 98%), *n*-heptane (99%), chloroform (Merck, p.a.), THF (Merck, p.a.), toluene (Merck, p.a.) and zinc acetate dihydrate ($Zn(OAc)_2 \cdot 2H_2O$, Merck, 99.5%) were purchased from commercial sources and used without further purification.

*Material Synthesis.* **BeIM-MIF** was synthesized in a typical procedure adding 5.4 mL BeIM (0.60 M in 1-hexanol) and 2.7 mL zinc acetate dihydrate (1.2 M in water) to a suspension

containing a mixture of 0.05 M CTAB/heptane/1-hexanol (200 mL). The established microemulsions were stirred vigorously for 10 min at room temperature and refluxed at 100 °C for 16 h. A white precipitate can be observed after 5 min of stirring. The white powder was isolated by centrifugation at 13,000 rpm for 10 min and washed with cold ethanol. The bulk material **[Zn(BeIM)OAc]** was synthesized like **BeIM-MIF** but without adding the surfactant. The latter reaction works also by mixing BeIM and Zinc acetate dihydrate in a ratio of 1:1 in either chloroform or ethanol.

*Instrumental.* Powder X-ray diffraction (XRD) data were collected on a D8 diffractometer (Bruker) and Stadi P powder diffractometer (Stoe), both using Cu-$K_{\alpha 1}$ radiation. For transmission electron microscopy (TEM), samples were prepared by drop coating the solutions on Cu grids with lacey carbon backing (Plano GmbH). TEM experiments were performed on a Philips CM 30 ST microscope equipped with a $LaB_6$ thermal source operated at 300 kV. SAED simulations were carried out with the software EMAP. EDX linescans and EELS measurements were performed with a VG HB 501UX microscope. For cross-section experiments the sample was embedded in Epo Fix resin, trimmed (Leica EM Trim 2) and cut with an ultramicrotome (Leica EM UC6). The resulting sample thickness was ~ 50 nm.

$^{13}C$ and $^{15}N$ solid-state cross polarization magic angle spinning nuclear magnetic resonance (CP-MAS NMR) spectra were recorded at room temperature with a DSX Avance 500 FT spectrometer (Bruker) equipped with a commercial 4 mm MAS NMR double-resonance probe at a magnetic field of 11.7 T. For the chemical shifts the samples were referenced with to TMS ($^{13}C$) and nitromethane ($^{15}N$) as external standards. The zinc content was determined by inductive coupled plasma atomic emission spectrscopy (ICP-AES) using a VISTA-PRO simultan spectrometer (Varian). Determination of the elements H, C, N, Cl and Br was carried out by oxidative pulping using a commercial elemental analyzer system with helium as carrier

gas (VARIO EL, Elementar Analysensysteme GmbH). The different NMR parameters for the single measurements are summarized in Table S2 (Supporting Information). Atomic Force Microscopy (AFM) measurements were carried out in tapping-mode on an Asylum MFP-3D AFM (Asylum Research, Santa Barbara) with an Olympus Si Micro Cantilever (300 kHz resonant frequency, 26.1 N/M spring constant).

## 5.6 Acknowledgement

We thank C. Minke and Dr. J. Weber for solid-state NMR measurements, H. Hartl and M.-L. Schreiber for ICP-measurements and Dr. M. Konuma for XPS-measurements. We are indebted to C. Donadel for practical support. We thank B. Bußmann for TEM cross-section preparation.

## 5.7 Supporting Information

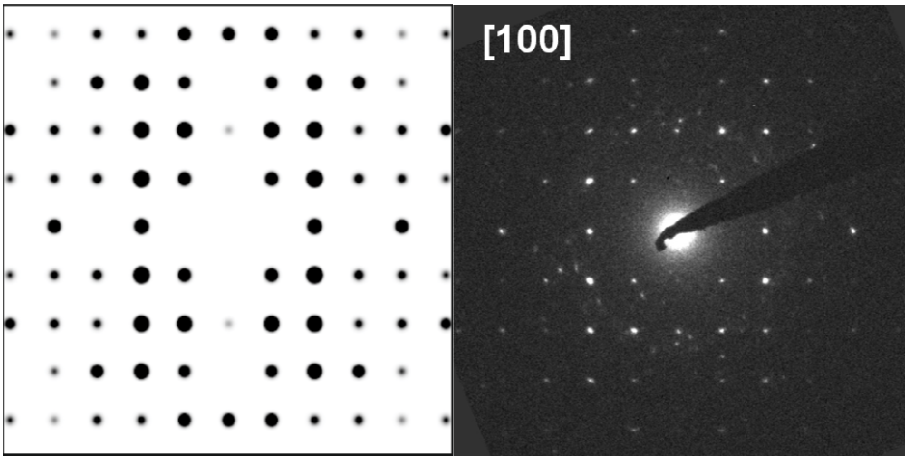


**Figure S4** SAED images of the (*hk*0) plane of **BeIM-MIF** after refluxing in ethanol for 32 h (right).The SAED patterns are consistent with the simulation for **[Zn(BeIM)OAc]**.

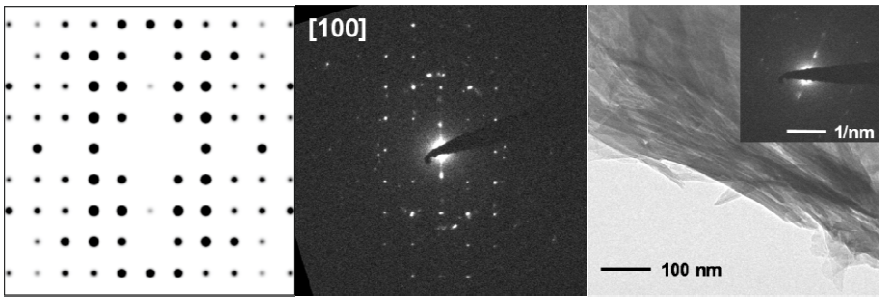


**Figure S5** SAED patterns (left: simulation, middle: experiment) and TEM image (right) of **BeIM-MIF** after refluxing in chloroform for 32 h.

**Table S2** Experimental parameters for the $^{13}C$ and $^{15}N$ solid-state NMR measurements.

| **$^{13}C$** | Rotational frequency | Contact time [μsec] | recycle delay [sec] | scans |
|---|---|---|---|---|
| BeIM(H) | 10 | 1000 | 24 | 1024 |
| ZIF-7 | 15 | 5000 | 4 | 15713 |
| **BeIM-MIF** | 10 | 5000 | 2 | 512 |
| **BeIM-MIF** (16 h,EtOH) | 10 | 5000 | 1 | 512 |
| **BeIM-MIF**(32 h,EtOH) | 10 | 5000 | 1 | 512 |
| **BeIM-MIF**(48 h,EtOH) | 10 | 5000 | 1 | 512 |
| **[Zn(BeIM)OAc]** | 10 | 5000 | 64 | 48 |
| **$^{15}N$** | | | | |
| **BeIM-MIF** | 10 | 5000 | 2 | 10100 |
| ZIF-7 | 10 | 10000 | 1 | 35264 |
| **[Zn(BeIM)OAc]** | 10 | 5000 | 32 | 1520 |
| BeIM(H) | 10 | 10000 | 4 | 1680 |

# 6 Toward BeIM-MIFs based on carboxylic acids with extended alkyl chains

This chapter is a continuation of the previous one in that in the following sections carbonic acids with extended alkyl chains such as propanoic (ProH, $CH_3CH_2CO_2H$) and butyric (ButoH, $CH_3CH_2CH_2CO_2H$) acids will be used instead of acetic acid, which was used as a structural building block in chapter 5. It is known from the structural model of **[Zn(BeIM)OAc]** shown in Figure 5.5 that the methylgroups of acetate are oriented along the *a*-axis of the unit cell. Therefore, for the substituted structures of **[Zn(BeIM)R]** (R = Pro and Buto) an increased *a*-axis is expected, while the other structural parameters should be largely unaffected.

## 6.1 Propanoic acid (Pro)

### 6.1.1 X-Ray Powder Diffraction and TEM measurements

The same conditions as in the system Zn/BeIM/OAc were applied, except that $Zn(OAc)_2$was mixed with BeIM(H) and zinc propionate ($Zn(Pro)_2$) instead of the corresponding acetate salt in a ratio of 1 : 1. The reaction was either carried out under microemulsion conditions with CTAB/1-hexanol/*n*-heptane, or under the same conditions without using the surfactant. The XRD powder patterns of the isolated products in the ternary system Zn/BeIM/Pro, named **[Zn(BeIM)Pro]**, and in the quaternary system CTAB/Zn/BeIM/Pro, named **BeIM-MIF(Pro)**, respectively, are depicted in Figure 6.1. All XRD powder patterns show no residues of the starting materials and do not correspond to known ZIF-structures (e.g. $Zn(BeIM)_2$, named ZIF-7 or ZIF-11).[100] Indexing and a Pawley Fit of the powder pattern of **[Zn(BeIM)Pro]** was possible (Figure 6.2) and revealed the lattice parameters $P2_1/c$; $a$ = 11.69 Å, $b$ = 9.92 Å, $c$ = 8.77 Å, $\beta$ = 92.36°.

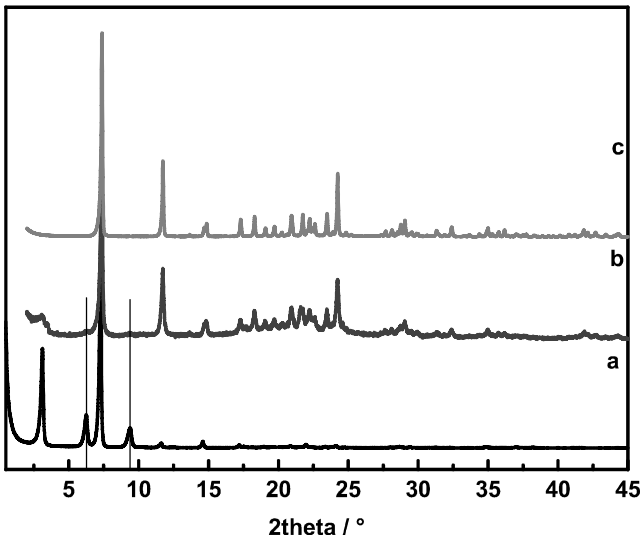


**Figure 6.1** XRD powder patterns of a) **BeIM-MIF(Pro)** measured on a D8 Bruker Advance in reflection mode and b) **BeIM-MIF(Pro)** and c) **[Zn(BeIM)Pro]** both measured in a capillary in transmission mode. The rise in intensity at $2\theta \approx 2°$ is due to the primary beam. The two reflections in the reflection measurement marked with a line are also visible in transmission mode but with significantly lower intensity. The comparison of a) and b) gives an impression of preferred orientation in reflection mode, possibly due to the glass slides.

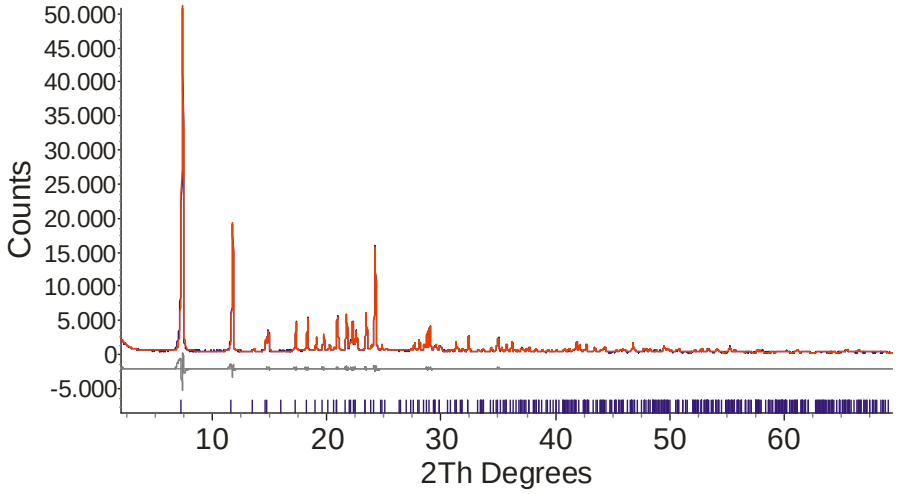


**Figure 6.2** Pawley Fit on powder XRD data of **[Zn(BeIM)Pro]** yielding space group and lattice parameters $P2_1/c$; $a$ = 11.69 Å, $b$ = 9.92 Å, $c$ = 8.77 Å, $\beta$ = 92.36°, GoF = 2.315.

The phase is isotypic with **[Zn(BeIM)OAc]**.[246] As already known from the acetate system a relationship between the layered coordination polymer **[Zn(BeIM)Pro]** and the mesostructure

**BeIM-MIF(Pro)** is observable. All wide angle reflection positions of the ternary system can also be assigned in the quaternary mesostructured system. The mesostructure exhibits additional reflections at *2θ* values of 6.2°, 9.2° and at small angles at 3.1° *2θ* (corresponding to a *d* value of 28.7 Å), which was verified by an X-ray measurement at small angles (Figure 6.1a). In contrast to **BeIM-MIF** (reflection at *d* ~80 Å) no further reflections at smaller angles were observed. The measurement in Bragg Brentano geometry also demonstrated the highly preferred orientation of the material, which is visible by measuring the sample on glass slides in reflection mode in contrast to a rotating capillary in transmission mode. While all reflections are having the same positions (compared to transmission mode measurements), reflections at high *2θ* values show a much lower intensity compared to reflections at small *2θ*. The structural relationship between the lattice parameters of the ternary and quaternary phase were confirmed by TEM measurements: In a sample of **BeIM-MIF(Pro)** all lattice parameters of **[Zn(BeIM)Pro]** and additionally the stacking reflections at ~2.9 nm were observed (Figure 6.3 and Table 6.1). The *d*-values obtained from TEM measurements fit well with the XRD powder pattern.

Overview TEM images showing the morphology of the material clearly indicate a foliated material which is growing anisotropically in lateral dimensions. The sample is highly unstable under the electron beam and thus recording of SAD patterns was only possible in “blind mode” by scanning randomly and without proper alignment of the sample. Short acquisition times are the reason for a high signal/noise ratio due to decomposition of the material by the electron beam.

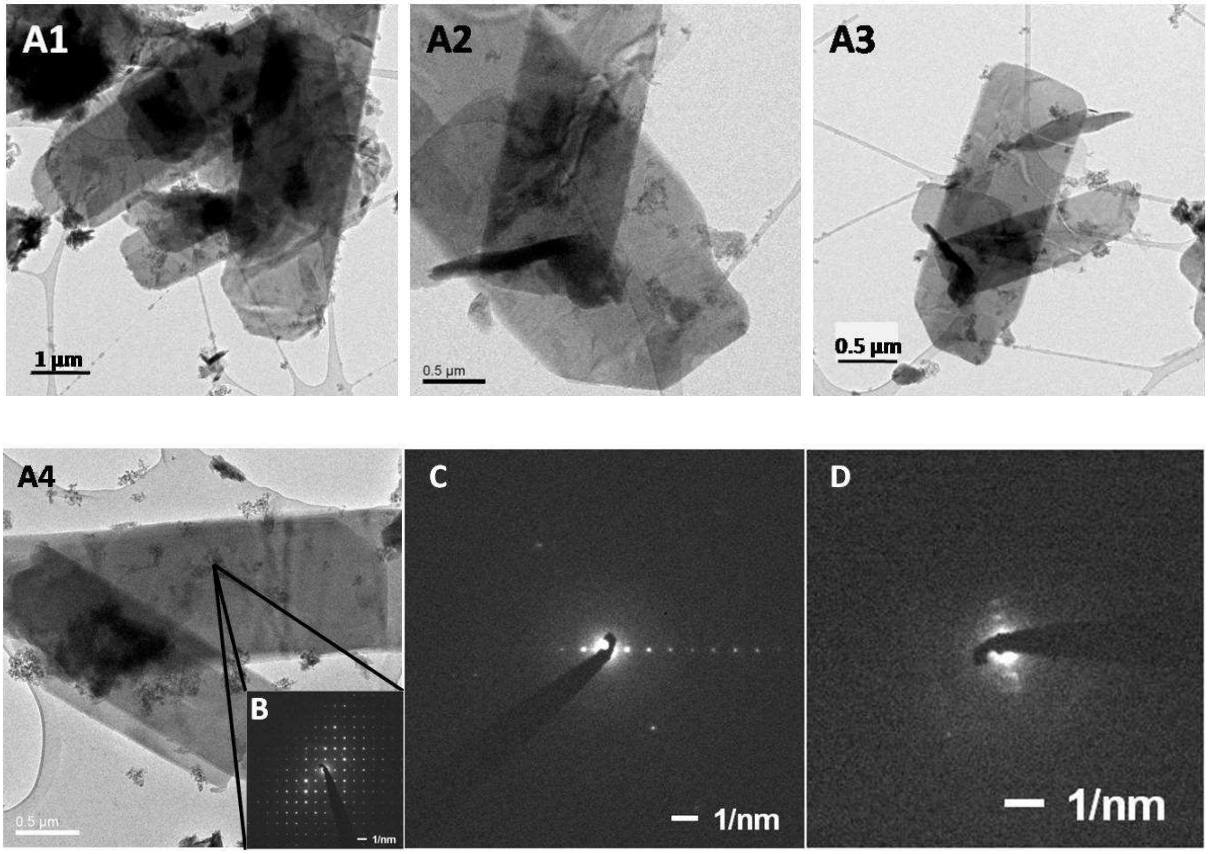


**Figure 6.3** TEM/SAED images of **BeIM-MIF(Pro)**. A1-A4) TEM images showing the slab like morphology of **BeIM-MIF(Pro)** and the corresponding SAD image. Further SAED images reveal the following lattice parameters: B) *b*-parameter (~9.7 Å) and *c*-parameter (~8.8 Å), C) *a*-parameter (~12.2 Å) and D) the stacking reflection (~27 Å).

**Table 6.1** *d*-values obtained from XRD and TEM measurements of **BeIM-MIF(Pro)**.

| *2θ* / ° XRD | *d* values / Å XRD | *d* values / Å TEM measurements |
|---|---|---|
| 3.1 | 28.7 | 27.0 |
| 7.38 | 11.97 | 12.3 |
| 11.74 | 7.53 | 7.72; 7.67 |
| 13.64 | 6.49 | 6.74; 6.75; 6.63 |
| 14.70 | 6.02 | |
| 14.86 | 5.96 | 5.60 |
| 17.30 | 5.12 | |
| 18.30 | 4.84 | (10.03;. 10.3; 10.1;. 10.0; 9.95; 9.94 9.57; 9.98) |
| 19.08 | 4.65 | 4.63 |
| 19.73 | 4.50 | (9.03; 8.94; 8.49; 8.99; 8.86; 8.83) |
| 20.25 | 4.38 | |

| *2θ* / ° XRD | *d* values / Å XRD | *d* values / Å TEM measurements |
|---|---|---|
| 20.94 | 4.24 | 4.16 |
| 21.75 | 4.08 | 4.10; |
| 22.06 | 4.03 | 4.06; 4.03 |
| 22.23 | 3.99 | (7.96; 7.72; 7.71; 8.05) |
| 22.42 | 3.96 | |
| 22.61 | 3.93 | |
| 23.48 | 3.79 | |
| 23.90 | 3.72 | 3.75 |
| 24.24 | 3.67 | |
| 24.85 | 3.58 | |
| 27.66 | 3.22 | 3.31; 3.33; 3.28; 3.24 |
| 28.13 | 3.17 | 3.15; 3.16 3.20 |
| 28.53 | 3.13 | 3.13 |
| 28.76 | 3.10 | |
| 29.04 | 3.07 | |
| 29.39 | 3.04 | |
| 29.52 | 3.02 | |

### 6.1.2 Solid-State NMR Spectroscopy

The solid-state $^{13}C$ CP-MAS NMR spectra of **BeIM-MIF(Pro)** and **[Zn(BeIM)Pro]** are shown in Figure 6.4. Both spectra correspond to those of the (CTAB/)Zn/BeIM/OAc systems. They do not show the signals of the starting materials BeIM(H) or $Zn(Pro)_2$ (compare with Table 6.2), indicating a complete conversion. In the range between 150 ppm to 110 ppm the signals of BeIM can be identified, yet in comparison to proton bearing BeIM(H) all signals are shifted to lower field. Especially the signal C2 between the two coordinating nitrogen atoms is shifted from 141.5 ppm in BeIM(H) to 147.7 ppm,which is an indication of anionic [$BeIM^-$]. The assignment of the individual benzimidazole carbon signals are shown in Table 6.2. The signals of anionic [$Pro^-$] are visible in **[Zn(BeIM)Pro]** at 10.4 ppm ($\delta CH_3$-$CH_2$-$CO_2$), 29.7 ppm ($CH_3$-$\delta CH_2$-$CO_2$), and 185.2 ppm ($CH_3$-$CH_2$-$\delta CO_2$), which is different from the free acid HPro (8.9 ppm, 27.6 ppm and 181.5 ppm) and $Zn(Pro)_2$ (9.1 ppm, 26.5 ppm and

185.3 ppm). The observed values for [Pro$^-$] are similar to the corresponding signals in **BeIM-MIF(Pro)**.

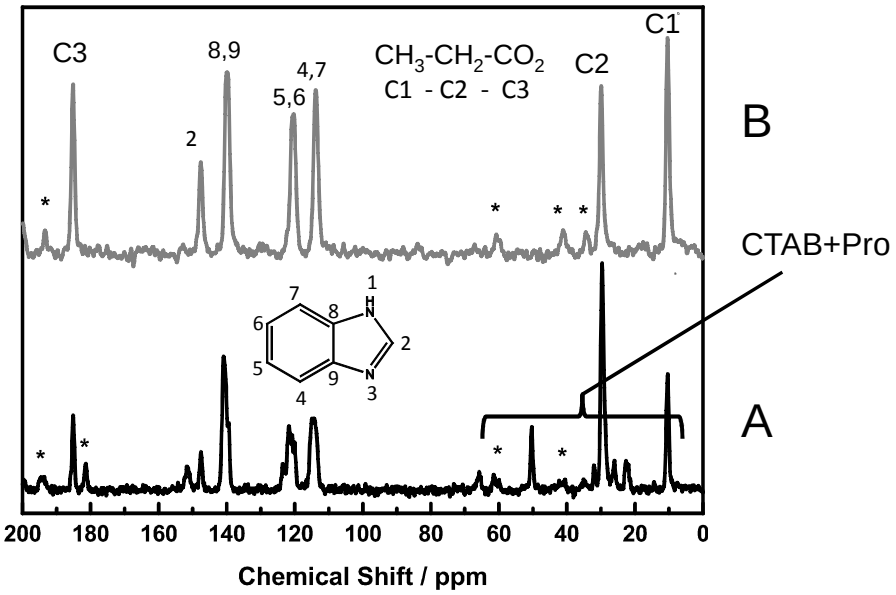


**Figure 6.4** Solid-state $^{13}$C CP-MAS NMR spectra of A) **BeIM-MIF(Pro)** and B) **[Zn(BeIM)Pro]**. Signals marked with an asterisk are spinning-side bands.

All in all, the splitting patterns and chemical shifts of anionic [BeIM$^-$] and [Pro$^-$] are the same in the ternary and quarternary systems, indicating a similar chemical environment of the building blocks and a structural relationship, which is also visible in the XRD powder patterns.

**Table 6.2** Experimental and literature $^{13}C$ NMR chemical shifts (in ppm) of **BeIM-MIF(Pro)**, **[Zn(BeIM)Pro]**, BeIM(H), ZIF-7, HPro and $Zn(Pro)_2$.

| $^{13}C$ NMR | $\delta CH_3$-$CH_2$-$CO_2$ | $CH_3$-$\delta CH_2$-$CO_2$ | $CH_3$-$CH_2$-$\delta CO_2$ | $\delta$C2 | $\delta$C4,7 | $\delta$C5,6 | $\delta$C8,9 |
|---|---|---|---|---|---|---|---|
| **BeIM-MIF(Pro)** | 10.4 | 29.7 | 185.2 | 151.7 | 114.9 | 123.0 | 140.9 |
| | | | 181.4 | 147.6 | 114.4 | 120.8 | 139.4 |
| **[Zn(BeIM)Pro]** | 10.5 | 30.0 | 185.1 | 147.7 | 113.8 | 120.3 | 140.0 |
| ZIF-7 | | | | 149.9 | 114.9 | 122.5;125.3 | 138.1;140.3 |
| BeIM(H) | | | | 141.5 | 115.4 | 122.9 | 137.9 |
| HPro* | 181.5 | 27.6 | 8.9 | | | | |
| $Zn(Pro)_2$ | 9.1 | 26.5 | 185.3 | | | | |

In the spectrum of **BeIM-MIF(Pro)** additional signals of CTAB are visible. The shift of CTAB in the solid-state $^{13}C$ CP-MAS NMR ranging from 55.1 ppm to 14.3 ppm is similar to other known mesostructured systems containing CTAB.[166, 195] Some signals of the methylene chains of CTAB partly overlap with the alkylsignals of Pro (Table 6.3). Especially the signal $CH_3$-$\delta CH_2$-$CO_2$ at ~30 ppm exhibits the same shift as the methylene carbons C5'-C15' in CTAB. In the solid-state $^{15}N$ CP-MAS NMR spectra only the signals of anionic [$BeIM^-$] N1/N3 (-194.3 ppm/-187.2 ppm for **BeIM-MIF(Pro)** and -194.6 ppm for **[Zn(BeIM)Pro]**, respectively), but not the signals of the [R-$N(CH_3)_3^+$]-group of CTAB located at ≈ -331.3 ppm[166] are visible (Table 6.3; Figure 6.5). **BeIM-MIF** consists of alternating **[Zn(BeIM)OAc]**$_n$ ($n$=5-6) and CTAB building blocks (Scheme 5.1, Chapter 5). The signal at -194.4 ppm represents the **[Zn(BeIM)OAc]**$_n$ units. The broader signal at -187.2 ppm (also visible in **BeIM-MIF**) could be an indication for a slight charge redistribution at the BeIM nitrogen sites in the outer **[Zn(BeIM)Pro]** layers, which are in direct contact with CTAB.

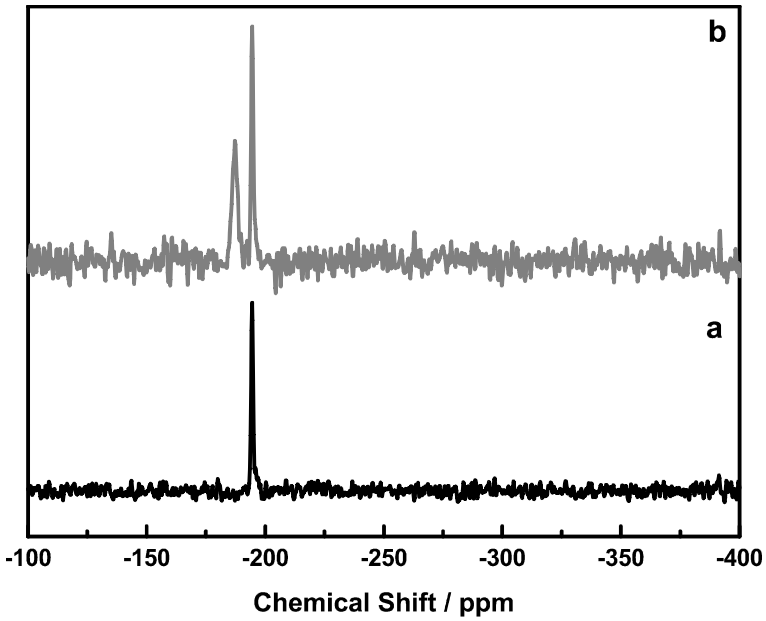


**Figure 6.5** Solid-state $^{15}$N CP-MAS NMR spectra of a) **[Zn(BeIM)Pro]**and b) **BeIM-MIF(Pro)**.

**Table 6.3** Experimental $^{15}$N CP-MAS NMR chemical shifts (in ppm) and assignments pertaining to the surfactant moiety in **BeIM-MIF(Pro)** and the respective surfactant CTAB.

| $^{15}$N NMR / ppm | $\delta N_1$ |
|---|---|
| **BeIM-MIF(Pro)** | -187.2;-194.5 |
| **BeIM-MIF** | -187.2; -194.3 |
| **[Zn(BeIM)Pro]** | -194.6 |
| **[Zn(BeIM)OAc]** | -194.4 |
| BeIM(H) | -145.2 |
| ZIF-7 | -192.4 |

### 6.1.3 Elemental analysis

As for the ternary Zn/BeIM/OAc system elemental analysis (EA+ICP) was also performed for the ternary system Zn/BeIM/Pro,yielding a molar ratio of $[Zn^{2+}] : [BeIM^{-}] :[RCO_2^{-}]= 1 : 1 : 1$

(R = $CH_3$ or $CH_3CH_2$), which again corroborates the isotypic structural relationship between the two compounds (Table 6.4).

**Table 6.4** Elemental analysis of **[Zn(BeIM)(Pro)]** with formula $M(C_{10}H_{10}O_2N_2Zn)$ = 255.58 g $mol^{-1}$.

| | **Zn** | **N** | **C** | **H** | **O** |
|---|---|---|---|---|---|
| 1st sample | 22.29 | 10.76 | 48.56 | 4.56 | 13.83 |
| 2nd sample | 25.28 | 10.42 | 44.93 | 3.86 | 15.51 |
| average | 23.79 | 10.96 | 46.99 | 3.94 | 12.53 |
| calc. | 25.58 | 10.96 | 46.99 | 3.94 | 12.53 |

### 6.1.4 Conclusion

It can be seen from the elemental analysis (EA + ICP), solid-state NMR spectroscopy and XRD that the quarternary system CTAB/Zn/BeIM/Pro can be traced back to the 2D layered compound **[Zn(BeIM)Pro]** (thickness ≈ 1.2 nm) interacting with CTAB, forming a periodic mesostructured compound similar to **BeIM-MIF**, yet with a mesostructure period of ~29 Å instead of 84 Å. Therefore, the CTAB layers in **BeIM-MIF** have an average thickness of about ~1.7 nm. A model of a regular periodic mesostructure with a repeat distance of ~ 30 Å can only be verified by assuming strictly alternating CTAB monolayers with individual **[Zn(BeIM)Pro]** sheets (Figure 6.6).

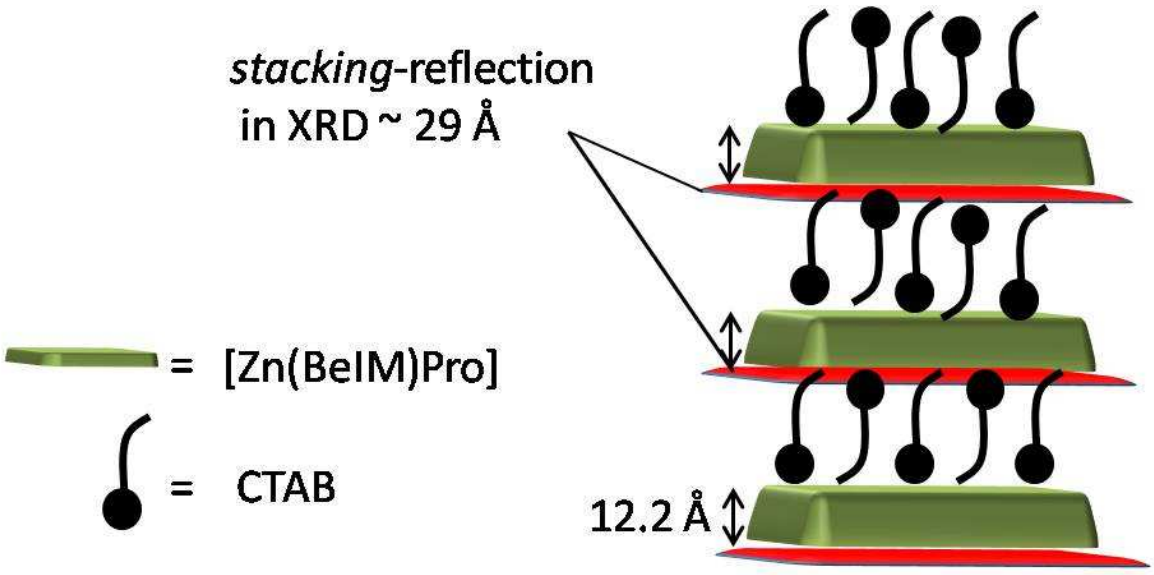


**Figure 6.6** Structural model for periodic **BeIM-MIF(Pro)**.

## 6.2 Butyric acid (Buto)

### 6.2.1 Synthesis of zinc butyrate ($Zn(Buto)_2$)

The system discussed in the previous chapter 6.1 was transferred to Zn/BeIM/Buto by replacing HPro with butyric acid (HButo, $CH_3CH_2CH_2CO_2$). As $Zn(Buto)_2$ is not commercially available, it was synthesized under reflux conditions in EtOH.[253] The product was analyzed with solid-state $^{13}C$ CP-MAS NMR (Figure 6.9c), elemental analysis (Table 6.5) and XRD. Four carbon signals were observed in the $^{13}C$ CP-MAS NMR of $Zn(Buto)_2$at13.5 ppm ($\delta$C1'), 19.3 ppm ($\delta$C2'), 37.1 ppm ($\delta$C3'), 184.6 ppm ($\delta$C4'), which are all shifted compared to HButo (13.7 ppm ($\delta$C1'), 18.4 ppm ($\delta$C2'), 36.2 ppm ($\delta$C3'), 180.7 ppm ($\delta$C4')). Within the limits of accuracy, no impurities were found in the XRD powder pattern. The conversion of the reaction was quantitative.

**Table 6.5** Elemental analysis of [Zn(Buto)$_2$] with formula $M(C_8H_{14}O_4Zn)$ = 239.58 g mol$^{-1}$.

| | **Zn** | **O** | **C** | **H** |
|---|---|---|---|---|
| Exp. | 25.4 | 28.7 | 40.0 | 5.9 |
| calc. | 27.3 | 26.7 | 40.1 | 5.9 |

### 6.2.2 [Zn(BeIM)Buto] and BeIM-MIF(Buto)

A layered compound in the ternary system Zn/BeIM/Buto was obtained *via* a solid-state reaction by mixing Zn(Buto)$_2$ and BeIM in a ratio of 1 : 1 in closed glass ampoules under argon, followed by heating to 180 °C for 16 h. Excess butyric acid was washed away with EtOH from the resulting colorless powder, named **[Zn(BeIM)Buto]**. The reaction is also possible in methanol. The analogues **[Zn(BeIM)R]** (R = OAc, Pro) can be synthesized by a solid-state reaction in closed ampoules as well. This synthesis procedure may be a good way in future experiments to obtain single crystals for structure solution from unknown and more complex hybrid systems.

When working under microemulsion conditions (See Experimental Section 6.4.3) in the quaternary system CTAB/Zn/BeIM/Buto, a colorless powder was obtained, dubbed **BeIM-MIF(Buto).**

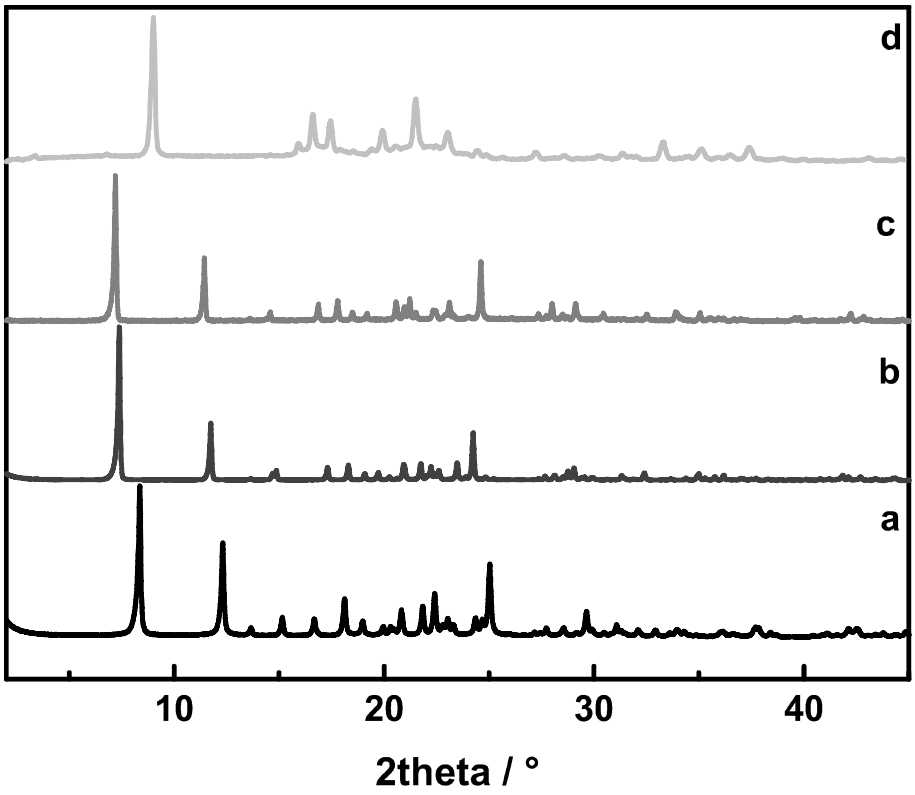


**Figure 6.7** XRD powder patterns of a) **[Zn(BeIM)OAc]**, b) **[Zn(BeIM)Pro]**, c) **[Zn(BeIM)Buto]** and d) **BeIM-MIF(Buto)**.

### 6.2.3 X-Ray Powder Diffraction

The XRD powder patterns of **[Zn(BeIM)Buto]** and **BeIM-MIF(Buto)** are shown in Figure 6.7. They were both compared with the starting materials and other related compounds, and both show no impurity of known compounds (starting materials, ZnO, etc.), which is an indication for the total conversion of the reactants. The XRD powder pattern of **[Zn(BeIM)Buto]** was indexed on space group $P2_1/c$, $a$ = 11.69Å, $b$ = 9.92Å, $c$ = 8.77 Å, $\beta$ = 92.36°, which confirmed that isotypic structures were obtained for the carbonic acid homologues in the compounds of type **[Zn(BeIM)R]** (R = OAc, Pro and Buto) (Figure 6.8). Comparing the powder patterns of **[Zn(BeIM)Buto]** and **BeIM-MIF(Buto)**, however, no similarity is observed unlike in the systems **BeIM-MIF** and **[Zn(BeIM)OAc]**, which illustrates the absence of a pronounced structural relationship between the two systems.

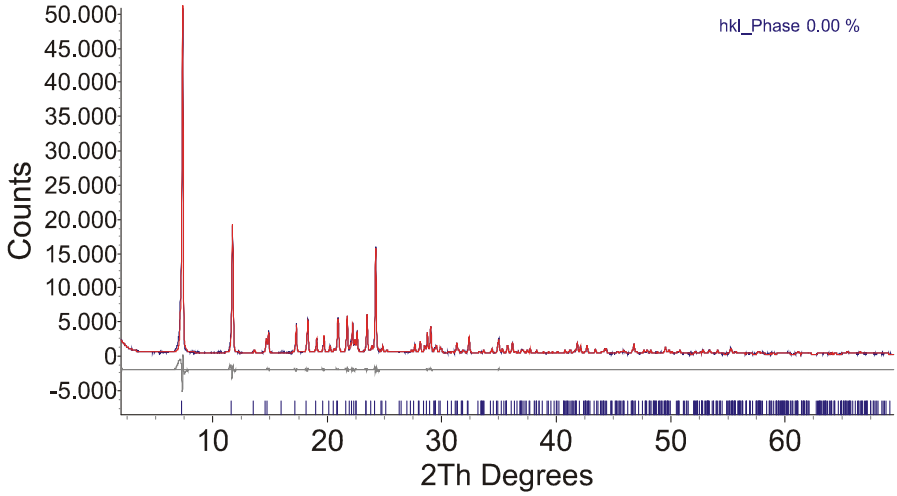


**Figure 6.8** Pawley Fit on powder XRD data of **[Zn(BeIM)Buto]**, yielding space group and metric parameters $P2_1/c$, $a$ = 11.69 Å, $b$ = 9.92 Å, $c$ = 8.78 Å, β = 92.36°, GoF = 1.128.

### 6.2.4 Solid-state NMR Spectroscopy

The solid-state $^{13}$C CP-MAS NMR measurements confirm the assumption that no obvious structural correlation between **BeIM-MIF(Buto)** and **[Zn(BeIM)Buto]** (Figure 6.9) exists. The chemical shifts of the anionic [BeIM$^-$] in **[Zn(BeIM)Buto]** are expected to appear between 150 ppm and 110 ppm, which matches well with the chemical shift of the C2 atom at 147.2 ppm indicating the deprotonation of BeIM(H). The splitting pattern of the NMR signals assigned to [BeIM$^-$] matches the pattern found in the analogous **[Zn(BeIM)R]** (R = OAc, Pro) systems (chapter 5+6.1). For the$^{13}$C carbon chemical shifts in the alkyl range three signals of the alkylchain of [Buto$^-$] are observed (14.0 ppm ($\delta$C1'), 18.9 ppm ($\delta$C2') and 36.9 ppm ($\delta$C3')). The signal of the deprotonated carboxyl group ($\delta$C4') is shifted to lower field at 184.8 ppm (Buto(H) 180.7 ppm), similar to the shift in Zn(Buto)$_2$ (184.6 ppm). The assignment of the individual carbon signals can be found in Table 6.6.

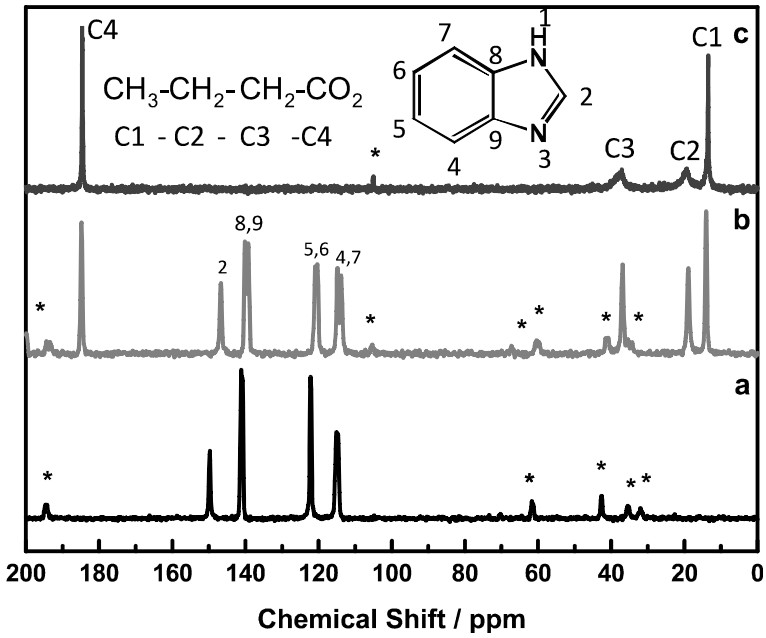


**Figure 6.9** Solid-state $^{13}C$ CP-MAS NMR spectra of a) **BeIM-MIF(Buto)**. The shift and the splitting pattern of the anionic [BeIM$^-$] signals indicate the formation of a ZIF network with unknown topology. Buto and CTAB are not contained in the network. NMR spectra of b) **[Zn(BeIM)Buto]** and c) $Zn(Buto)_2$.

The solid-state $^{13}C$ CP-MAS NMR spectrum of **BeIM-MIF(Buto)** only shows the signals of anionic [BeIM$^-$] in the range of 150 ppm to 110 ppm and no trace of butyric acid, neither de-protonated nor protonated. The chemical shifts and splitting pattern of [BeIM$^-$] are in good agreement with **[Zn(BeIM)R]** (R= OAc, Pro) and ZIF-7 ($Zn(BeIM)_2$), portending that [BeIM$^-$] is coordinated in anionic form to the Lewis acid [$Zn^{2+}$]. Additionally, no signals of CTAB in the range of about 66 ppm - 20 ppm are visible. Thus, the conclusion was made that under these conditions for **BeIM-MIF(Buto)** it was not possible to form either the expected mesostructured compound, like **BeIM-MIF** or **BeIM-MIF(Pro)** nor **[Zn(BeIM)Buto]**.

**Table 6.6** Experimental and literature-derived $^{13}C$ NMR chemical shifts (in ppm) of **BeIM-MIF(Buto)**, **[Zn(BeIM)Buto]**, BeIM(H), ZIF-7, HButo and $Zn(Buto)_2$.

| $^{13}C$ MAS NMR | $\delta CH_3$ $CH_2$- $CH_2$- $CO_2$ | $CH_3\delta C$ $H_2$- $CH_2$- $CO_2$ | $CH_3$- $CH_2$- $\delta CH_2$- $CO_2$ | $CH_3$- $CH_2$- $CH_2$- $\delta CO_2$ | $\delta$C2 | $\delta$C4,7 | $\delta$C5,6 | $\delta$C8,9 |
|---|---|---|---|---|---|---|---|---|
| **BeIM-MIF(Buto)**[1] | | | | | 149.8 | 115.1 | 122.2 | 141.2 |
| **[Zn(BeIM)Buto]** | 14.0 | 18.9 | 36.9 | 184.8 | 146.7 | 114.9<br>113.8 | 120.9<br>120.3 | 140.1<br>139.2 |
| ZIF-7 | | | | | 149.9 | 114.9 | 122.5;125.3 | 138.1;140.3 |
| BeIM(H) | | | | | 141.5 | 115.4 | 122.9 | 137.9 |
| HButo* | 13.7 | 18.4 | 36.2 | 180.7 | | | | |
| $Zn(Buto)_2$ | 13.5 | 19.3 | 37.1 | 184.6 | | | | |

* measured in $CDCl_3$;[1];**BeIM-MIF(Buto)** is a ZIF-network with unknown topology.

### 6.2.5 Elemental analysis

The oxygen weight percent is indirectly determined by O% = 100(%) - Zn(%) – H(%) – C(%) – N(%). No oxygen was found in **BeIM-MIF(Buto)**, again indicating the absence of the carbonic acid (Table 6.8). The elemental analysis of **BeIM-MIF(Buto)** reveals a ratio of $[Zn^{2+}] : [BeIM^-]$ of 1 : 2, which is commonly found in dense imidazolates and ZIF compounds.[100] However, for **[Zn(BeIM)Buto]** a ratio of 1 : 1 : 1 of the individual building blocks $[Zn^{2+}] : [BeIM^-] : [Buto^-]$ was found (Table 6.7), which is in agreement with the above data.

**Table 6.7** Elemental analysis of [Zn(BeIM)(Buto)] with formula $M(C_{11}H_{12}O_2N_2Zn)$ = 269.60 g $mol^{-1}$.

| | **Zn** | **N** | **C** | **H** | **O** |
|---|---|---|---|---|---|
| Exp. | 23.42 | 10.36 | 48.96 | 4.52 | 13.16 |
| calc. | 24.25 | 10.39 | 49.00 | 4.49 | 11.87 |

´**Table 6.8** Elemental analysis of **BeIM-MIF(Buto)** synthesized under microemulsion conditions. The results from solid-state $^{13}C$ CP-MAS NMR spectroscopy and elemental analysis indicate the synthesis of an unknown ZIF phase ($Zn(BeIM)_2$) with formula $M(C_{14}H_{10}N_4Zn)$ = 299.64 g $mol^{-1}$.

| | **Zn** | **N** | **C** | **H** |
|---|---|---|---|---|
| Exp. | 22.41 | 17.76 | 56.04 | 3.88 |
| calc. | 21.82 | 18.70 | 56.12 | 3.36 |

### 6.2.6 Conclusion

The coordination polymer **[Zn(BeIM)Buto]**, which is isotpyic with [Zn(BeIM)R] (R=OAc, Pro), was isolated in a solid-state reaction and characterized by XRD, solid-state $^{13}C$ CP-MAS NMR and elemental analysis. However, the results from elemental analysis and solid-state $^{13}C$ CP-MAS NMR point out that under microemulsion conditions in the presence of CTAB a dense benzimidazolate or ZIF compound with composition $Zn(BeIM)_2$ possibly featuring a 3D network was formed, rather than a hierarchically micro-mesostructured compound composed of **[Zn(BeIM)Buto]** and CTAB, as observed for the other carbonic acids. The powder pattern of **BeIM-MIF(Buto)** was compared to the powder patterns of the two known ZIF compounds with benzimidazole, ZIF-7 and ZIF-11.[100] No similarities were found, which signify that the ZIF network topology of the presented compound is unknown. Interestingly, by replacing $Zn^{2+}$ with $Co^{2+}$ in the system CTAB/Co/BeIM/OAc, and also in the ternary system

Zn/BeIM/OAc, when a solution of BeIM in 1-hexanol was covered with a solution of $Zn(OAc)_2$ in water, a powder pattern identical to **BeIM-MIF(Buto)** was obtained. **BeIM-MIF(Buto)** was not further characterized.

## 6.3 Chapter Summary

In this chapter the relationship between the layered coordination polymers **[Zn(BeIM)R]** (R = OAc, Pro, Buto) was presented. In the structure of **[Zn(BeIM)OAc]**, the alkylchains of the acetate groups are oriented parallel to the stacking direction of adjacent sheets (along the *a*-axis). According to the increase in alkyl chain length of the carboxylic acids in the order OAc → Pro → Buto, a gradual increase of the *a*-axis can be observed. The metric parameters in the lateral dimensions (*b* and *c*-parameter) are unchanged within measurement errors.

Contrary to the system CTAB/Zn/BeIM/Buto, microemulsion conditions in the system CTAB/Zn/BeIM/Pro furnish a mesostructured compound (**BeIM-MIF(Pro)**). The diffraction pattern of this structure shows additional reflections corresponding to a lamellar mesostructure with a stacking distance of 29 Å compared to 84 Å in the acetate system. It was also shown that the structure of **BeIM-MIF(Buto)** is not related to the **[Zn(BeIM)R]** structures (R = OAc, Pro, Buto) in that it does not show the same layered morphology based on [Zn(BeIM)R] building blocks as seen in chapter 5.

## 6.4 Experimental Section

### 6.4.1 Synthesis of $Zn(Buto)_2$

ZnO (10 g, 0.112 mol) was mixed with butyric acid (33.63 mL, 0.368 mol) in 200 mL ethanol under reflux conditions for 2 h. The white precipitate, collected by centrifugation, was washed with ethanol and petroleum ether and dried at room temperature.

### 6.4.2 Synthesis of [Zn(BeIM)R], R = Pro, Buto

0.118 g BeIM (1.0 mmol) and 0.211 g $Zn(Pro)_2$ (1.0 mmol) (or 0.239 g $Zn(Buto)_2$) were thoroughly ground and filled in a dried Duran glass tube ($ø_{ext.}$= 10 mm, $ø_{int.}$ = 7 mm). The tube was evacuated, sealed under argon atmosphere at a length of 12 cm and placed in an inclined tube furnace. The oven was heated with a rate of 60°C · $h^{-1}$ to 180 °C, held for 10 h, cooled to 105 °C with a rate of 1 C· $h^{-1}$ and cooled to room temperature with 60 °C · $h^{-1}$. The colorless product was washed with ethanol and dried over night at room temperature.

### 6.4.3 Synthesis of BeIM-MIF(R), R = Pro, Buto

**BeIM-MIF**(R) was synthesized in a typical procedure by adding 5.4 mL BeIM (0.60 M in 1-hexanol) and 2.7 mL zinc propionate (or zinc butyrate) (1.20 M in water) to a suspension containing a mixture of 0.05 M CTAB in *n*-heptane/1-hexanol (200 mL). The mixture was heated for 16 h and yielded a white precipitate. The white powder was isolated by centrifugation (10000 rpm for 5 min) and dried over night at room temperature.

# 7 The mesostructured zinc benzimidazolate „BeIM-MIF-40“

A mesostructured zinc benzimidazolate (**BeIM-MIF-40)**, distinct from **BeIM-MIF** described in chapter 5, was obtained under the same synthetic conditions as those used for the synthesis of **BeIM-MIF**. Either **BeIM-MIF** or **BeIM-MIF-40** were isolated, a mixture of these two phases was never observed. Experimental parameters such as reaction temperature and solution composition were modified to optimize the reaction conditions for each phase, however no coherence was recognized and it was therefore not possible to ascertain the exact synthesis conditions for this phase. As the reproducibility of this particular phase is limited, this chapter only contains a brief overview of the results obtained so far, which are discussed in the context of the related compound **BeIM-MIF**.

## 7.1 X-Ray Powder Diffraction and TEM measurements

**BeIM-MIF-40**, a white solid, was characterized by XRD powder diffraction (Figure 7.1).

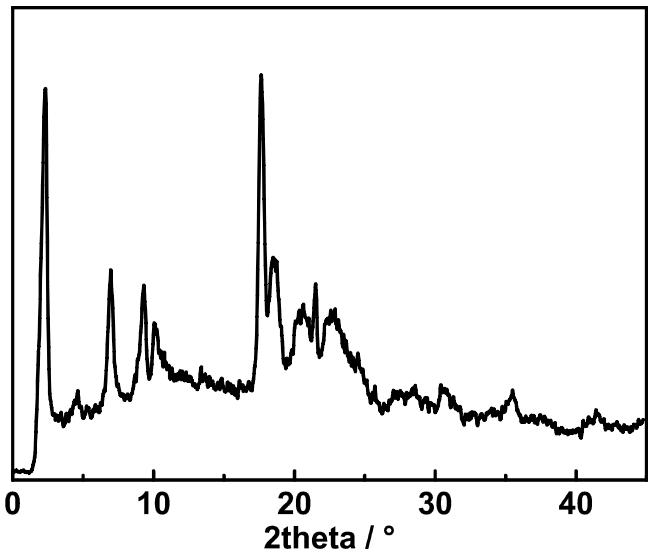


**Figure 7.1** XRD powder pattern of **BeIM-MIF-40**.

The XRD measurement shows a series of equidistant *00l*-reflections at small angles starting from a *d*-value of 38 Å (approximately half of **BeIM-MIF**: ~80 Å), which indicates the formation of a periodic hierarchically structured compound. Rather broad reflections were observed at high angles, which implies that the material is not well ordered on the molecular level in comparison to **BeIM-MIF**. However, the basal distance of 38 Å does not correspond to known lamellar bilayers (52 Å) or single layer models (26 Å) containing CTAB.[166, 183-188] The TEM bright field measurement (Fig. 7.2A) shows that the material is built up of alternate lamellae of different thicknesses discernible by the varying contrast, which was also observed for **BeIM-MIF**. This array of alternating layers presumably represents a CTAB layer sandwiched between hybrid layers of **[Zn(BeIM)OAc]**. SAED images (Fig. 7.2B+C) reveal *d*-values which match well with the values deduced from the XRD powder pattern. Further TEM tilting experiments show that the lamellar structure is present in one direction whilst the structure resembles nanosheets in the two other directions (Fig. 7.2D+E).

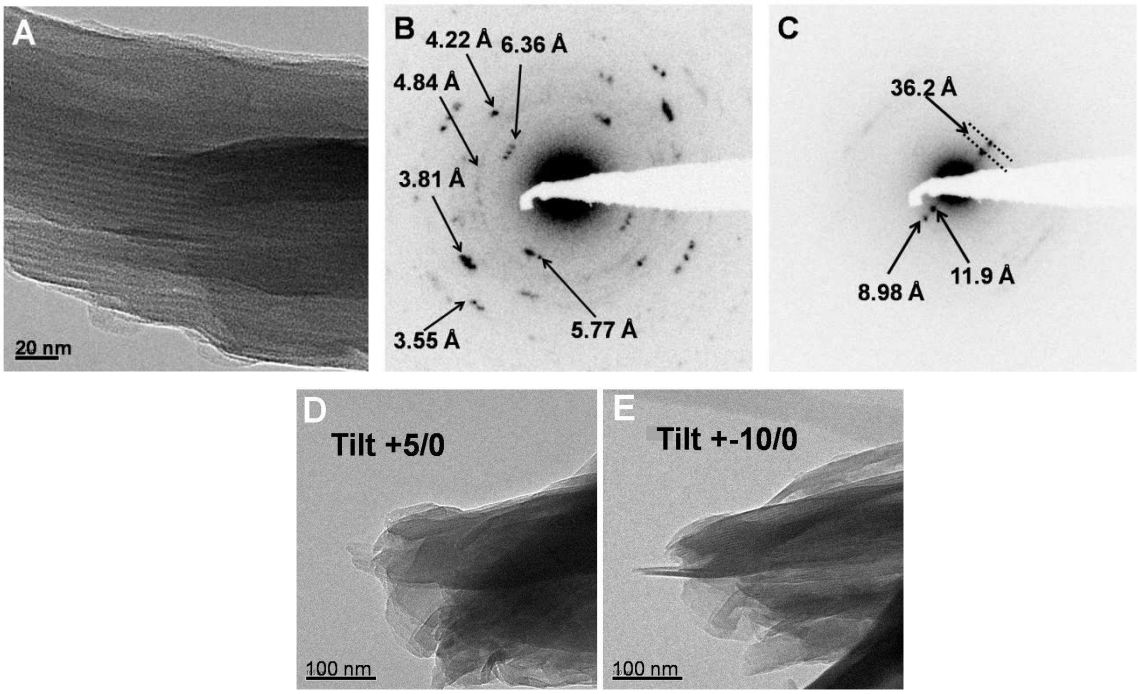


**Figure 7.2** TEM images of **BeIM-MIF-40** showing A) a side view onto the lamellae (stacking distance ~37 Å),

B+C) SAED patterns showing the extracted *d*-values, and D+E) a TEM tilt series of **BeIM-MIF-40** representing the lamellar mesostructure. The images were obtained by rotating the TEM sample holder starting from +5° to -10°.

## 7.2 Solid-state NMR Spectroscopy

The solid-state $^{13}C$ CP-MAS NMR spectrum of **BeIM-MIF-40** (Figure 7.3) shows that the compound contains BeIM (150 - 100 ppm), acetate (~180 ppm) and CTAB (~65 – 20ppm). By comparing the spectrum of the product with the respective spectra of the starting materials, it is evident that the spectrum is not a superposition of the starting materials. The shifting and splitting pattern of CTAB ranges from 55.1 ppm to 14.3 ppm in the $^{13}C$ CP-MAS NMR of **BeIM-MIF-40**. A similar splitting pattern is observed also in the$^{13}C$ NMR spectra of numerous mesostructured systems containing CTAB.[166, 195]

All $^{13}C$ NMR peak positions of BeIM close to the deprotonated position N1/N3 such as C8/C9 and C2 are shifted to lower field (146.6 ppm/140.9 ppm vs. 134.9 ppm for C8/9 and 151.7. ppm vs. 141.7 ppm for C2). The other signals of the benzene ring (C4/7 at 114.7/113.5 ppm and C5/C6 121.3 ppm/120.3 ppm) are split. The $^{13}C$ peak positions are shifted and have almost the same multiplett pattern as anionic [$BeIM^-$][245] in **[Zn(BeIM)OAc]**, which suggests complete deprotonation of BeIM.

The solid state $^{13}C$ CP-MAS NMR spectrum shows two peaks in the carboxylate range at 182.9 and 178.3 ppm, which originate from acetate. The $^{13}C$ NMR (liquid, $CDCl_3$) of HOAc shows signals at 178.1 and 20.8 ppm and the $^{13}C$ CP-MAS NMR of $Zn(OAc)_2 \cdot 2H_2O$ at 183.7 and 19.3 ppm, respectively. Extraction experiments like in **BeIM-MIF-30**, which reveal that protonated acetate is a crucial part of the structure, were not carried out. Therefore, an impurity of HOAc cannot be excluded. Similarly to [$BeIM^-$], the signal at 182.9 ppm suggests that the acetate anion is coordinated to $Zn^{2+}$. In the alkylrange of the $^{13}C$ CP-MAS NMR of

**BeIM-MIF-40** only signals up to 22.5 ppm are visible. Free protonated HOAc should reveal a signal in the range of alkyl groups at around ~20.8 ppm.[164] The coordination polymer substructure of **BeIM-MIF** comprises infinite -$(OAc)_{2/2}$Zn-$(OAc)_{2/2}$-Zn-$(OAc)_{2/2}$ chains, which show a $^{13}$C NMR signal at 183.7 ppm. The signal at 178.3 ppm in **BeIM-MIF-40** could represent chains disconnected and terminatedby protonation (-$(OAc)_{2/2}$-Zn-(HOAc)).

In the solid-state $^{15}$N CP-MAS NMR spectra of **BeIM-MIF-40** two signals are visible for deprotonated BeIM at -194.4 (split) and -187.1 ppm (Figure 7.4). Similar values were found for ZIF-7 (-192.4 ppm) and **[Zn(BeIM)OAc]** (-194.5 ppm), respectively, whereas for protonated BeIM(H) different signals were observed (-145.2 and -223.5 ppm for N1/N3). Consistent with the shifts observed for **BeIM-MIF-40**, **BeIM-MIF** shows two signals at -194.3 and -187.2 ppm. The signal at -187.1 ppm found for **BeIM-MIF** could indicate a different chemical environment as in the outer **[Zn(BeIM)OAc]**-layers, which are in direct contact with CTAB due to the **[Zn(BeIM)OAc]**|CTAB interface.

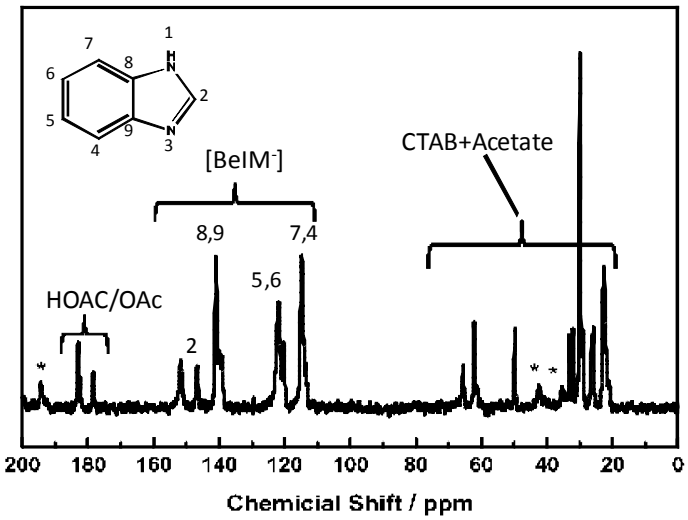


**Figure 7.3** Solid-state $^{13}$C CP-MAS NMR spectrum of **BeIM-MIF-40.** Signals marked with an asterisk are spinning side bands.

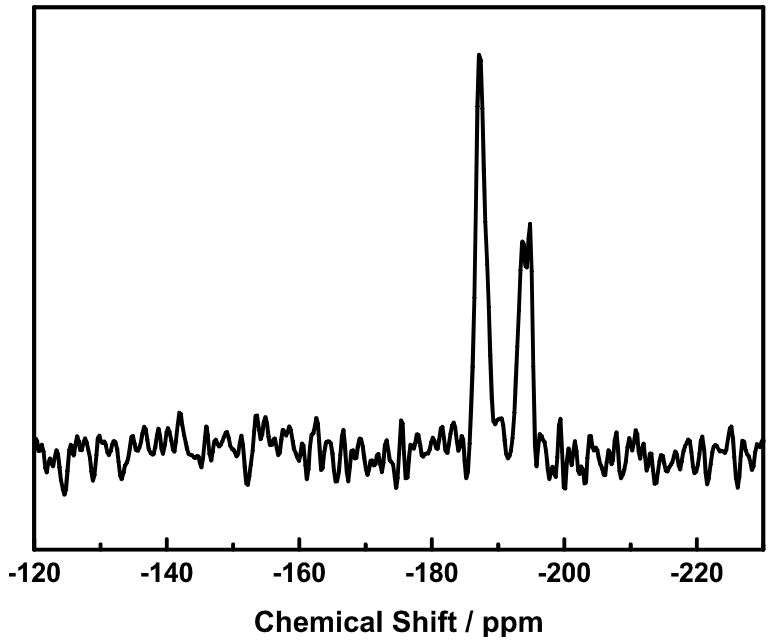


**Figure 7.4** Solid-state $^{15}N$ CP-MAS NMR spectra of **BeIM-MIF-40**.

## 7.3 IR Spectroscopy

The IR spectrum shows the presence of CTAB in **BeIM-MIF-40** through the two characteristic $\nu(CH_2)$-stretching vibrations at 2850 $cm^{-1}$ and 2915 $cm^{-1}$. Additionally, the fingerprint region shows characteristic BeIM and OAc ($\nu$(C=O)-stretching at 1542 $cm^{-1}$/1454 $cm^{-1}$) deformation and wagging modes.[165] The $^{13}C$ NMR reveals the presence of protonated OAc in the structure. In the IR spectrum of **BeIM-MIF-40** the broad $\nu$(OH) and $\nu$(NH) stretching modes above 1800 $cm^{-1}$(Fig. 7.5) are hardly discernible. This indicates mainly the absence of hydrogen-bonded proton bearing acetic acid and benzimidazole.

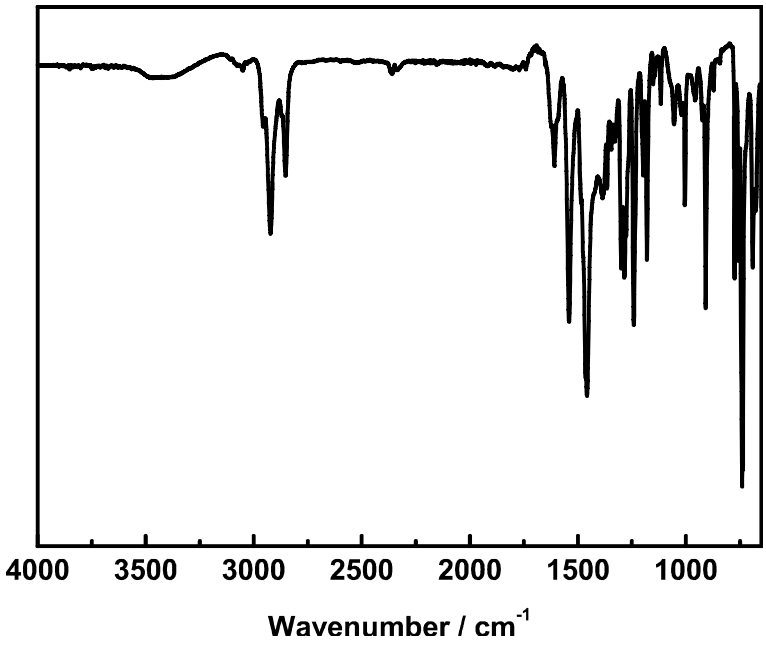


**Figure 7.5** IR spectrum of **BeIM-MIF-40**.

## 7.4 Elemental analysis

The elemental analysis of **BeIM-MIF-40** represents a ratio of $[Zn^{2+}]$ : $[BeIM^-]$ : $[OAc^-]$ : [CTAB] = 4 : 4.5 : 3.5 : 1 (Table 7.1). The elemental analysis is similar to that for **BeIM-MIF**, where also a slight excess of $[BeIM^-]$ with respect to $[OAc^-]$ was observed ($[Zn^{2+}]$ : $[BeIM^-]$ : $[OAc^-]$ : [CTAB] = 7 : 7.5 : 6.5 : 1). As for **BeIM-MIF**, the ratio of metal to ligands $[Zn^{2+}]$ : $[BeIM^-]$ : $[OAc^-]$ in **BeIM-MIF-40** is about the same as in **[Zn(BeIM)OAc]**, namely ~ 1 : 1 : 1.

**Table 7.1** Elemental analysis of **BeIM-MIF-40** with formula $\{[(Zn_4\ (BeIM)_{4.5}OAc_{3.5})]\cdot CTAB\}$ and $M(C_{115}H_{149}Br_2N_{20}O_{14}Zn_8)$ = 2718.4217 g/mol.

| | **Zn** | **N** | **C** | **H** | **Br** | **O** |
|---|---|---|---|---|---|---|
| 1st sample | 19.0 | 10.4 | 51.9 | 5.9 | 5.9 | 6.9 |
| 2nd sample | 19.4 | 10.5 | 51.6 | 5.6 | 5.9 | 7.0 |
| 3rd sample | 19.0 | 10.5 | 51.6 | 5.8 | 6.1 | 7.1 |
| average | 19.1 | 10.5 | 51.7 | 5.8 | 5.9 | 7.0 |
| calc. | 19.2 | 10.3 | 50.8 | 5.6 | 5.9 | 8.2 |

The results from XRD, elemental analysis and solid state NMR of **BeIM-MIF-40** reveal a close relationship to **BeIM-MIF**, yet a reliable structural model for this phase cannot be devised at this stage. We suggest, however, that **BeIM-MIF-40** can be derived from **BeIM-MIF**, featuring a different amount of [Zn(OAc)BeIM] layers within the hybrid stacks which are interleaved with CTAB, giving rise to a lamellar mesostructure with a periodicity of roughly 4 nm.

# 8 BeIM-MIF-30– A lamellar mesostructured zinc benzimidazolate phase

As outlined in chapter 5 **BeIM-MIF** was synthesized with a 0.50 M CTAB solution in *n*-heptane/1-hexanol under microemulsion conditions. By increasing the concentration of CTAB from 0.5 M to 1 M, a white powder could be isolated, named **BeIM-MIF-30**. The reaction is highly reproducible.

## 8.1 XRD powder diffraction and TEM measurements

The XRD powder pattern of **BeIM-MIF-30** is depicted in Figure 8.1a. It shows a new phase which has a lower crystallinity than **BeIM-MIF** and reveals no obvious structural relationship to the latter. The powder pattern was compared with the patterns of the starting materials. No agreement could be found, indicating a complete conversion of the starting materials. Indexing of the powder pattern was not possible owing to its low quality and the low number of reflections. TEM measurements (Figure 8.2A) show that this compound consists of equidistant lamellae with a spacing of ≈ 30 Å, which is consistent with the presumed *001*-reflection, the first in the series of three *00l*-reflections in the XRD powder pattern. The sample is extremely sensitive to the electron beam, requiring short acquisition times for SAED measurements. Therefore, recording of SAED images was possible only in blind mode, with a random orientation of the sample with respect to the beam. From *in plane* SAED images, which were rarely obtained, hexagonal metrics can be deduced (Figure 8.2B). In different experiments **BeIM-MIF-30** were treated with TEOS (tetraethylorthosilicate) in order to stabilize the lamellar structure by pillaring and therefore make it suitable for TEM measurements. On hierarchically structured MFI zeolite sheets the consolidation effect of TEOS was already described by Na *et al.*[173] In an ideal case the surfactant can be removed completely after stabilization of the material, while the inorganic architecture remains in good order (Scheme 8.1),[178,

[254] whereas without TEOS the lamellar compound would collapse. However, in our case it seems that the TEOS-stabilized hybrid material is still destroyed under the electron beam. Even TEM measurements of the sample still containing the surfactant and TEOS were unsuccessful.

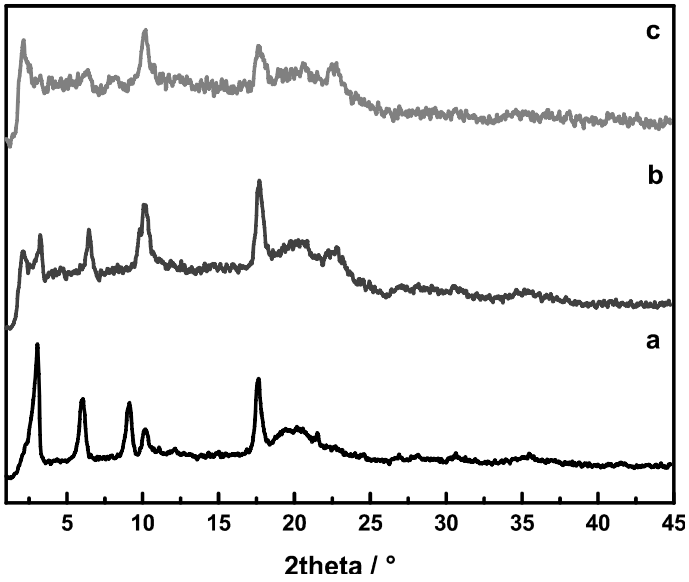


**Figure 8.1** XRD powder patterns of **BeIM-MIF-30** a) unwashed, b) boiled in EtOH for 2 h and c) for 4 h.

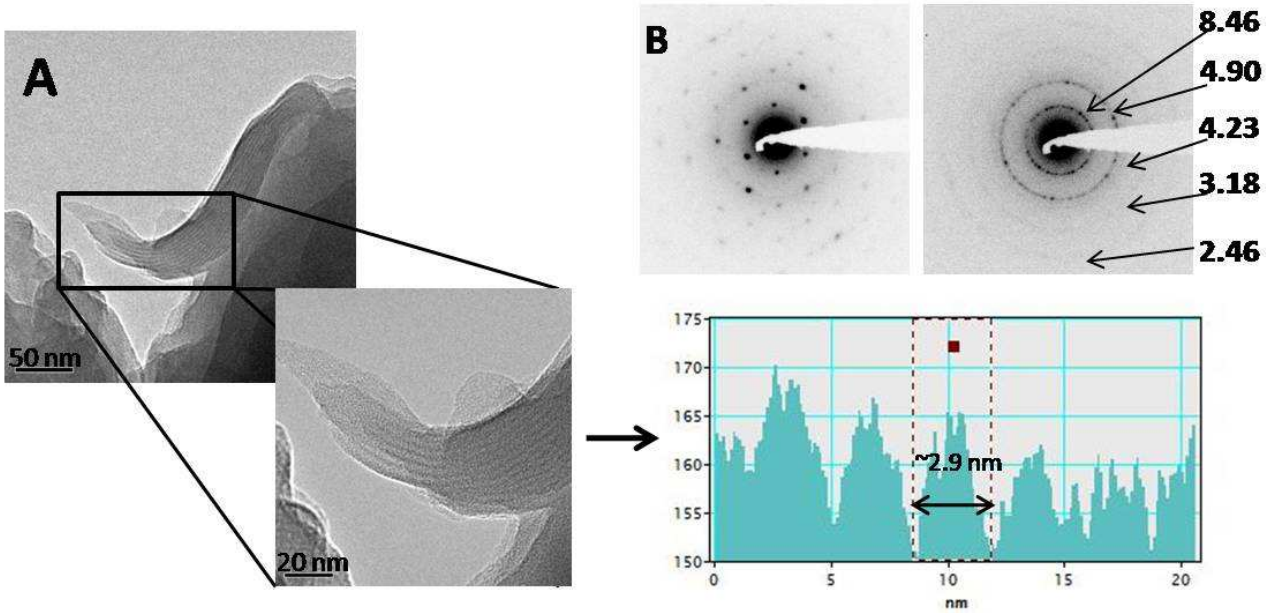


**Figure 8.2** A) TEM measurements of **BeIM-MIF-30**. B) SAED images of **BeIM-MIF-30**.

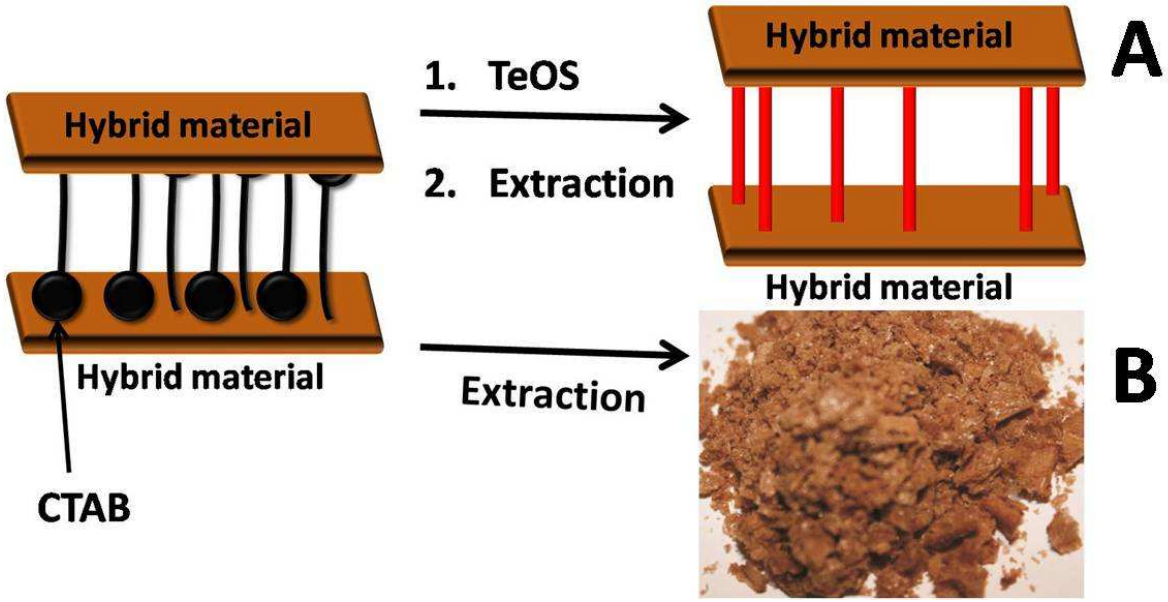


**Scheme 8.1** A) Illustration of the pillaring principle and B) extraction of a lamellar material, without pillaring or when no intercalation of TEOS between the hybrid materials takes place.

**Table 8.1** Comparison of the *d*-values from XRD of **BeIM-MIF-30** with *d*-values obtained from SAD/TEM images.

| *2θ* from XRD / ° | *d* from XRD / Å | *d* values from TEM / Å | |
|---|---|---|---|
| 3.0 | 29.04 | 29 | *00l*-reflections |
| 6.0 | 14.66 | | |
| 9.1 | 9.71 | | |
| 10.1 | 8.69 | 8.5 | *Inplane*-reflections |
| 17.6 | 5.03 | 4.9 | |
| 20.1 | 4.40 | | |
| 21.5 | 4.13 | 4.2 | |
| 26.8 | 3.31 | 3.2 | |
| 30.6 | 2.92 | | |
| 35.5 | 2.52 | 2.5 | |

## 8.2 Solid-state NMR spectroscopy

The solid-state $^{13}C$ CP-MAS NMR spectrum of **BeIM-MIF-30** shows the signals of BeIM (from 150 ppm to 110 ppm), the signals of acetate and CTAB, which gives a first impression of the analogy to **BeIM-MIF** (Figure 8.3). All signals for BeIM are shifted compared to

proton bearing BeIM(H), especially the signal C2 at 151.4 ppm (C2 at 141.5 ppm in BeIM(H)), which indicates anionic [BeIM$^-$]. This is also confirmed by the presence of only one signal for the two nitrogen atoms N1/N3 of [BeIM$^-$] at -187.5 ppm in the $^{15}$N CP-MAS NMR (BeIM(H): -145.20 and -223.53 ppm, Figure 8.4, Table 8.3). In **BeIM-MIF** two signals are observed at -194.3 and at-187.2 ppm. As speculated in chapter 5, the signal at -194.3 ppm may represent the inner **[Zn(BeIM)OAc]**$_n$ sheets while the latter one may indicate a change in the chemical environment of the [BeIM$^-$] sites of the outer **[Zn(BeIM)OAc]** sheets at the boundary **[Zn(BeIM)OAc]|CTAB**. The $^{15}$N NMR signal at -187.5 ppm in **BeIM-MIF-30** would indicate the proximity of CTAB and hence a similar chemical environment of [BeIM$^-$] as in the CTAB-facing layers in **BeIM-MIF**.

The $^{13}$C NMR splitting pattern of [BeIM$^-$] is different from that observed in the [Zn(BeIM)R] (R = OAc, Pro, Buto) class of compounds, which indicates different chemical environments through the arrangement of different secondary building blocks. The assignments of the carbon signals are summarized in Table 8.2.

**Table 8.2** Experimental and literature values of $^{13}$C NMR chemical shifts (in ppm) for **BeIM-MIF-30**, **[Zn(BeIM)OAc]**, BeIM(H), ZIF-7, HOAc and $Zn(OAc)_2 \cdot 2H_2O$.

| $^{13}$C MAS NMR | $CH_3\delta CO_2$ | $\delta CH_3CO_2$ | δC2 | δC4,7 | δC5,6 | δC8,9 |
|---|---|---|---|---|---|---|
| **BeIM-MIF-30** | 178.2 | 22.5 | 151.4 | 114.7 | 121.6; 123.2 | 140.8 |
| BeIM(H) | | | 141.7 | 118.1;112.5 | 122.4;120.9 | 134.9 |
| HOAc* | 178.1 | 20.8 | | | | |
| $Zn(OAc)_2$ $2H_2O$ | 183.7 | 19.3 | | | | |

* measured in $CDCl_3$

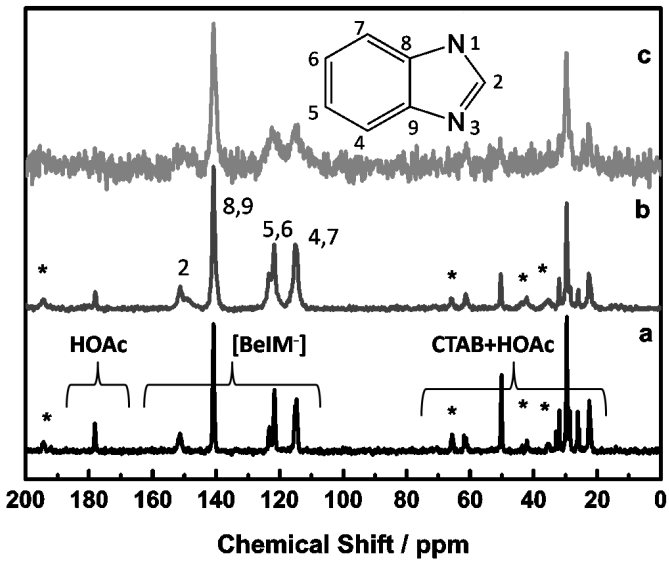


**Figure 8.3** Solid-state $^{13}C$ CP-MAS NMR spectra of **BeIM-MIF-30**: a) unwashed, b) boiled in EtOH for 2 h and c) 4 h, respectively. Signals marked with an asterisk are spinning-side bands.

For acetate two signals are visible at 178.2 ppm and 22.5 ppm, similar to protonated HOAc (178.1 ppm, 20.8 ppm) and different from deprotonated [$OAc^-$] (183.7 ppm, 19.3 ppm for $Zn(OAc)_2$). The protonated HOAc in **BeIM-MIF-30** is either a crucial part of the structure or an impurity, which can be washed away with organic solvents.Therefore **BeIM-MIF-30** was treated with different solvents at RT like $CHCl_3$ or EtOH and the$^{13}C$ NMR spectra indicate that **BeIM-MIF-30**still contains HOAc.

**Table 8.3** Experimental $^{15}N$ CP-MAS NMR chemical shifts (in ppm) of **BeIM-MIF**, **BeIM-MIF-30**, **[Zn(BeIM)OAc]**, BeIM(H), and ZIF-7.

| $^{15}N$ NMR / ppm | $\delta N_1$ |
|---|---|
| **BeIM-MIF-30** | -187.5 |
| **BeIM-MIF** | -194.3; 187.2 |
| **[Zn(BeIM)OAc]** | -194.4 |
| BeIM(H) | -145.2 |
| ZIF-7 | -192.4 |

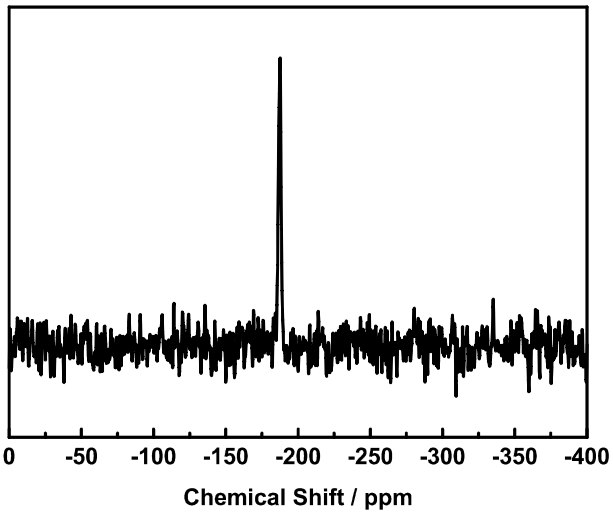


**Figure 8.4** Solid-state $^{15}N$ CP-MAS NMR spectrum of **BeIM-MIF-30**.

Other experiments were undertaken where **BeIM-MIF-30** is boiled in EtOH. $^{13}C$ CP-MAS NMR measurements of the boiled products show that the supposed impurity of HOAc can hardly be washed away. At the same time, XRD measurements suggest that the mesostructure of **BeIM-MIF-30** starts to decompose (Figure 8.1b). Figure 8.3b indicates that the sample still contains HOAc after reflux for 2 h in EtOH, no HOAc can be observed. However, the quality of the network crystallinity suffers under these conditions (Figure 8.1b+c) compared to unwashed **BeIM-MIF-30** (Figure 8.1a). All these experiments portend that HOAc is an integral part of the structure. In **[Zn(BeIM)OAc]** anionic [$OAc^-$] is twofold coordinated, thereby forming one-dimensional $Zn(OAc)_{2/2}$-chains. In **MIF-1**, **MIF-2** and **MIF-3**, the coordination polymer substructure is likely composed of $Zn(IM)_{2/2}$-chains in which the termini of the [$Zn^{2+}$] tetrahedrons are occupied by [$Br^-$] ions.[166] This finding could be a hint that in **BeIM-MIF-30** the [$Br^-$] ions are substituted by protonated [HOAc]-groups. Some examples for similar structures can be found in the literature: $[Zn(HIM)_2(oda)]_n$ (oda=oxydiacetate, IM = imidazole) consists of Zn(oda) chains, in which the $Zn^{2+}$ tetrahedrons are terminated by protonated imidazole units.[255] In $[Zn(IM)_6](HB)_2$the zinc ion is coordinated to six imidazole ([$IM^-$]) ligands and the α-hydroxycarboxylato unit ($H_2B$ =

benzylic acids) is present as a monoanionic counterion.[256] The splitting pattern and the $^{13}C$ NMR chemical shifts of CTAB ranging from 65.6 to 22.5 ppm are known values for mesostructured systems containing CTAB.[166, 195] The signals partly overlap with the $CH_3$-signal of HOAc at 22.5 ppm.

## 8.3 Elemental analysis

With regard to the results from the solid-state $^{13}C$ CP-MAS NMR, the elemental analysis yields a ratio of $[Zn^{2+}]$ : $[BeIM^-]$ : [HOAc] : [CTAB] = 2 : 3 : 2 :1 (Table 8.4).

**Table 8.4** Elemental analysis of **BeIM-MIF-30** with formula {[$(Zn_2(BeIM)_3 \cdot HOAc_2)$]*CTAB} and $M(C_{44}H_{65}O_4N_7Zn_2Br) = 966.71\ g \cdot mol^{-1}$.

| | **N** | **C** | **H** | **Br** | **Zn** | **O** |
|---|---|---|---|---|---|---|
| 1st sample | 10.0 | 55.6 | 7.0 | 9.3 | 12.9 | 5.4 |
| 2nd sample | 9.7 | 56.2 | 6.8 | 8.1 | 13.4 | 5.8 |
| 3rd sample | 9.8 | 55.9 | 7.2 | 8.1 | 13.1 | 6.0 |
| average | 9.8 | 55.9 | 7.0 | 8.5 | 13.1 | 5.7 |
| calc. | 10.1 | 54.7 | 6.8 | 8.3 | 13.5 | 6.6 |

## 8.4 Discussion

The extraction experiments show that HOAc is a crucial part of the structure. Removal of this component by extraction leads to a collapse of the structure. From the XRD powder pattern a lamellar structure was inferred, indicated by a *00l* series with a distance of 30 Å between different layers. TEM measurements indicate a hexagonal *in plane* structure of the hybrid material consisting of Zn/BeIM/OAc (Scheme 8.2A). By assuming a fourfold coordinated $Zn^{2+}$ tetrahedron and a plane layer with a hexagonal metric consisting of Zn/BeIM/HOAc building blocks, three edges of a $[Zn^{2+}]$ tetrahedron have to be bridged with each other

*via*$[BeIM^-]_{3/2}$ (Scheme 8.2B). The fourth terminal end of the $[Zn^{2+}]$ tetrahedron is occupied with an $[HOAc]_{1/1}$ unit. $CTA^+Br^-$ is not charged and may be sandwiched between the hybrid coordination polymer. This model, however, describes the system deficiently as it creates an excess of positively charged $Zn^{2+}$ units. By using an elemental composition of {$[Zn_2(BeIM)_3OAc]$*HOAc*CTAB}, the model is neutrally charged, but the deprotonated acetate signal is not observed by solid-state $^{13}C$ CP-MAS NMR.

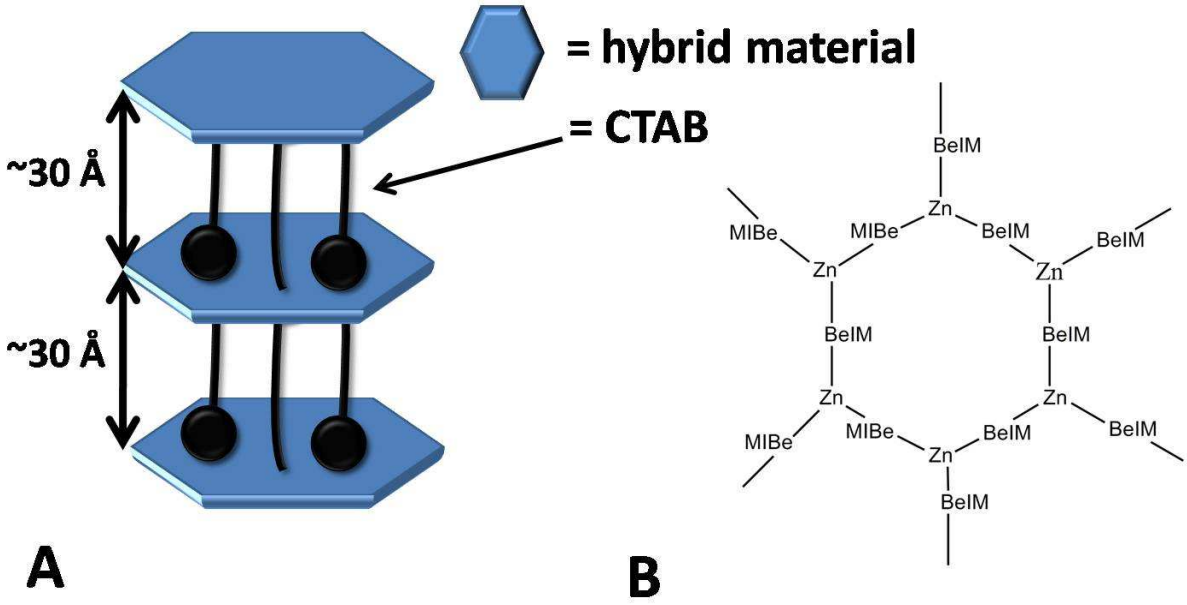


**Scheme 8.2** A) Possible structure model of **BeIM-MIF-30** with a hexagonal *inplane* ordering of the hybrid material. (B) "Cleavage" of a possible molecular assembly of a hexagonal basal layer consisting of Zn/BeIM/OAc. The terminal (H)OAc group of the $Zn^{2+}$ tetrahedrons was omitted for reasons of clarity.

# 9 Functionalization of poly[$\mu_2$-acetato-$\mu_2$-benzimidazolato zinc(II)]

In this chapter different functionalized benzimidazole derivates were used to install characteristic groups on the poly[$\mu_2$-acetato-$\mu_2$-benzimidazolato zinc(II)] coordination polymer skeleton, which can be used in further reactions as starting point for postsynthetic modifications by covalent bonding to the layered coordination polymer and, hence, also to **BeIM-MIF**. For layered oxides or perovskites, which do not contain linkers with accessible functional groups on the network skeleton, the intrinsic properties of the network are the essential tool towards applications. Post-synthetic modifications (PSM) by covalent reactions (see Introduction), as they are known from MOFs, are not possible in these systems. In MOF chemistry PSM reactions influence the physical and chemical properties of a material and therefore open up another dimension of structural possibilities and applications. Along these lines, the synthesis of different prefunctionalized **[Zn(XBeIM)OAc]** (X = Br, $NH_2$, $N_3$) materials results in a plethora of possible PSM reactions on the layered compounds derived thereof.

## 9.1 2-Chloromethylbenzimidazole (ClMe-BeIM) and 5-Bromo-1H-benzimidazole (BrBeIM)

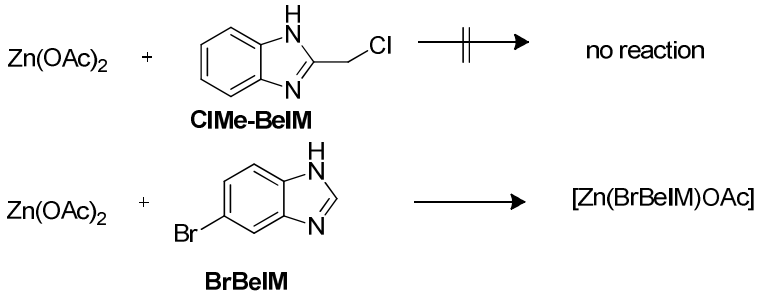


**Scheme 9.1** Synthesis attempts with functionalized benzimidazole ligands.

Firstly, the ligand 2-chloromethylbenzimidazole (**ClMe-BeIM)** (Scheme 9.1) was used under microemulsion conditions (*n*-heptane/1-hexanol), but no reaction was noted. Even when the

solvent was removed by rotary evaporation to increase the concentration, no reaction could be observed. The functionalization at the imidazole ring probably leads to a sterical hindrance, such that the $Zn^{2+}$ cannot coordinate with the two nitrogen atoms of BeIM.

On the contrary, the benzene rings of [$BeIM^-$] in the structure of **[Zn(BeIM)OAc]** are orientated parallel to the stacking direction *a* of different sheets. Therefore, it was expected that functionalization at the benzene ring as opposed to the imidazole ring would not lead to a significant sterical hindrance and a product can be isolated. Furthermore, the stacking parameter is expected to increase with the introduced functionalization.

### 9.1.1 X-Ray Powder Diffraction

Further work was done in the system Zn/BrBeIM/OAc (product named **[Zn(BrBeIM)OAc]**) by replacing benzimidazole with 5-bromo-1H-benzimidazole (BrBeIM). The XRD powder pattern of the isolated white powder is shown in Figure 9.1. The metric parameters $P2_1/c$, $a$ = 12.13, $b$ = 9.62, $c$ = 8.29 Å, $\beta$ = 94.78 were obtained by indexing of the **[Zn(BrBeIM)OAc]** phase and confirmed by TEM measurements; they are very similar to those obtained for the unfunctionalized phase. The Pawley fit shows that this phase contains impurities. The sample was not washed with EtOH.

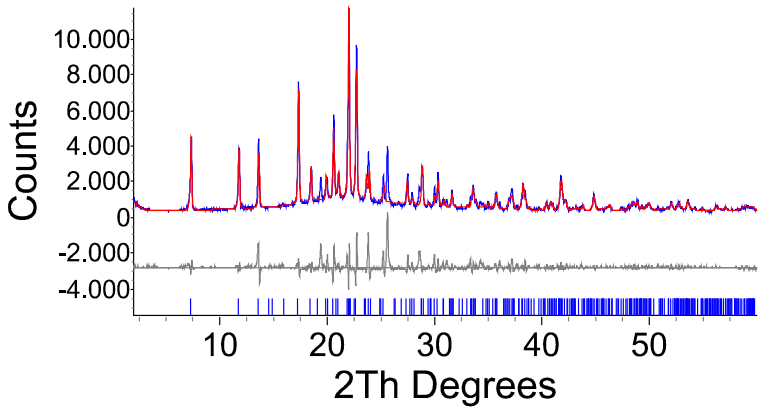


**Figure 9.1** Pawley Fit on powder XRD data of **[Zn(BrBeIM)OAc]**, yielding the space group and lattice parameters $P2_1/c$, $a$ = 12.13, $b$ = 9.62, $c$ = 8.29 Å, $\beta$ = 94.78, GoF= 4.804.

### 9.1.2 Solid-state NMR Spectroscopy

The solid-state $^{13}$C CP-MAS NMR spectra of **[Zn(BrBeIM)OAc]** and protonated BrBeIM(H) are shown in Figure 59 (Table 25).

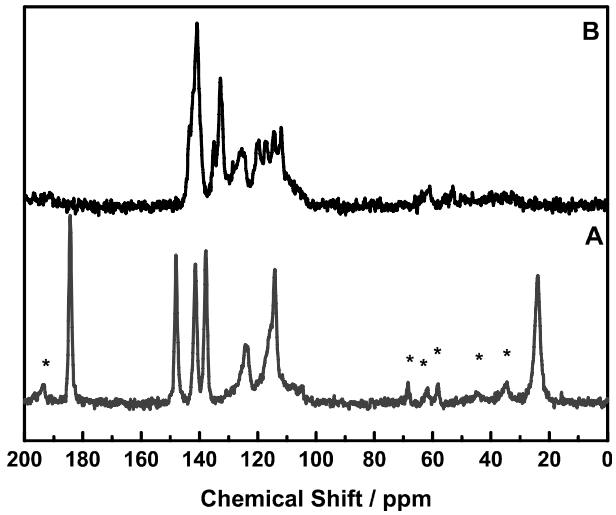


**Figure 9.2** Solid-state $^{13}$C CP-MAS NMR spectra of A) **[Zn(BrBeIM)OAc]** and B) BrBeIM(H). Signals marked with an asterisk are spinning-side bands.

These spectra reveal the signals of anionic [$OAc^-$] at 184.4/23.8 ppm (HOAc: 178.1/20.8 ppm) and the signals of BrBeIM. In comparison to protonated BrBeIM(H) all signals in Figure 9.2A are shifted to lower field which indicates that the spectra do not contain the starting materials, but rather correspond to a conversion of the starting materials. Especial-

ly the shift to lower field of the C2 signal from 140.9 ppm (for BrBeIM(H)) to 148.1 ppm (for **[Zn(BrBeIM)OAc]**) indicates the anionic character of the functionalized ligand. The deprotonated state of BeIM is confirmed by the solid-state $^{15}$N CP-MAS NMR spectrum of **[Zn(BrBeIM)OAc]**, which only exhibits a single signal at -191.3 ppm, while protonated BeIM(H) shows signals at -145.2 ppm and -223.5 ppm (Table 9.2). Since similar shifts were expected for proton bearing BrBeIM(H) in the solid-state$^{15}$N CP-MAS NMR, no $^{15}$N measurement for BrBeIM(H) was performed. The C2 signal from $^{13}$C NMR as well as the N1/N3 signals from $^{15}$N NMR, respectively, are in the range of known deprotonated [BeIM$^-$] compounds (Table 9.1+26).

**Table 9.1** Experimental and literature $^{13}$C NMR chemical shifts (in ppm) of **[Zn(BrBeIM)OAc]**, BrBeIM(H), ZIF-7, HOAc and $Zn(OAc)_2$ $2H_2O$.

| $^{13}$C NMR | $CH_3$ $\delta CO_2$ | $\delta CH_3$ $CO_2$ | $\delta$C2 | $\delta$C9 | $\delta$C8 | $\delta$C5 | $\delta$C4 | $\delta$C7 | $\delta$C6 |
|---|---|---|---|---|---|---|---|---|---|
| **[Zn(BrBeIM)OAc]** | 184.4 | 24.0 | 148.1 | 141.4 | 137.3 | 124.3[1] | 124.3[1] | 114.2[1] | 114.2[1] |
| BrBeIM(H) | | | 140.9 | 135.1 | 132.8 | 125.6 | 119.7 | 117.3 | 114.5 |
| BeIM(H) | | | 141.5 | 137.9 | 137.9 | 122.9 | 115.4 | 115.4 | 122.9 |
| HOAc* | 178.1 | 20.8 | | | | | | | |
| $Zn(OAc)_2$ $2H_2O$ | 183.7 | 19.32 | | | | | | | |

*measured in $CDCl_3$; [1]very broad peaks.

**Table 9.2** Experimental solid-state $^{15}$N CP-MAS NMR chemical shifts (in ppm) of **BeIM-MIF, [Zn(BeIM)OAc]**, BeIM(H), and ZIF-7.

| $^{15}$N NMR / ppm | $\delta N_1$ |
|---|---|
| **[Zn(BrBeIM)OAc]** | -191.3 |
| **BeIM-MIF** | -194.3; -187.2 |
| **[Zn(BeIM)OAc]** | -194.4 |
| BeIM(H) | -145.2 |
| ZIF-7 | -192.4 |

### 9.1.3 Elemental analysis

The molar composition (EA+ICP) of **[Zn(BrBeIM)OAc]** was determined to be $[Zn^{2+}] : [BrBeIM^{-}] : [OAc^{-}] = 1 : 1 : 1$ (Table. 9.3). This is consistent with the related compounds [Zn(BeIM)R] (R = OAc, Pro, Buto).

**Table 9.3** Elemental analysis of **[Zn(BrBeIM)(OAc)]** with formula $M(C_9H_7O_2N_2ZnBr) = 320.45 g\ mol^{-1}$.

| | **Zn** | **N** | **C** | **H** | **Br** | **O** |
|---|---|---|---|---|---|---|
| 1st sample | 20.42 | 8.74 | 33.68 | 2.39 | 24.77 | 10.00 |
| 2nd sample | 20.88 | 8.73 | 33.66 | 2.37 | 24.64 | 9.72 |
| average | 20.65 | 8.74 | 33.67 | 2.38 | 24.71 | 9.86 |
| calc. | 20.40 | 8.74 | 33.73 | 2.20 | 24.93 | 9.99 |

## 9.2 5-Aminobenzimidazole($NH_2$BeIM)

The ligand 5-aminobenzimidazole ($NH_2$BeIM(H)) was synthesized by reduction of 5-nitrobenzimidazole over $Pd/H_2$ (Scheme 9.2).[257] The integrals and the number of different protons/different carbon atoms in the $^1H/^{13}C$ NMR spectra fit to $NH_2$BeIM(H). No indications of impurities were found, which was also confirmed by elemental analysis. HRMS (high resolution mass spectrometry) reveal the exact mass for $NH_2$BeIM(H) *(m/z* 133.0622 $[M+H]^+$ for $C_7H_7N_3$). However, the chemical shifts in the $^1H$ and $^{13}C$ NMR spectra of $NH_2$BeIM(H) do not correspond to known literature values.[257-258]

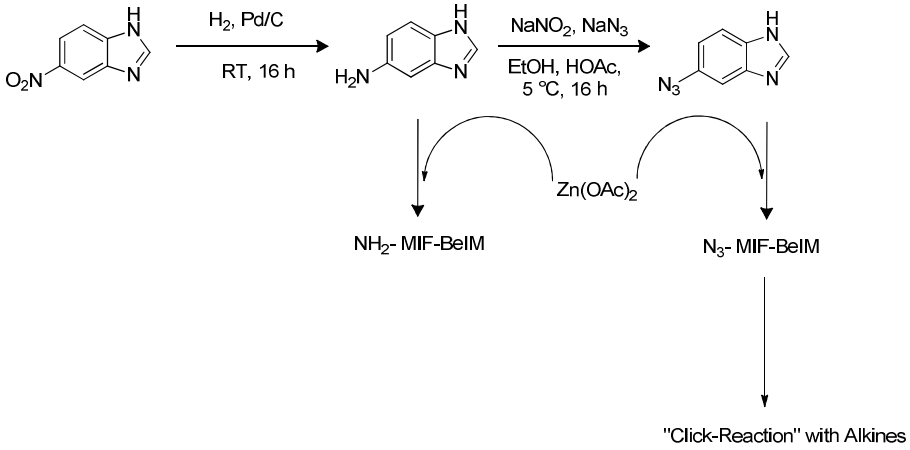


**Scheme 9.2** Reaction scheme for the synthesis of $NH_2$BeIM and $N_3$BeIM. Both BeIM(H) ligands can react with $Zn(OAc)_2$ to form the functionalized [Zn(XBeIM)OAc] (X = $N_3$, $NH_2$) systems.

## 9.3 [Zn($NH_2$BeIM)OAc]

Part of the synthesized compound was consumed for the reaction with $Zn(OAc)_2$, the other part was used for the synthesis of $N_3$BeIM(H). Synthetic work was performed under the same conditions as in the system Zn/BeIM/OAc by mixing $Zn(OAc)_2$ with $NH_2$BeIM(H) in a ratio of 1 : 1.

### 9.3.1 X-Ray Powder Diffraction

The XRD powder pattern of the isolated product, named **[Zn($NH_2$BeIM)OAc]**, is shown in Figure 9.3.

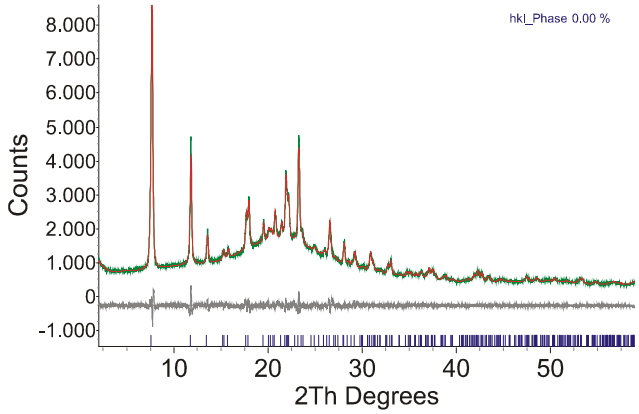


**Figure 9.3** Pawley Fit on powder XRD data of **[Zn(NH$_2$BeIM)OAc]**, yielding space group and metric parameters $P2_1/c$, $a$ = 11.69 Å, $b$ = 9.92 Å, $c$ = 8.77 Å, $\beta$ = 92.36°, GoF = 1.366.

The XRD powder pattern was indexed and refined by a Pawley fit. The space group and metric parameters were determined as $P2_1/c$, $a$ = 11.69 Å, $b$ = 9.92 Å, $c$ = 8.77 Å, $\beta$ = 92.36°. **[Zn(NH$_2$BeIM)OAc]** is isotypic to **[Zn(BeIM)OAc]**.[246]

### 9.3.2 Elemental analysis

The compositional relationship to **[Zn(BeIM)OAc]** was also confirmed by elemental analysis (EA+ICP), which reveals a ratio of [$Zn^{2+}$] : [$NH_2BeIM^-$] : [$OAc^-$] = 1 : 1 : 1 (Table 9.4).

**Table 9.4** Elemental analysis of [Zn(NH$_2$BeIM)(OAc)] with formula $M$($C_9H_{10}O_2N_3Zn$) = 257.58 g·mol$^{-1}$.

| | **Zn** | **N** | **C** | **H** | **O** |
|---|---|---|---|---|---|
| exp. | 24.1 | 16.2 | 41.8 | 3.6 | 14.3 |
| calc. | 25.3 | 16.3 | 41.9 | 3.9 | 12.4 |

### 9.3.3 Solid-state NMR Spectroscopy

The solid-state$^{13}$C CP-MAS NMR spectrum of **[Zn(NH$_2$BeIM)OAc]** is shown in Figure 9.4.

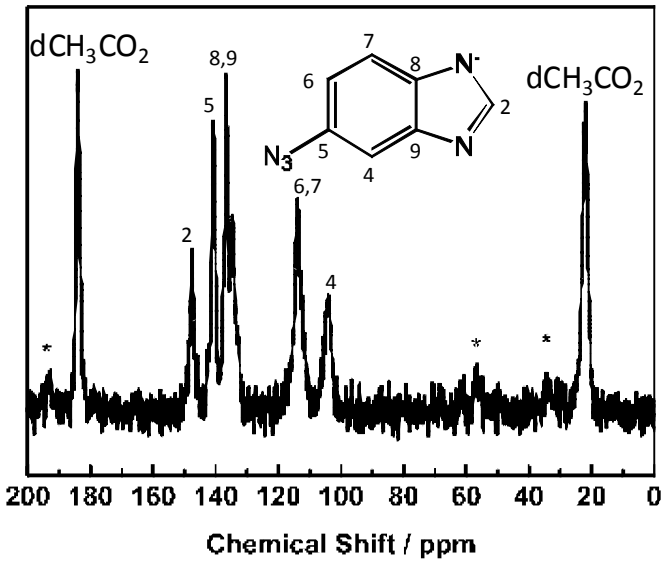


**Figure 9.4** Solid-state $^{13}C$ CP-MAS NMR spectrum of **[Zn($NH_2$BeIM)OAc]**. Signals marked with an asterisk are spinning-side bands.

The spectrum demonstrates that $NH_2$BeIM (~range 146 – 97 ppm) and anionic [$OAc^-$] at 182.6/23.4 ppm (HOAc: 178.1/20.8 ppm) are contained in this phase. Comparing the solid-state $^{13}C$ NMR spectrum with the one of $NH_2$BeIM shows that all signals are shifted, indicating that the spectrum of **[Zn($NH_2$BeIM)OAc]** does not contain starting materials. The two signals in the solid-state $^{15}N$ CP-MAS NMR spectrum at -194.5 and -196.9 ppm can be assigned to the deprotonated species of the two coordinating nitrogen atoms of the $NH_2$BeIM ligand (Figure 9.6). For **[Zn(BeIM)OAc]** only one signal was observed for the two coordinating N1/N3 atoms at -194.3 ppm. A further signal at -327.6 ppm can be assigned to the free amine group.[259-260]

The spectrum demonstrates that $NH_2$BeIM (~range 146 – 97 ppm) and anionic [$OAc^-$] at 182.6/23.4 ppm (HOAc: 178.1/20.8 ppm) are contained in this phase. Comparing the solid-state $^{13}C$ NMR spectrum with the one of $NH_2$BeIM shows that all signals are shifted, indicating that the spectrum of **[Zn($NH_2$BeIM)OAc]** does not contain starting materials. The two signals in the solid-state $^{15}N$ NMR spectrum at -194.5 and -196.9 ppm can be assigned to the deprotonated species of the two coordinating nitrogen atoms of the $NH_2$BeIM ligand

(Figure 9.6). For **[Zn(BeIM)OAc]** only one signal was observed for the two coordinating N1/N3 atoms at -194.3 ppm. A further signal at -327.6 ppm can be assigned to the free amine group.[259-260]

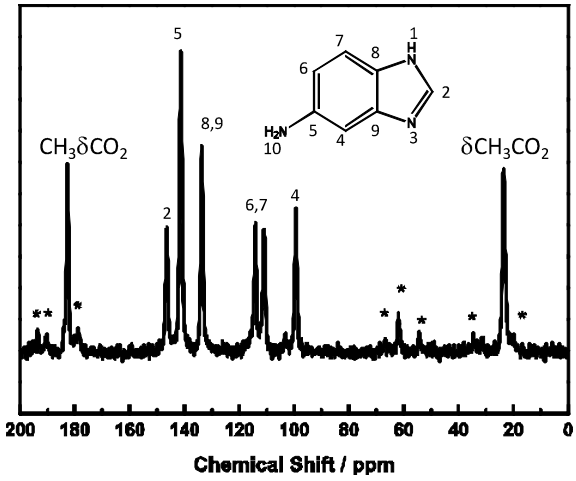


**Figure 9.5** Solid-state $^{13}C$ CP-MAS NMR spectrum of **[Zn($NH_2$BeIM)OAc]**. Signals marked with an asterisk are spinning-side bands.

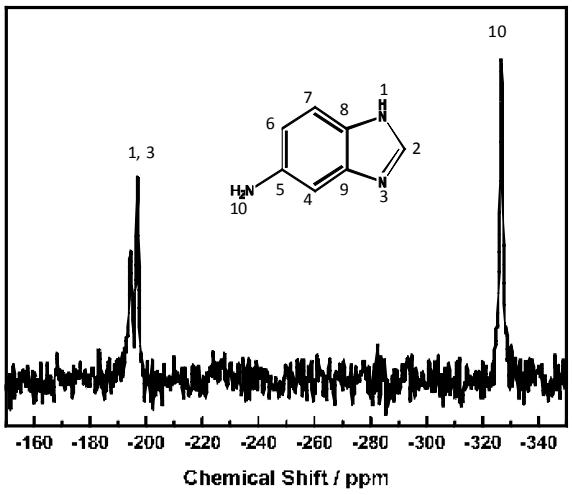


**Figure 9.6** Solid-state $^{15}N$ CP-MAS NMR spectra of **[Zn($NH_2$BeIM)OAc]**.

### 9.3.4 Conclusion

The solid-state $^{13}C/^{15}N$ CP-MAS NMR spectra, the XRD powder pattern and the elemental analysis results clearly indicate that **[Zn($NH_2$BeIM)OAc]** is quantitatively functionalized

with an amino group at the benzene ring and that the spectra are distinct from the unfunctionalized BeIM compound. If this was not the case, the splitting patterns of both BeIM species (functionalized and unfunctionalized) would be visible in the $^{13}C$ NMR spectrum of Figure 9.5.

## 9.4 5-Azidobenzimidazole ($N_3$BeIM(H))

The ligand 5-azidobenzimidazole ($N_3$BeIM(H)) was synthesized by a modified Sandmeyer reaction.[261] Amino-benzimidazole quickly reacts with sodium nitrite ($NaNO_2$) to form an aryl diazonium salt, which decomposes in the presence of sodium azide ($NaN_3$) to form the desired azide substituted benzimidazole.

Although the observed nitrogen content shows a significant deviation from the theoretical content (39.5 wt%, calc. 44.0 wt%), $^{13}C$ and $^{1}H$ NMR spectra indicate the absence of impurities of unsubstituted BeIM, which would be perceptible as a superposition of both compounds in the $^{13}C/^{1}H$ NMR spectra. Furthermore, the carbon/hydrogen weight percent (C: 52.5; H: 3.3) is in agreement with the theoretical values (C: 52.8; H: 3.2). The exact mass peak for $N_3$BeIM(H) is observed by HRMS (ESI, *m/z* 160.0617 $[M+H]^+$for $C_7H_5N_5$).

## 9.5 [Zn($N_3$BeIM)OAc]

### 9.5.1 X-Ray Powder Diffraction

The XRD powder pattern of the conversion of $N_3$BeIM and $Zn(OAc)_2$ in 1-hexanol/*n*-heptane to**[Zn($N_3$BeIM)OAc]** is shown in Figure 9.7. The low crystallinity can be explained by the reaction conditions. The synthesis was carried out at room temperature. Similar systems with **X**BeIM (X = H, $NH_2$, Br) were refluxed overnight at 100 °C. The cell parameters were ex-

tracted by a indexing ($P2_1/c$, $a$ = 12.26 Å, $b$ = 9.60 Å, $c$ = 8.73 Å, $\beta$ = 93.75°) and are isotypic to the coordination polymer **[Zn(BeIM)OAc]**.[246]

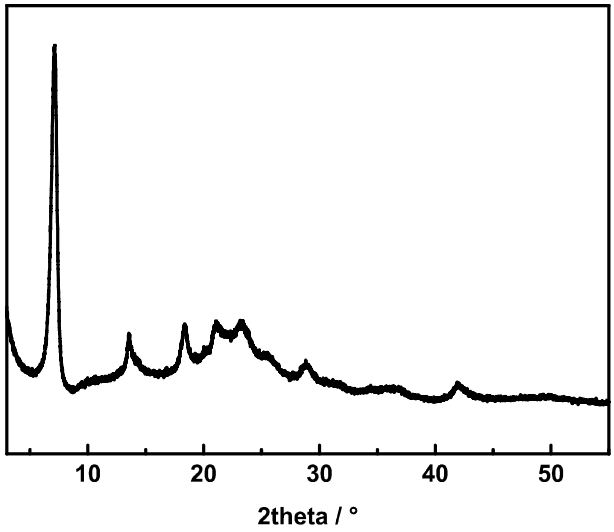


**Figure 9.7** XRD powder pattern of**[Zn($N_3$BeIM)OAc]**. A reliable Pawley Fit on the XRD data was not possible due to insufficient crystallinity of the material.

### 9.5.2 Elemental analysis

Similar to **[Zn($NH_2$BeIM)OAc]** the use of $N_3$BeIM(H) results in a material which is isotypic with **[Zn(BeIM)OAc]**. This is reinforced by elemental analysis (EA+ICP) which reveals a ratio of $[Zn^{2+}] : [N_3BeIM^- ] : [OAc^-] = 1 : 1 : 1$ (Table 9.5).

**Table 9.5** Elemental analysis of **[Zn($N_3$BeIM)(OAc)]** with formula $M(C_9H_7O_2N_5Zn) = 282.57 g \cdot mol^{-1}$.

| | **Zn** | **N** | **C** | **H** | **O** |
|---|---|---|---|---|---|
| exp. | 22.6 | 23.0 | 38.3 | 2.8 | 13.3 |
| calc. | 23.1 | 24.7 | 38.3 | 2.5 | 11.3 |

### 9.5.3 Solid-state NMR Spectroscopy

The solid-state $^{13}C$ CP-MAS NMR spectrum of **[Zn($N_3$BeIM)OAc]** is shown in Figure 9.8.

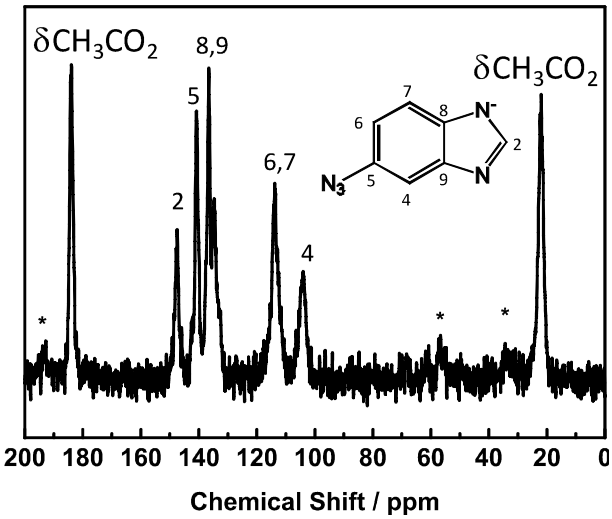


**Figure 9.8** Solid-state $^{13}C$ CP-MAS NMR spectrum of **[Zn($N_3$BeIM)OAc]**.

It clearly shows the presence of $N_3$BeIM (~range of 150 to 100 ppm) and anionic [$OAc^-$] at 183.9/22.0 ppm (HOAc: 178.1/20.8 ppm). In comparison to protonated $N_3$BeIM(H) all signals are shifted, which is a sign that the spectrum of **[Zn($N_3$BeIM)OAc]** does not contain the protonated ligand. In comparison to the proton bearing ligand the signal of C2 at 142.8 ppm is shifted to 147.5 ppm, which was observed for several anionic BeIM systems. The anionic character of [$N_3$BeIM$^-$] is also confirmed by the solid-state$^{15}N$ CP-MAS NMR spectrum. The signal at -193.5 ppm can be assigned to the deprotonated species of the two nitrogen atoms of the $N_3$BeIM ligand, which is in the range of known anionic BeIM compounds (Figure 9.9), as protonated BeIM shows signals at -145.2 ppm and-223.5 ppm. Further signals at -136.1 ppm (N2),-146.9 ppm (N4) and -290.4 ppm (N3) can be assigned to the azide group.[259-260]

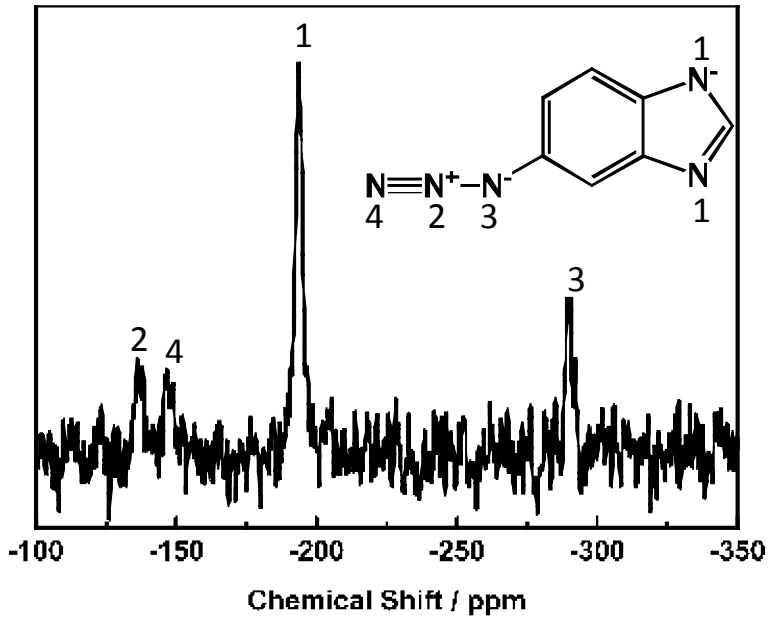


**Figure 9.9** Solid-state $^{15}$N CP-MAS NMR spectrum of **[Zn($N_3$BeIM)OAc].**

### 9.5.4 IR-spectroscopy

IR measurements are in agreement with the solid-state $^{15}$N CP-MAS NMR results (Figure 9.10) and show the presence of the azide moiety in the hybrid compound through characteristic vibrations at 2113 cm$^{-1}$($NaN_3$: 2097 cm$^{-1}$; $N_3$BeIM: 2106/2079 cm$^{-1}$). Furthermore, characteristic $N_3$BeIM and OAc ($\nu$(C=O)-stretching at 1534 cm$^{-1}$/1475 cm$^{-1}$) deformation and wagging modes are visible in the fingerprint region. In line with the NMR measurements, the absence of broad $\nu$(OH) and $\nu$(NH) stretching modes assignable to hydrogen-bonded proton bearing acetic acid and $N_3$BeIM above 1800 cm$^{-1}$again indicates complete deprotonation of $N_3$BeIM and OAc moieties.[164]

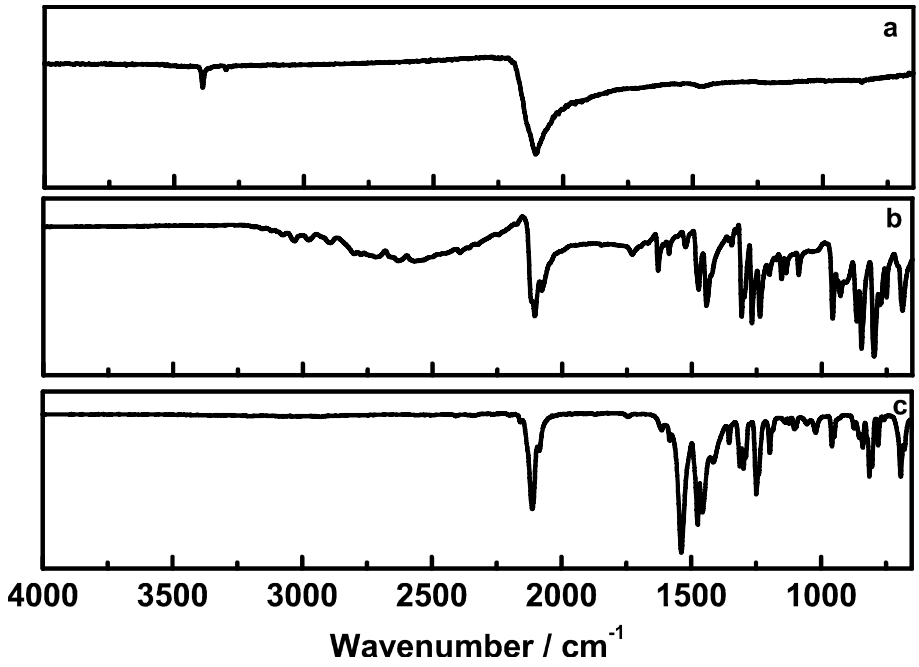


**Figure 9.10** IR-Spectra of a) $NaN_3$, b) $N_3$BeIM(H), c)**[Zn($N_3$BeIM)OAc]**.

### 9.5.5 Conclusion

The solid-state $^{13}C/^{15}N$ CP-MAS NMR spectra, the XRD powder pattern, the IR spectrum and the elemental analysis results clearly indicate that **[Zn($N_3$BeIM)OAc]** is quantitatively functionalized with the azide group and the $^{13}C/^{15}N$ spectra show the absence of the unfunctionalized BeIM compound. In the latter case the splitting patterns of functionalized and unfunctionalized BeIM compounds would be visible in the solid-state $^{13}C/^{15}N$ CP-MAS NMR spectra in Figures 9.8 and 9.9.

## 9.6 Outlook

Investigations on the reactions of $Zn(OAc)_2$ with different functionalized benzimidazole linkers were carried out. All obtained materials with modified benzimidazole linkers reveal structures isotypic to the poly[$\mu_2$-acetato-$\mu_2$-benzimidazolato zinc(II)] coordination polymer.[246] In all cases the additional functional groups do not coordinate to the zinc salt.

The structure of this coordination polymer consists of interlinked Zn-$BeIM_{2/2}$-Zn and Zn-$OAc_{2/2}$-Zn chains, which form a flat periodic backbone (Figure 9.11). The repeat distance of the functional groups within the individual layers corresponds to the lattice parameters along the benzimidazole chains ($b$~ 10 Å) and the acetate chains ($c$~ 9 Å) of **[Zn(XBeIM)OAc]**, respectively. PSM reactions can be carried out on this molecularly ordered backbone, giving rise to a high density of functional groups. **[Zn(XBeIM)OAc]** (**X**= $N_3$) can therefore be considered as a functionalized scaffold with atomic periodicity. Recently, the Cheetham group discussed several electronic and mechanical properties with regard to two-dimensional hybrid materials.[238-244] If functionalized **[Zn(XBeIM)OAc]** had semiconducting characteristics, nanoscale light harvesting materials could be constructed: For example, with the aim of click reactions modified chlorophyll molecules or dyes could be fixed on the layers. These organic dyes are vital for photosynthesis, which allows plants to absorb energy from light (Fig. 9.11).

In the structure of **[Zn(BeIM)OAc]** the sheets are connected by weak Van der Waals interactions. On an azido-functionalized matrix, a covalent crosslinking of different sheets could be achieved by the choice of polytopic short alkine molecules. By using longer or shorter linkers the interlayer distance should be tunable. Similar pore systems could be established by pushing different layers apart by suitable ligands (Figure 9.11, middle).

By clicking with long chain polymers terminated at the end with alkine groups, this action can be regarded like “knotting a wig”. Similar systems exist in nature for example on the foot of a gecko. Due to adhesion forces the gecko can climb rapidly upon smooth vertical surfaces. Recently, researchers found the reason for this phenomenon.[262] On the sole of its foot the gecko has tiny hairs which have morphologically hierarchical micro- and nano-structures. The development of a bottom-up method for gecko feet-type materials – yet on a much smaller

length scale – should be possible based on the functionalized poly[$\mu_2$-acetato-$\mu_2$-benzimidazolato zinc(II)] coordination polymer (Figure 9.11, left).

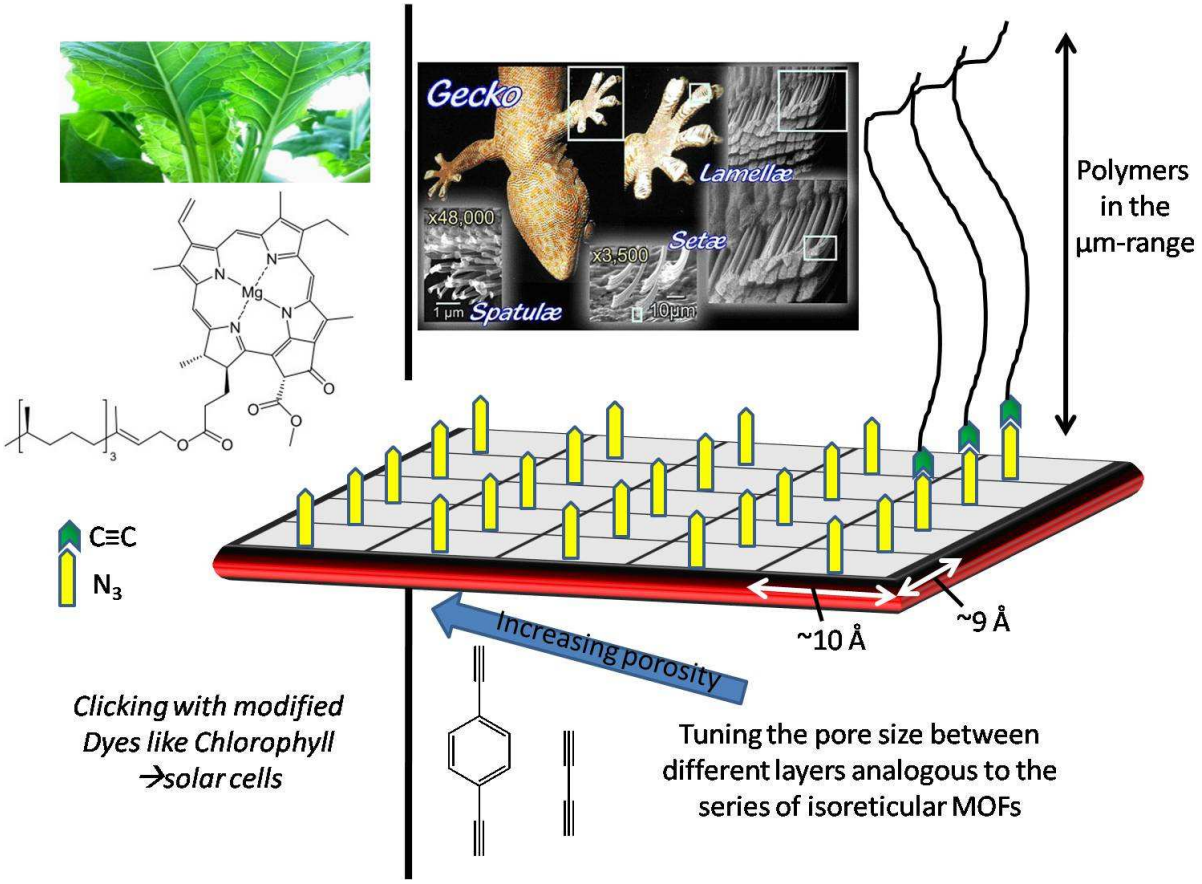


**Figure 9.11** Possible applications of the pre-functionalized material **[Zn(XBeIM)OAc]**.[263,264]

## 9.7 Experimental Section

### 9.7.1 Synthesis of [Zn(BrBeIM)OAc]

0.197 g BrBeIM (1.0 mmol) and 0.219 g $Zn(OAc)_2 \cdot 2H_2O$ (1.0 mmol) were thoroughly grinded and filled in a dried Duran glass tube ($ø_{ext.}$ = 10 mm, $ø_{int.}$ = 7 mm). The tube was evacuated, sealed under argon atmosphere at a length of 12 cm and placed in an inclined tube furnace. The oven was heated with a rate of 60 °C $h^{-1}$to 180 °C, held at this temperature for

10 h, cooled to 105 °C with a rate of 1 °C $h^{-1}$ and cooled to room temperature with 60 °C $h^{-1}$. The colorless product was washed with ethanol and dried overnight at room temperature.

### 9.7.2 Synthesis of $NH_2$BeIM(H)

In a three neck flask under hydrogen atmosphere (~2 L), a solution of 5-nitrobenzimidazole ($M_w$= 163.13 $gmol^{-1}$, 1.63 g, 0.01 mol) in ethanol (70 mL) was stirred over a palladium on carbon catalyst (5%wt Pd, 0.5 g) overnight. The progress of the reaction was controlled with thin layer chromatography. The suspension was filtered over Celite® and the filtrate was washed with ethanol. The solvent was removed with a rotary evaporator under reduced pressure. The organic residue, solved again in ethyl acetate, was washed with an aqueous $NaHCO_3$and dried over $Na_2SO_4$. After filtration and the removal of the solvent, the product was dried in an oven (60 °C) overnight.

**$^1$H NMR** (400 MHz, $d_6$-DMSO) δ) 8.29 (s, 1H), 7.50 (d, 1H), 6.78 (d, 1H), 6.57 (dd, 1H).

**$^{13}$C NMR** (100 MHz, $d_6$-DMSO) δ) 153.3($C_q$), 146.7, 143.8($C_q$), 138.6($C_q$), 118.9, 112.1, 93.5.

**HRMS** for $C_7H_7N_3$ ($DEI^+$, *m/z*) 133.0622 $[M+H]^+$, calc: 133.0640.

**Table 9.6** Elemental analysis of $NH_2$BeIM(H) with formula $M(C_7H_7N_3)$ = 133.15 g·$mol^{-1}$.

| | N | C | H |
|---|---|---|---|
| exp. | 31.6 | 63.1 | 5.3 |
| calc. | 31.6 | 63.1 | 5.3 |

### 9.7.3 Synthesis of [Zn($NH_2$BeIM)OAc]

In a 100 mL flask 2.7 mL of a 0.6 M $NH_2$BeIM solution (in 1-hexanol) was mixed under stirring with 5.4 mL 1.2 M $Zn(OAc)_2$ solution (in water) in a solvent mixture of *n*-heptane/1-hexanol (9 : 1, 100 mL) and refluxed at 100 °C overnight. The product was isolated by centrifugation (5 min/10000 rpm) and dried overnight in an oven (40 °C).

### 9.7.4 Synthesis of $N_3$BeIM(H)

A solution of $NaNO_2$ (51.7 mg) in water (1.5 mL) was mixed with a solution of $NH_2$BeIM (100 mg) in 4 mL acetic acid at 278 K. The reaction was cooled in an ice bath to 273 K and stirred for 30 min. A solution of $NaN_3$ (73.1 mg) in water (2 mL) was added and the mixture was stirred overnight. 100 mL ethyl acetate was added and the organic phase was washed three times with an aqueous saturated $K_2CO_3$ solution and dried over $Na_2SO_4$. After filtration the excess solvent was removed by a rotary evaporator.

**$^1$H NMR** (400 MHz, $CD_3OD$) δ) 8.04 (s, 1H), 7.58 (d, 1H), 7.24 (d, 1H), 6.96 (dd, 1H).

**$^{13}$CNMR** (100 MHz, $CD_3OD$) δ) 142.8, 137.0 ($C_q$), 138.3 ($C_q$), 136.2 ($C_q$), 117.3, 115.5, 105.6.

**HRMS** for $C_7H_5N_5$ ($ESI^+$, *m/z*) 160.0617 $[M+H]^+$, calc: 160.0623 ; ($ESI^-$, *m/z*) 158.0473 $[M-H]^-$, calc: 158.0467.

**IR-Spectrum**: Figure 9.10b

**Table 9.7** Elemental analysis of $N_3$BeIM(H) with formula M($C_7H_5N_5$) =159.06 $g \cdot mol^{-1}$.

| | N | C | H |
|---|---|---|---|
| exp. | 39.5 | 52.5 | 3.3 |
| calc. | 44.0 | 52.8 | 3.2 |

### 9.7.5 Synthesis of [Zn($N_3$BeIM)OAc]

In a 100 mL flask 1.35 mL of a 0.6 M $N_3$BeIM stock solution (in 1-hexanol) was mixed with 0.75 mL of a 1.2 M $Zn(OAc)_2$ stock solution (in water) in *n*-heptane/1-hexanol (45 mL/5 mL) and stirred at room temperature overnight. The product was isolated by centrifugation (5 min/10000 rpm) and dried overnight in an oven (40 °C).

## 9.8 Supporting Information

**Table S3.** Experimental parameters for the solid-state CP-MAS $^{13}C$ and $^{15}N$ NMR measurements.

| **$^{13}C$** | Rotational frequency | Contact time [μsec] | recycle delay [sec] | scans |
|---|---|---|---|---|
| **BeIM-MIF(Pro)** | 10 | 5000 | 1 | 200 |
| **[Zn(BeIM)Pro]** | 10 | 3000 | 8 | 200 |
| **$Zn(Pro)_2$** | 10 | 5000 | 5 | 40 |
| **BeIM-MIF(Buto)** | 10 | 5000 | 4 | 100 |
| **[Zn(BeIM)Buto]** | 10 | 5000 | 4 | 100 |
| **$Zn(Buto)_2$** | 10 | 5000 | 5 | 16 |
| **[Zn(BrBeIM)OAc]** | 10 | 5000 | 16 | 492 |
| **BrBeIM(H)** | 10 | 5000 | 32 | 100 |
| **[Zn($NH_2$BeIM)OAc]** | 10 | 5000 | 8 | 200 |
| **[Zn($N_3$BeIM)OAc]** | 10 | 5000 | 1 | 512 |
| **BeIM-MIF-30** | 10 | 5000 | 2 | 204 |
| **BeIM-MIF-40** | 10 | 1000 | 1 | 28 |
| **$^{15}N$** | | | | |
| **MIF-Pro** | 10 | 5000 | 2 | 10100 |
| **BeIM-MIF-30** | 10 | 5000 | 2 | 230488 |
| **BeIM-MIF-40** | 10 | 10000 | 1 | 12136 |
| **[Zn($NH_2$BeIM)OAc]** | 10 | 5000 | 8 | 6704 |
| **[Zn($N_3$BeIM)OAc]** | 10 | 5000 | 1 | 36724 |

# 10 References


1. Cronstedt, A. F., *Akad. Handl. Stockholm* **1756,** *18*, 120.
2. Damour, A., *Ann. Mines.* **1840,** *17*, 191.
3. Eichhorn, H., *Ann. Rev. Phys. Chem.* **1858,** *105*, 126.
4. Taylor, W. H., *Zeitschrift fuer Kristallographie, Kristallgeometrie, Kristallphysik, Kristallchemie* **1930,** *74*, 1.
5. Pauling, L., *Zeitschrift fuer Kristallographie, Kristallgeometrie, Kristallphysik, Kristallchemie* **1930,** *74*, 213.
6. Barrer, R. M., *J. Chem. Soc.* **1948**, 2158-2163.
7. Barrer, R. M.; Riley, D. W., *J. Chem. Soc.* **1948**, 133-143.
8. Barrer, R. M., *J. Chem. Soc.* **1948**, 127-132.
9. http://www.iza-structure.org/databases/. Structure Commission of the International Zeolite Association.
10. Cundy, C. S.; Cox, P. A., *Chem. Rev.* **2003,** *103*, 663-702.
11. Weitkamp, J., *Solid State Ionics* **2000,** *131*, 175-188.
12. Martínez, C.; Corma, A., *Coord. Chem. Rev.* **2011,** *255*, 1558-1580.
13. Yilmaz, B.; Müller, U., *Top Catal* **2009,** *52*, 888-895.
14. P. B. Venuto, E. T. H., Jr., *Fluid Catalytic Cracking with Zeolite Catalysts*. **1979**; Vol. 1.
15. Wilson, S. T.; Lok, B. M.; Messina, C. A.; Cannan, T. R.; Flanigen, E. M., *J. Am. Chem. Soc.* **1982,** *104*, 1146-1147.
16. Cascales, C.; Gutiérrez-Puebla, E.; Iglesias, M.; Monge, M. A.; Ruíz-Valero, C., *Angew. Chem. Int. Ed.* **1999,** *38*, 2436-2439.
17. Cavellec, M.; Riou, D.; Ninclaus, C.; Grenèche, J.-M.; Férey, G., *Zeolites* **1996,** *17*, 250-260.
18. Cheetham, A. K.; Forster, P. M., *The Chemistry of Nanomaterials: Synthesis, Properties and Applications*. Weinheim, **2004**; Vol. 2.
19. Cheetham, A. K.; Forster, P. M., *The Chemistry of Nanomaterials: Synthesis,Properties and Applications*. WILEY-VCH Verlag GmbH & Co. KGaA: Weinheim, **2004.**; Vol. 2.
20. Tchernev, D. I., *Rev. Mineral. Geochem.* **2001,** *45*, 589-617.

21. Vallet-Regí, M.; Balas, F.; Colilla, M.; Manzano, M., *Solid State Sci.* **2007,** *9*, 768-776.

22. Dogliotti, G.; Malavazos, A. E.; Giacometti, S.; Solimene, U.; Fanelli, M.; Corsi, M. M.; Dozio, E., *J. Clin Biochem. Nutr.* **2012,** *50*, 195-198.

23. Platas-Iglesias, C.; Vander Elst, L.; Zhou, W.; Muller, R. N.; Geraldes, C. F. G. C.; Maschmeyer, T.; Peters, J. A., *Chem. Eur. J.* **2002,** *8*, 5121-5131.

24. Adams, C. J.; Araya, A.; Carr, S. W.; Chapple, A. P.; Franklin, K. R.; Graham, P.; Minihan, A. R.; Osinga, T. J.; Stuart, J. A., Zeolite map: The new detergent zeolite. In *Stud. Surf. Sci. Catal.*, Hakze Chon, S.-K. I.; Young Sun, U., Eds. Elsevier: **1997**; Vol. Volume 105, pp 1667-1674.

25. Coe, C. G., *Gas Separation Technology*. Elsevier: **1990**.

26. Chiku, H.; Matsui, M.; Murakami, S.; Kiyozumi, Y.; Mizukami, F.; Sakaguchi, K., *Anal. Biochem.* **2003,** *318*, 80-85.

27. Caro, J., *Micropor. Mesopor. Mater.* **2009,** *125*, 79-84.

28. Li, Y. Y.; Cunin, F.; Link, J. R.; Gao, T.; Betts, R. E.; Reiver, S. H.; Chin, V.; Bhatia, S. N.; Sailor, M. J., *Science* **2003,** *299*, 2045-2047.

29. Nijkamp, M. G.; Raaymakers, J. E. M. J.; van Dillen, A. J.; de Jong, K. P., *Appl Phys A* **2001,** *72*, 619-623.

30. Liu, C. Y.; Aika, K.-i., *J. Jpn. Pet. Inst.* **2003,** *46*, 301-307.

31. Düren, T.; Sarkisov, L.; Yaghi, O. M.; Snurr, R. Q., *Langmuir* **2004,** *20*, 2683-2689.

32. Sing, K. S. W.; Everett, D. H.; Haul, R. A. W.; Moscou, L.; Pierotti, R. A.; Rouquerol, J.; Siemeniewska, T., *Pure Appl. Chem.* **1985,** *57*, 603-619.

33. Kersting, B., http://www.uni-leipzig.de/~bkerst/MCM41.ppt.

34. Kresge, C. T.; Leonowicz, M. E.; Roth, W. J.; Vartuli, J. C.; Beck, J. S., *Nature* **1992,** *359*, 710-712.

35. Beck, J. S.; Vartuli, J. C.; Roth, W. J.; Leonowicz, M. E.; Kresge, C. T.; Schmitt, K. D.; Chu, C. T. W.; Olson, D. H.; Sheppard, E. W., *J. Am. Chem. Soc.* **1992,** *114*, 10834-10843.

36. Wan, Y.; Zhao, *Chem. Rev.* **2007,** *107*, 2821-2860.

37. Sakamoto, Y.; Kim, T.-W.; Ryoo, R.; Terasaki, O., *Angew. Chem. Int. Ed.* **2004,** *43*, 5231-5234.

38. Sakamoto, Y.; Kaneda, M.; Terasaki, O.; Zhao, D. Y.; Kim, J. M.; Stucky, G.; Shin, H. J.; Ryoo, R., *Nature* **2000,** *408*, 449-453.

39. Garcia-Bennett, A. E.; Miyasaka, K.; Terasaki, O.; Che, S., *Chem. Mater.* **2004,** *16*, 3597-3605.

40. Kaneda, M.; Tsubakiyama, T.; Carlsson, A.; Sakamoto, Y.; Ohsuna, T.; Terasaki, O.; Joo, S. H.; Ryoo, R., *J. Phys. Chem. B* **2002,** *106*, 1256-1266.

41. Yu, T.; Zhang, H.; Yan, X.; Chen, Z.; Zou, X.; Oleynikov, P.; Zhao, D., *J. Phys. Chem. B* **2006,** *110*, 21467-21472.

42. Zhao, D.; Huo, Q.; Feng, J.; Chmelka, B. F.; Stucky, G. D., *J. Am. Chem. Soc.* **1998,** *120*, 6024-6036.

43. Gomez-Vega, J. M.; Teshima, K.; Hozumi, A.; Sugimura, H.; Takai, O., *Surface and Coatings Technology* **2003,** *169–170*, 504-507.

44. Tian, B.; Liu, X.; Yu, C.; Gao, F.; Luo, Q.; Xie, S.; Tu, B.; Zhao, D., *Chem. Commun.* **2002**, 1186-1187.

45. Lang, N.; Tuel, A., *Chem. Mater.* **2004,** *16*, 1961-1966.

46. Kawi, S., *Chem. Commun.* **1998**, 1407-1408.

47. Tanev, P. T.; Pinnavaia, T. J., *Science* **1995,** *267*, 865-867.

48. Herrier, G.; Blin, J.-L.; Su, B.-L., *Langmuir* **2001,** *17*, 4422-4430.

49. Zhao, D.; Feng, J.; Huo, Q.; Melosh, N.; Fredrickson, G. H.; Chmelka, B. F.; Stucky, G. D., *Science* **1998,** *279*, 548-552.

50. Zhao, D.; Sun, J.; Li, Q.; Stucky, G. D., *Chem. Mater.* **2000,** *12*, 275-279.

51. Impéror-Clerc, M.; Davidson, P.; Davidson, A., *J. Am. Chem. Soc.* **2000,** *122*, 11925-11933.

52. Taguchi, A.; Schüth, F., *Micropor. Mesopor. Mater.* **2005,***77*, 1-45.

53. Attard, G. S.; Bartlett, P. N.; Coleman, N. R. B.; Elliott, J. M.; Owen, J. R.; Wang, J. H., *Science* **1997,** *278*, 838-840.

54. MacLachlan, M. J.; Coombs, N.; Ozin, G. A., *Nature* **1999,** *397*, 681-684.

55. Jun, Y.-S.; Hong, W. H.; Antonietti, M.; Thomas, A., *Adv. Mater.* **2009,** *21*, 4270-4274.

56. Trikalitis, P. N.; Rangan, K. K.; Bakas, T.; Kanatzidis, M. G., *Nature* **2001,** *410*, 671-675.

57. Ciesla, U.; Schacht, S.; Stucky, G. D.; Unger, K. K.; Schüth, F., *Angew. Chem. Int. Ed.* **1996,** *35*, 541-543.

58. Ryoo, R.; Joo, S. H.; Jun, S., *J. Phys. Chem. B* **1999,** *103*, 7743-7746.

59. Möller, K.; Bein, T., *Science* **2011,** *333*, 297-298.

60. Na, K.; Jo, C.; Kim, J.; Cho, K.; Jung, J.; Seo, Y.; Messinger, R. J.; Chmelka, B. F.; Ryoo, R., *Science* **2011,** *333*, 328-332.

61. Yaghi, O. M.; Li, G.; Li, H., *Nature* **1995,** *378*, 703-706.

62. Tomic, E. A., *J. Apppl. Polym. Sci.* **1965,** *9*, 3745-3752.

63. Yaghi, O. M.; O'Keeffe, M.; Ockwig, N. W.; Chae, H. K.; Eddaoudi, M.; Kim, J., *Nature* **2003,** *423*, 705-714.

64. O'Keeffe, M.; Peskov, M. A.; Ramsden, S. J.; Yaghi, O. M., *Acc. Chem. Res.* **2008,** *41*, 1782-1789.

65. Tranchemontagne, D. J.; Ni, Z.; O'Keeffe, M.; Yaghi, O. M., *Angew. Chem. Int. Ed.* **2008,** *47*, 5136-5147.

66. O'Keeffe, M., *Chem. Soc. Rev.* **2009,** *38*, 1215-1217.

67. O'Keeffe, M.; Eddaoudi, M.; Li, H.; Reineke, T.; Yaghi, O. M., *J. Solid State Chem.* **2000,** *152*, 3-20.

68. Tranchemontagne, D. J.; Mendoza-Cortes, J. L.; O'Keeffe, M.; Yaghi, O. M., *Chem. Soc. Rev.* **2009,** *38*, 1257-1283.

69. Eddaoudi, M.; Kim, J.; Rosi, N.; Vodak, D.; Wachter, J.; O'Keeffe, M.; Yaghi, O. M., *Science* **2002,** *295*, 469-472.

70. Batten, S. R.; Robson, R., *Angew. Chem. Int. Ed.* **1998,** *37*, 1460-1494.

71. Rowsell, J. L. C.; Yaghi, O. M., *Angew. Chem. Int. Ed.* **2005,** *44*, 4670-4679.

72. Deng, H.; Grunder, S.; Cordova, K. E.; Valente, C.; Furukawa, H.; Hmadeh, M.; Gándara, F.; Whalley, A. C.; Liu, Z.; Asahina, S.; Kazumori, H.; O'Keeffe, M.; Terasaki, O.; Stoddart, J. F.; Yaghi, O. M., *Science* **2012,** *336*, 1018-1023.

73. Choi, S. B.; Furukawa, H.; Nam, H. J.; Jung, D.-Y.; Jhon, Y. H.; Walton, A.; Book, D.; O'Keeffe, M.; Yaghi, O. M.; Kim, J., *Angew. Chem. Int. Ed.* **2012,** *51*, 8791-8795.

74. Rowsell, J. L. C.; Yaghi, O. M., *Micropor. Mesopor. Mater.* **2004,** *73*, 3-14.

75. Bellarosa, L.; Calero, S.; Lopez, N., *Phys. Chem. Chem. Phys.* **2012,** *14*, 7240-7245.

76. Kitagawa, S.; Kitaura, R.; Noro, S.-i., *Angew. Chem. Int. Ed.* **2004,** *43*, 2334-2375.

77. Rao, C. N. R.; Natarajan, S.; Vaidhyanathan, R., *Angew. Chem. Int. Ed.* **2004,** *43*, 1466-1496.

78. Chen, Q.-Y.; Li, Y.; Zheng, F.-K.; Zou, W.-Q.; Wu, M.-F.; Guo, G.-C.; Wu, A. Q.; Huang, J.-S., *Inorg. Chem. Commun.* **2008,** *11*, 969-971.

79. Gao, W.-Y.; Yan, W.; Cai, R.; Williams, K.; Salas, A.; Wojtas, L.; Shi, X.; Ma, S., *Chem. Commun.* **2012**, 8898-8900.

80. Valente, C.; Choi, E.; Belowich, M. E.; Doonan, C. J.; Li, Q.; Gasa, T. B.; Botros, Y. Y.; Yaghi, O. M.; Stoddart, J. F., *Chem. Commun.* **2010**, 4911-4913.

81. Smaldone, R. A.; Forgan, R. S.; Furukawa, H.; Gassensmith, J. J.; Slawin, A. M. Z.; Yaghi, O. M.; Stoddart, J. F., *Angew. Chem. Int. Ed.* **2010,** *49*, 8630-8634.

82. Zhao, Y.-L.; Liu, L.; Zhang, W.; Sue, C.-H.; Li, Q.; Miljanić, O. Š.; Yaghi, O. M.; Stoddart, J. F., *Chem. Eur. J.* **2009,** *15*, 13356-13380.

83. Mizutani, M.; Maejima, N.; Jitsukawa, K.; Masuda, H.; Einaga, H., *Inorg. Chim. Acta* **1998,** *283*, 105-110.

84. Zhang, Y.; Saha, M. K.; Bernal, I., *Cryst. Eng. Comm.* **2003,** *5*, 34-37.

85. Tranchemontagne, D. J.; Hunt, J. R.; Yaghi, O. M., *Tetrahedron* **2008,** *64*, 8553-8557.

86. Pichon, A.; James, S. L., *Cryst. Eng. Comm.* **2008,** *10*, 1839-1847.

87. Parnham, E. R.; Morris, R. E., *Acc. Chem. Res.* **2007,** *40*, 1005-1013.

88. Britt, D.; Furukawa, H.; Wang, B.; Glover, T. G.; Yaghi, O. M., *Proc. Nat. Acad. Sci.* **2009,** *106*, 20637-20640.

89. Farrusseng, D., *Metal-Organic Frameworks Applications from Catalysis to Gas Storage*. Wiley-VCH Verlag GmbH & Co. KGaA: **2011**; Vol. 1. Auflage.

90. Farrusseng, D.; Aguado, S.; Pinel, C., *Angew. Chem. Int. Ed.* **2009,** *48*, 7502-7513.

91. Lee, J.; Farha, O. K.; Roberts, J.; Scheidt, K. A.; Nguyen, S. T.; Hupp, J. T., *Chem. Soc. Rev.* **2009,** *38*, 1450-1459.

92. Corma, A.; García, H.; Llabrés i Xamena, F. X., *Chem. Rev.* **2010,** *110*, 4606-4655.

93. Huxford, R. C.; Della Rocca, J.; Lin, W., *Currr. Opin. Chem. Biol.* **2010,** *14*, 262-268.

94. Evans, O. R.; Lin, W., *Acc. Chem. Res.* **2002,** *35*, 511-522.

95. Lu, Z.-Z.; Zhang, R.; Li, Y.-Z.; Guo, Z.-J.; Zheng, H.-G., *J. Am. Chem. Soc.* **2011,** *133*, 4172-4174.

96. Férey, G.; Serre, C.; Mellot-Draznieks, C.; Millange, F.; Surblé, S.; Dutour, J.; Margiolaki, I., *Angew. Chem. Int. Ed.* **2004,** *43*, 6296-6301.

97. Férey, G.; Mellot-Draznieks, C.; Serre, C.; Millange, F.; Dutour, J.; Surblé, S.; Margiolaki, I., *Science* **2005,** *309*, 2040-2042.

98. Huang, X.-C.; Lin, Y.-Y.; Zhang, J.-P.; Chen, X.-M., *Angew. Chem. Int. Ed.* **2006,** *45*, 1557-1559.

99. Phan, A.; Doonan, C. J.; Uribe-Romo, F. J.; Knobler, C. B.; O'Keeffe, M.; Yaghi, O. M., *Acc. Chem. Res.* **2009,** *43*, 58-67.

100. Park, K. S.; Ni, Z.; Côte, A. P.; Choi, J. Y.; Huang, R.; Uribe-Romo, F. J.; Chae, H. K.; O´Keeffe, M.; Yaghi, O. M., *Proc. Nat. Acad. Sci.* **2006,** *103*, 10186-10191.

101. Banerjee, R.; Phan, A.; Wang, B.; Knobler, C.; Furukawa, H.; O'Keeffe, M.; Yaghi, O. M., *Science* **2008,** *319*, 939-943.

102. Wang, B.; Cote, A. P.; Furukawa, H.; O/'Keeffe, M.; Yaghi, O. M., *Nature* **2008,** *453*, 207-211.

103. Bux, H.; Liang, F.; Li, Y.; Cravillon, J.; Wiebcke, M.; Caro, J. r., *J. Am. Chem. Soc.* **2009,** *131*, 16000-16001.

104. Liu, Y.; Hu, E.; Khan, E. A.; Lai, Z., *J. Membr. Sci.* **2010,** *353*, 36-40.

105. Lu, G.; Hupp, J. T., *J. Am. Chem. Soc.* **2010,** *132*, 7832-7833.

106. Hinterholzinger, F. M.; Ranft, A.; Feckl, J. M.; Ruhle, B.; Bein, T.; Lotsch, B. V., *J. Mater. Chem.* **2012,** *22*, 10356-10362.

107. Liédana, N.; Galve, A.; Rubio, C.; Téllez, C.; Coronas, J., *ACS Appl. Mater. Interfaces* **2012,** *4*, 5016-5021.

108. Seo, J. S.; Whang, D.; Lee, H.; Jun, S. I.; Oh, J.; Jeon, Y. J.; Kim, K., *Nature* **2000,** *404*, 982-986.

109. Wang, Z.; Cohen, S. M., *J. Am. Chem. Soc.* **2007,** *129*, 12368-12369.

110. Cohen, S. M., *Chem. Sci.* **2010,** *1*, 32-36.

111. Wang, Z.; Cohen, S. M., *Chem. Soc. Rev.* **2009,** *38*, 1315-1329.

112. Tanabe, K. K.; Wang, Z.; Cohen, S. M., *J. Am. Chem. Soc.* **2008,** *130*, 8508-8517.

113. Britt, D.; Lee, C.; Uribe-Romo, F. J.; Furukawa, H.; Yaghi, O. M., *Inorg. Chem.* **2010,** *49*, 6387-6389.

114. Doonan, C. J.; Morris, W.; Furukawa, H.; Yaghi, O. M., *J. Am. Chem. Soc.* **2009,** *131*, 9492-9493.

115. Dugan, E.; Wang, Z.; Okamura, M.; Medina, A.; Cohen, S. M., *Chem. Commun.* **2008**, 3366-3368.

116. Wang, Z.; Cohen, S. M., *Angew. Chem. Int. Ed.* **2008,** *47*, 4699-4702.

117. Jones, S. C.; Bauer, C. A., *J. Am. Chem. Soc.* **2009,** *131*, 12516-12517.

118. Volkringer, C.; Cohen, S. M., *Angew. Chem. Int. Ed.* **2010,** *49*, 4644-4648.

119. Kim, M.; Cahill, J. F.; Prather, K. A.; Cohen, S. M., *Chem. Commun.* **2011,** *47*, 7629-7631.

120. Taylor-Pashow, K. M. L.; Rocca, J. D.; Xie, Z.; Tran, S.; Lin, W., *J. Am. Chem. Soc.* **2009,** *131*, 14261-14263.

121. Morris, W.; Doonan, C. J.; Furukawa, H.; Banerjee, R.; Yaghi, O. M., *J. Am. Chem. Soc.* **2008,** *130*, 12626-12627.

122. Bernt, S.; Guillerm, V.; Serre, C.; Stock, N., *Chem. Commun.* **2011**, 2838-2840.

123. Tanabe, K. K.; Allen, C. A.; Cohen, S. M., *Angew. Chem. Int. Ed.* **2010,** *49*, 9730-9733.

124. Modrow, A.; Zargarani, D.; Herges, R.; Stock, N., *Dalton Trans.* **2012,** *41*, 8690-8696.

125. Kolb, H. C.; Finn, M. G.; Sharpless, K. B., *Angew. Chem. Int. Ed.* **2001,** *40*, 2004-2021.

126. Binder, W. H.; Sachsenhofer, R., *Macromol. Rapid Commun.* **2007,** *28*, 15-54.

127. Wu, P.; Malkoch, M.; Hunt, J. N.; Vestberg, R.; Kaltgrad, E.; Finn, M. G.; Fokin, V. V.; Sharpless, K. B.; Hawker, C. J., *Chem. Commun.* **2005**, 5775-5777.

128. Díaz, D. D.; Rajagopal, K.; Strable, E.; Schneider, J.; Finn, M. G., *J. Am. Chem. Soc.* **2006,** *128*, 6056-6057.

129. Gupta, S. S.; Kuzelka, J.; Singh, P.; Lewis, W. G.; Manchester, M.; Finn, M. G., *Bioconjugate Chem.* **2005,** *16*, 1572-1579.

130. Dirks, A. J.; van Berkel, S. S.; Hatzakis, N. S.; Opsteen, J. A.; van Delft, F. L.; Cornelissen, J. J. L. M.; Rowan, A. E.; van Hest, J. C. M.; Rutjes, F. P. J. T.; Nolte, R. J. M., *Chem. Commun.* **2005**, 4172-4174.

131. Beatty, K. E.; Xie, F.; Wang, Q.; Tirrell, D. A., *J. Am. Chem. Soc.* **2005,** *127*, 14150-14151.

132. Link, A. J.; Tirrell, D. A., *J. Am. Chem. Soc.* **2003,** *125*, 11164-11165.

133. Goto, Y.; Sato, H.; Shinkai, S.; Sada, K., *J. Am. Chem. Soc.* **2008,** *130*, 14354-14355.

134. Savonnet, M.; Camarata, A.; Canivet, J.; Bazer-Bachi, D.; Bats, N.; Lecocq, V.; Pinel, C.; Farrusseng, D., *Dalton Trans.* **2012,** *41*, 3945-3948.

135. Gadzikwa, T.; Lu, G.; Stern, C. L.; Wilson, S. R.; Hupp, J. T.; Nguyen, S. T., *Chem. Commun.* **2008**, 5493-5495.

136. Gadzikwa, T.; Farha, O. K.; Malliakas, C. D.; Kanatzidis, M. G.; Hupp, J. T.; Nguyen, S. T., *J. Am. Chem. Soc.* **2009,** *131*, 13613-13615.

137. Jiang, H.-L.; Feng, D.; Liu, T.-F.; Li, J.-R.; Zhou, H.-C., *J. Am. Chem. Soc.* **2012,** *134*, 14690-14693.

138. Zhao, D.; Tan, S.; Yuan, D.; Lu, W.; Rezenom, Y. H.; Jiang, H.; Wang, L.-Q.; Zhou, H.-C., *Adv. Mater.* **2011,** *23*, 90-93.

139. Rieter, W. J.; Taylor, K. M. L.; An, H.; Lin, W.; Lin, W., *J. Am. Chem. Soc.* **2006,** *128*, 9024-9025.

140. Horcajada, P.; Serre, C.; Maurin, G.; Ramsahye, N. A.; Balas, F.; Vallet-Regí, M. a.; Sebban, M.; Taulelle, F.; Férey, G. r., *J. Am. Chem. Soc.* **2008,** *130*, 6774-6780.

141. Horcajada, P.; Serre, C.; Vallet-Regí, M.; Sebban, M.; Taulelle, F.; Férey, G., *Angew. Chem. Int. Ed.* **2006,** *45*, 5974-5978.

142. Horcajada, P.; Chalati, T.; Serre, C.; Gillet, B.; Sebrie, C.; Baati, T.; Eubank, J. F.; Heurtaux, D.; Clayette, P.; Kreuz, C.; Chang, J.-S.; Hwang, Y. K.; Marsaud, V.; Bories, P.-N.; Cynober, L.; Gil, S.; Ferey, G.; Couvreur, P.; Gref, R., *Nat Mater* **2010,** *9*, 172-178.

143. Taylor, K. M. L.; Jin, A.; Lin, W., *Angew. Chem. Int. Ed.* **2008,** *47*, 7722-7725.

144. Taylor, K. M. L.; Rieter, W. J.; Lin, W., *J. Am. Chem. Soc.* **2008,** *130*, 14358-14359.

145. Della Rocca, J.; Liu, D.; Lin, W., *Acc. Chem. Res.* **2011,** *44*, 957-968.

146. Cravillon, J.; Münzer, S.; Lohmeier, S.-J.; Feldhoff, A.; Huber, K.; Wiebcke, M., *Chem. Mater.* **2009,** *21*, 1410-1412.

147. Zhuang, J.-L.; Ceglarek, D.; Pethuraj, S.; Terfort, A., *Adv. Funct. Mater* **2011,** *21*, 1442-1447.

148. Flugel, E. A.; Ranft, A.; Haase, F.; Lotsch, B. V., *J. Mater. Chem.* **2012,** *22*, 10119-10133.

149. Surble, S.; Millange, F.; Serre, C.; Ferey, G.; Walton, R. I., *Chem. Commun.* **2006**, 1518-1520.

150. Zacher, D.; Liu, J.; Huber, K.; Fischer, R. A., *Chem. Commun.* **2009**, 1031-1033.

151. Millange, F.; Medina, M. I.; Guillou, N.; Férey, G.; Golden, K. M.; Walton, R. I., *Angew. Chem. Int. Ed.* **2010,** *49*, 763-766.

152. Zhao, Y.; Zhang, J.; Han, B.; Song, J.; Li, J.; Wang, Q., *Angew. Chem. Int. Ed.* **2011,** *50*, 636-639.

153. Sun, L.-B.; Li, J.-R.; Park, J.; Zhou, H.-C., *J. Am. Chem. Soc.* **2011,** *134*, 126-129.

154. Wee, L. H.; Wiktor, C.; Turner, S.; Vanderlinden, W.; Janssens, N.; Bajpe, S. R.; Houthoofd, K.; Van Tendeloo, G.; De Feyter, S.; Kirschhock, C. E. A.; Martens, J. A., *J. Am. Chem. Soc.* **2012,** *134*, 10911-10919.

155. Do, X.-D.; Hoang, V.-T.; Kaliaguine, S., *Micropor. Mesopor. Mater.* **2011,** *141*, 135-139.

156. Huang, X.-X.; Qiu, L.-G.; Zhang, W.; Yuan, Y.-P.; Jiang, X.; Xie, A.-J.; Shen, Y.-H.; Zhu, J.-F., *Cryst. Eng. Comm.* **2012,** *14*, 1613-1617.

157. Kecht, J. Colloidal Porous Nanoparticles-Synthesis and Functionalization of Nanostructured Aluminosilicates and Silicas. Ludwig-Maximilians-Universität, München, **2008**.

158. Thomas, J. M.; Gai, P. L., Electron Microscopy and the Materials Chemistry of Solid Catalysts. In *Adv. Catal.*, Academic Press: **2004**; Vol. Volume 48, pp 171-227.

159. Goodhew, P. J.; Humphreys, J.; Beanland, R., *Electron microscopy and analysis.* Taylor & Francis London, **1988**.

160. Williams, D. B.; Carter, C. B., *Transmission electron microscopy : a textbook for materials science : I : basics.* Plenum: New York, **1996**.

161. Kim, M.; Cohen, S. M., *Cryst. Eng. Comm.* **2012,** *14*, 4096-4104.

162. Schmidt-Rohr, K.; Spiess, H. W., *Multidimensional Solid State NMR and Polymers.* Academic Press, London: **1994**.

163. Laws, D. D.; Bitter, H.-M. L.; Jerschow, A., *Angew. Chem. Int. Ed.* **2002,** *41*, 3096-3129.

164. Hesse, M.; Meier, H.; Zeeh, B., *Spektroskopische Methoden in der organischen Chemie*. Thieme Stuttgart, **2005**; Vol. 7.

165. http://en.wikipedia.org/wiki/Atomic_force_microscope.

166. Junggeburth, S. C.; Schwinghammer, K.; Virdi, K. S.; Scheu, C.; Lotsch, B. V., *Chem. Eur. J.* **2012,** *18*, 2143-2152.

167. Jiang, H.-L.; Tatsu, Y.; Lu, Z.-H.; Xu, Q., *J. Am. Chem. Soc.* **2010,** *132*, 5586-5587.

168. Park, Y. K.; Choi, S. B.; Nam, H. J.; Jung, D.-Y.; Ahn, H. C.; Choi, K.; Furukawa, H.; Kim, J., *Chem. Commum.* **2010**, 3086-3088.

169. Klein, N.; Senkovska, I.; Gedrich, K.; Stoeck, U.; Henschel, A.; Mueller, U.; Kaskel, S., *Angew. Chem. Int. Ed.* **2009,** *48*, 9954-9957.

170. Mu, B.; Schoenecker, P. M.; Walton, K. S., *J. Phys. Chem. C* **2010,** *114*, 6464-6471.

171. Hartmann, M., *Angew. Chem. Int. Ed.* **2004,** *43*, 5880-5882.

172. Xiao, F.-S.; Wang, L.; Yin, C.; Lin, K.; Di, Y.; Li, J.; Xu, R.; Su, D. S.; Schlögl, R.; Yokoi, T.; Tatsumi, T., *Angew. Chem. Int. Ed.* **2006,** *45*, 3090-3093.

173. Van den Bossche, G.; Sobry, R.; Fontaine, F.; Clacens, J.-M.; Gabelica, Z., *J. Appl. Cryst.* **1997,** *30*, 1065-1074.

174. Roy, X.; MacLachlan, M. J., *Chem. Eur. J.* **2009,** *15*, 6552-6559.

175. Chiou, J. Y. Z.; Chen, J. N.; Lei, J. S.; Lin, I. J. B., *J. Mater. Chem.* **2006,** *16*, 2972-2977.

176. Schwarz, G.; Bodenthin, Y.; Tomkowicz, Z.; Haase, W.; Geue, T.; Kohlbrecher, J.; Pietsch, U.; Kurth, D. G., *J. Am. Chem. Soc.* **2010,** *133*, 547-558.

177. Choi, M.; Na, K.; Kim, J.; Sakamoto, Y.; Terasaki, O.; Ryoo, R., *Nature* **2009,** *461*, 246-249.

178. Na, K.; Choi, M.; Park, W.; Sakamoto, Y.; Terasaki, O.; Ryoo, R., *J. Am. Chem. Soc.* **2010,** *132*, 4169-4177.

179. Corma, A.; Díaz, U.; García, T.; Sastre, G. n.; Velty, A., *J. Am. Chem. Soc.* **2010,** *132*, 15011-15021.

180. Sturm, M.; Brandl, F.; Engel, D.; Hoppe, W., *Acta Cryst.* **1975,** *B31*, 2369-2378.

181. Kim, M.; Garibay, S. J.; Cohen, S. M., *Inorg. Chem.* **2011,** *50*, 729-731.

182. Campanelli, A. R.; Scaramuzza, L., *Acta Cryst.* **1986,** *C42*, 1380-1383.

183. Huo, Q.; Margolese, D. I.; Ciesla, U.; Demuth, D. G.; Feng, P.; Gier, T. E.; Sieger, P.; Firouzi, A.; Chmelka, B. F.; Schüth, F.; Stucky, G. D., *Chem. Mater.* **1994,** *6*, 1176-1191.

184. Wang, Y.; Sun, X.; Li, H., *Mater. Sci. Engin. B* **2010,** *167*, 177-181.

185. Z. Khimyak, Y.; Klinowski, J., *J. Chem. Soc., Faraday Trans.* **1998,** *94*, 2241-2247.

186. Chen, L.; Klar, P. J.; Heimbrodt, W.; Oberender, N.; Kempe, D.; Fröba, M., *Appl. Phys. Let.* **2000,** *77*, 3965-3967

187. Martin, J. D.; Keary, C. L.; Thornton, T. A.; Novotnak, M. P.; Knutson, J. W.; Folmer, J. C. W., *Nat. Mater.* **2006,** *5*, 271-275.

188. Sun, Y.; Afanasiev, P.; Vrinat, M.; Coudurier, G., *J. Mater. Chem.* **2000**, 2320-2324.

189. Tan, Y.; Steinmiller, E. M. P.; Choi, K.-S., *Langmuir* **2005,** *21*, 9618-9624.

190. Lund, K.; Muroyama, N.; Terasaki, O., *Micropor. Mesopor. Mater.* **2010,** *128*, 71-77.

191. Baran, E. J.; Ferrer, E. G.; Apella, M. C., *Monatshefte für Chemie / Chemical Monthly* **1991,** *122*, 21-26.

192. Bouchmella, K.; Dutremez, S. G.; Alonso, B.; Mauri, F.; Gervais, C., *Cryst. Growth Des.* **2008,** *8*, 3941-3950.

193. Kuroki, S.; Ando, S.; Ando, I.; Shoji, A.; Ozaki, T.; Webb, G. A., *J. Molecular Structure* **1990,** *240*, 19-29.

194. Webb, J. A.; Klijn, J. E.; Hill, P. A.; Bennett, J. L.; Goroff, N. S., *J. Org.Chem.* **2004,** *69*, 660-664.

195. Khimyak, Y. Z.; Klinowski, J., *Phys. Chem. Chem. Phys.* **2001,** *3*, 616-626.

196. Wang, L. Q.; Exarhos, G. J.; Liu, J., *Adv. Mater.* **1999,** *11*, 1331-1341.

197. Wang, L.-Q.; Liu, J.; Exarhos, G. J.; Bunker, B. C., *Langmuir* **1996,** *12*, 2663-2669.

198. Lee, C. K.; Ling, M. J.; Lin, I. J. B., *Dalton Trans.* **2003**, 4731-4737.

199. Martins, G. A. V.; Byrne, P. J.; Allan, P.; Teat, S. J.; Slawin, A. M. Z.; Li, Y.; Morris, R. E., *Dalton Trans.* **2010,** *39*, 1758-1762.

200. *Materials Studio*, 5.5.

201. Mantina, M.; Chamberlin, A. C.; Valero, R.; Cramer, C. J.; Truhlar, D. G., *J. Phys. Chem. A* **2009,** *113*, 5806-5812.

202. Jochum, M.; Unruh, H.-G.; Baernighausen, H., *J. Phys.: Condens. Matter* **1994,** *6*, 5751.

203. Liang; Shimizu, Y.; Masuda, M.; Sasaki, T.; Koshizaki, N., *Chem. Mater.* **2004,** *16*, 963-965.

204. Meyn, M.; Beneke, K.; Lagaly, G., *Inorg. Chem.* **1993,** *32*, 1209-1215.

205. Oliver, S.; Kuperman, A.; Lough, A.; Ozin, G. A., *Chem. Comm.* **1996**, 1761-1762.

206. Benjelloun, M.; Van Der Voort, P.; Cool, P.; Collart, O.; Vansant, E. F., *Phys. Chem. Chem. Phys.* **2001,** *3*, 127-131.

207. Venna, S. R.; Jasinski, J. B.; Carreon, M. A., *J. Am. Chem. Soc.* **2010,** *132*, 18030-18033.

208. Kumar, D.; Varma, S.; Dey, G. K.; Gupta, N. M., *Micropor. Mesopor. Mater.* **2004,** *73*, 181-189.

209. Alivisatos, A. P., *Science* **1996,** *271*, 933-937.

210. Thakur, P. Y.; Ram, M. Y.; Dinesh, P. S., *Nanoscience and Nanotechnology* **2012,** *2*, 22-48.

211. Adachi, M.; Nakagawa, K.; Sago, K.; Murata, Y.; Nishikawa, Y., *Chem. Commun.* **2005**, 2381-2383.

212. Nakagawa, K.; Yamaguchi, K.; Yamada, K.; Sotowa, K.-I.; Sugiyama, S.; Adachi, M., *Eur. J. Inorg. Chem.* **2012,** *2012*, 2741-2748.

213. Xu, C.; Zeng, Y.; Rui, X.; Xiao, N.; Zhu, J.; Zhang, W.; Chen, J.; Liu, W.; Tan, H.; Hng, H. H.; Yan, Q., *ACS Nano* **2012,** *6*, 4713-4721.

214. Pham, M.-H.; Vuong, G.-T.; Fontaine, F.-G.; Do, T.-O., *Cryst. Growth Des.* **2012,** *12*, 3091-3095.

215. Kijima, T.; Nagatomo, Y.; Takemoto, H.; Uota, M.; Fujikawa, D.; Sekiya, Y.; Kishishita, T.; Shimoda, M.; Yoshimura, T.; Kawasaki, H.; Sakai, G., *Adv. Funct. Mater* **2009,** *19*, 545-553.

216. Jang, J.-t.; Jeong, S.; Seo, J.-w.; Kim, M.-C.; Sim, E.; Oh, Y.; Nam, S.; Park, B.; Cheon, J., *J. Am. Chem. Soc.* **2011,** *133*, 7636-7639.

217. Vaughn II, D. D.; Patel, R. J.; Hickner, M. A.; Schaak, R. E., *J. Am. Chem. Soc.* **2010,** *132*, 15170-15172.

218. Waller, M. R.; Townsend, T. K.; Zhao, J.; Sabio, E. M.; Chamousis, R. L.; Browning, N. D.; Osterloh, F. E., *Chem. Mater.* **2012,** *24*, 698-704.

219. Gao, M.-R.; Yao, W.-T.; Yao, H.-B.; Yu, S.-H., *J. Am. Chem. Soc.* **2009,** *131*, 7486-7487.

220. Ma, R.; Sasaki, T., *Adv. Mater.* **2010,** *22*, 5082-5104.

221. Centi, G.; Perathoner, S., *Micropor. Mesopor. Mater.* **2008,** *107*, 3-15.

222. Manos, M. J.; Petkov, V. G.; Kanatzidis, M. G., *Adv. Funct. Mater* **2009,** *19*, 1087-1092.

223. Lee, K. K.; Loh, P. Y.; Sow, C. H.; Chin, W. S., *Biosensors and Bioelectronics* **2013,** *39*, 255-260.

224. Gérardin, C.; Kostadinova, D.; Sanson, N.; Coq, B.; Tichit, D., *Chem. Mater.* **2005,** *17*, 6473-6478.

225. Geng, F.; Xin, H.; Matsushita, Y.; Ma, R.; Tanaka, M.; Izumi, F.; Iyi, N.; Sasaki, T., *Chem. Eur. J.* **2008,** *14*, 9255-9260.

226. Yuan, C.; Li, J.; Hou, L.; Zhang, X.; Shen, L.; Lou, X. W., *Adv. Funct. Mater* **2012,** *22*, 4592-4597.

227. Patil, A. J.; Mann, S., *J. Mater. Chem.* **2008,** *18*, 4605-4615.

228. Miyamoto, N.; Kuroda, K.; Ogawa, M., *J. Mater. Chem.* **2004,** *14*, 165-170.

229. Ida, S.; Ogata, C.; Eguchi, M.; Youngblood, W. J.; Mallouk, T. E.; Matsumoto, Y., *J. Am. Chem. Soc.* **2008,** *130*, 7052-7059.

230. Ramakrishna Matte, H. S. S.; Gomathi, A.; Manna, A. K.; Late, D. J.; Datta, R.; Pati, S. K.; Rao, C. N. R., *Angew. Chem. Int. Ed.* **2010,** *49*, 4059-4062.

231. Omomo, Y.; Sasaki, T.; Wang; Watanabe, M., *J. Am. Chem. Soc.* **2003,** *125*, 3568-3575.

232. Ma, R.; Takada, K.; Fukuda, K.; Iyi, N.; Bando, Y.; Sasaki, T., *Angew. Chem. Int. Ed.* **2008,** *47*, 86-89.

233. Keller, S. W.; Kim, H.-N.; Mallouk, T. E., *J. Am. Chem. Soc.* **1994,** *116*, 8817-8818.

234. Li, P.-Z.; Maeda, Y.; Xu, Q., *Chem. Commun.* **2011**, 8436-8438.

235. Amo-Ochoa, P.; Welte, L.; Gonzalez-Prieto, R.; Sanz Miguel, P. J.; Gomez-Garcia, C. J.; Mateo-Marti, E.; Delgado, S.; Gomez-Herrero, J.; Zamora, F., *Chem. Commun.* **2010**, 3262-3264.

236. Li, Z.-Q.; Qiu, L.-G.; Wang, W.; Xu, T.; Wu, Y.; Jiang, X., *Inorg. Chem. Commun.* **2008,** *11*, 1375-1377.

237. Yuan, Y.; Wang, W.; Qiu, L.; Peng, F.; Jiang, X.; Xie, A.; Shen, Y.; Tian, X.; Zhang, L., *Mater. Chem. Phys.* **2011,** *131*, 358-361.

238. Tan, J. C.; Cheetham, A. K., *Chem. Soc. Rev.* **2011,** *40*, 1059-1080.

239. Saines, P. J.; Jain, P.; Cheetham, A. K., *Chem. Sci.* **2011,** *2*, 1929-1939.

240. Li, W.; Barton, P. T.; Burwood, R. P.; Cheetham, A. K., *Dalton Trans.* **2011,** *40*, 7147-7152.

241. Tan, J.-C.; Jain, P.; Cheetham, A. K., *Dalton Trans.* **2012,** *41*, 3949-3952.

242. Saines, P. J.; Barton, P. T.; Jain, P.; Cheetham, A. K., *Cryst. Eng. Comm.* **2012,** *14*, 2711-2720.

243. Saines, P. J.; Tan, J.-C.; Yeung, H. H. M.; Barton, P. T.; Cheetham, A. K., *Dalton Trans.* **2012,** *41*, 8585-8593.

244. Tan, J.-C.; Saines, P. J.; Bithell, E. G.; Cheetham, A. K., *ACS Nano* **2011,** *6*, 615-621.

245. Grant, D. M.; Pugmire, R. J., *J. Am. Chem. Soc.* **1971,** *93*, 1880-1887.

246. Li, X.-M., *Acta Crystallographica Section E* **2007,** *63*, m1984.

247. Arai, L.; Nadeem, M. A.; Bhadbhade, M.; Stride, J. A., *Dalton Trans.* **2010,** *39*, 3372-3374.

248. Chen, S.-S.; Chen, Z.-H.; Fan, J.; Okamura, T.-a.; Bai, Z.-S.; Lv, M.-F.; Sun, W.-Y., *Cryst. Growth Des.* **2012,** *12*, 2315-2326.

249. Günther, W.; Fretzdorff, A.-M., *Chem. Ber.* **1956,***Bd. 305*, 1-19.

250. Schürmann, U.; Duppel, V.; Buller, S.; Bensch, W.; Kienle, L., *Cryst. Res. Technol.* **2011,** *46*, 561-568.

251. Viculis, L. M.; Mack, J. J.; Kaner, R. B., *Science* **2003,** *299*, 1361.

252. Braga, S. F.; Coluci, V. R.; Legoas, S. B.; Giro, R.; Galvão, D. S.; Baughman, R. H., *Nano Lett.* **2004,** *4*, 881-884.

253. Taylor, R. A.; Ellis, H. A., *Spectrochimica Acta Part A: Molecular and Biomolecular Spectroscopy* **2007,** *68*, 99-107.

254. Maheshwari, S.; Jordan, E.; Kumar, S.; Bates, F. S.; Penn, R. L.; Shantz, D. F.; Tsapatsis, M., *J. Am. Chem. Soc.* **2008,** *130*, 1507-1516.

255. Baggio, R.; Garland, M. T.; Perec, M.; Vega, D., *Inorg. Chim. Acta* **1999,** *284*, 49-54.

256. Carballo, R.; Castiñeiras, A.; Covelo, B.; García-Martínez, E.; Niclós, J.; Vázquez-López, E. M., *Polyhedron* **2004,** *23*, 1505-1518.

257. Kihel, A. E.; Benchidmi, M.; Essassi, E. M.; Bauchat, P.; Danion-bougot, R., *Synth. Commun.* **1999,** *29*, 2435-2445.

258. Blackburn, B. J.; Ankrom, D. W.; Hutton, H. M., *Can. J. Chem.* **1982,** *60*, 2987-3092.

259. Levy, G. C.; Lichter, R. L., *Nitrogen-15 NMR Spectroscopy*. Wiley: New York, **1979**.

260. Martin, G. J.; Martin, M. L.; Gouesnard, J. P., *$^{15}$N-NMR Spectrocopy*. Springer Verlag: Berlin, **1981**.

261. Armstrong; Helen M. (Westfield, N., Beresis; Richard (New York, NY), Goulet; Joung L. (Westfield, NJ), Holmes; Mark A. (Middlesex, NJ), Hong; Xingfang (Westfield, NJ), Mills; Sander G. (Scotch Plains, NJ), Parsons; William H. (Belle Mead, NJ), Sinclair; Peter J. (Scotch Plains, NJ), Steiner; Mark G. (East Brunswick, NJ), Wong; Frederick (Glen Ridge, NJ), Zaller; Dennis M. (Scotch Plains, NJ) Src kinase inhibitor compounds. **2002**.

262. Autumn, K.; Liang, Y. A.; Hsieh, S. T.; Zesch, W.; Chan, W. P.; Kenny, T. W.; Fearing, R.; Full, R. J., *Nature* **2000,** *405*, 681-685.

263. http://biomaterials.bme.northwestern.edu/gecko.asp.

264 Fleming I., Nature **1967**, *216*, 151.

# 11 Publications

## Published as Part of this Thesis

1. **Towards Mesostructured Zinc Imidazolate Frameworks,**
   S. C. Junggeburth, K. Schwinghammer, K. S. Virdi, C. Scheu, B. V. Lotsch, *Chem. Eur. J.* **2012,** *18***,** 2143-2152**,** DOI: 10.1002/chem.201101530.

2. **Ultrathin 2D Coordination Polymer Nanosheets by Surfactant-Mediated Synthesis,**
   S. C. Junggeburth, L. Diehl, S. Werner, V. Duppel, W. Sigle, B. V. Lotsch, *J. Am. Chem. Soc.* **2013,** *135***,** 6157–6164, DOI: 10.1021/ja312567v.

## Published Previously

3. **Nitridogermanate nitrides $Sr_7[GeN_4]N_2$ and $Ca_7[GeN_4]N_2$: synthesis employing sodium melts, crystal structure, and density-functional theory calculations**,
   S. C. Junggeburth, O. Oeckler, D. Johrendt, W. Schnick, *Inorg. Chem.* **2008**, *47*(24), 12018-23.

4. **$Sr_5Ge_2N_6$ - a nitrido-germanate with edge-sharing double tetrahedral**,
   S. C. Junggeburth, O. Oeckler, W. Schnick, *Z. Anorg. Allg. Chem*. **2008**, 634(8), 1309-1311.

5. **Di-μ-methoxido-μ-oxido-bis[triphenylantimony(V)] methanol disolvate**
   R. Betz, S. C. Junggeburth,; P. Mayer, P. Kluefers, *Acta Cryst E.* **2010**, *E66*(1), m28.

# Contributions to Conferences

# Oral Presentations

I. **From Porous Materials to Mesostructured Zinc Imidazolates,**
   S. C. Junggeburth, S. Hug, E. Flügel, B. V. Lotsch, Max-Planck-Society, Ringberg, 2012.

II. **Mesoporous Imidazolate Frameworks (MIFs)**,
   S. C. Junggeburth, B. V. Lotsch, CeNS workshop, Venice, 2010.

## Poster Presentations

1. **Ultrathin 2D coordination frameworks**
   S. C. Junggeburth, E. Flügel, S. Werner, V. Duppel, B. V. Lotsch,
   Advisory Board Meeting at the Max-Planck-Institute for solid-state research, Stuttgart, 2012.

2. **Synthesis and Characterization of Ultrathin 2D-Zinc-Imidazolate–Acetate Nano-sheets**
   S. C. Junggeburth, V. Duppel, B. V. Lotsch,.
   Workshop Material Chemistry, Max-Planck-Institute for solid-state research, Stuttgart, 2012.

3. **Mesoporous Imidazolate Frameworks (MIFs)**
   S. C. Junggeburth, G. Rühl, B. V. Lotsch,
   NIM summer school, 2010.

4. **MesostructuredImidazolate Frameworks (MIFs)**,
   S.C. Junggeburth, K.S. Virdi, C. Scheu, B.V. Lotsch,
   CeNS workshop, Venice, 2010.

5. **Chemistry in Diminishing Dimensions: Functional Nanostructures**,
   S.C. Junggeburth, K.S. Virdi, C. Scheu, G. A. Ozin, B.V. Lotsch,
   Seon, 2010.